UNIVERSITÀ DEGLI STUDI DI PADOVA
Facoltà di Ingegneria

Corso di Laurea Magistrale in Ingegneria delle Telecomunicazioni

Tesi di Laurea

Generation and Characterization of Polarization Scrambled Optical Signals

---

Relatore:
Prof. Marco Santagiustina

Correlatore:
Prof. Luca Palmieri

Laureando:
Alex Pegoraro

Luglio 2012

A.A. 2011/2012

Abstract

Controlling the state of polarization of a light beam of an optical fiber is of crucial importance. Non-Linear *Polarization Pulling* (NLPP) (also named *Polarization Attraction*) is an all-optical way to control the state of polarization of signals which has been proposed in recent years. Polarization attraction effect enables to align a generic input State of Polarization (SOP) towards a fixed one. NLPP can be induced by various nonlinear effects occurring in optical fibers, in particular by the Stimulated Raman Scattering (SRS).

This Thesis is propaedeutic for experiments investigating NLPP. In fact, any experiment on SRS polarization pulling needs a proper polarimeter which can analyze the signals in the wavelength range from 1550 nm to 1640 nm. It is therefore necessary to employ a suitable polarimetric technique which should also give information on the spectral composition of the signals, mainly to estimate the Amplified Spontaneous Emission (ASE) due to the SRS. This polarimeter is tested and characterized in experimental tests performed during this Thesis. Moreover, there is also the necessity to generate depolarized signals to verify the repolarization capability of the NLPP effect. To meet this need, two different polarization scramblers have been employed and systematically tested to characterize the generated polarization scrambled signals.

Contents

List of Figures

List of Tables

List of Acronyms

ASE Amplified Spontaneous Emission

DOP Degree of Polarization

FRA Fiber Raman Amplifier

NLPP Non-Linear Polarization Pulling

OSA Optical Spectrum Analyzer

PC Polarization Controller

PDG Polarization Dependent Gain

PDL Polarization Dependent Loss

PM Power Meter

PMD Polarization Mode Dispersion

SOP State of Polarization

SBS Stimulated Brillouin Scattering

SRS Stimulated Raman Scattering

WDM Wavelength Division Multiplexing

Introduction

Polarization is a property of vectorial waves that describes the orientation of their oscillations. Electromagnetic waves, that is light, exhibit polarization. This fundamental property of the light has a key role in many phenomena, like for example in the propagation in optical fibers.

Polarization is also a valuable property of the signals propagating in optical fibers, as it provides an additional degree of freedom in various applications, such as advanced modulation formats in optical fiber communication systems, polarization-assisted fiber sensor broadening applications, etc. On the other hand, polarization is difficult to control and it is sometimes associated with signal degradations due to the random and dynamic polarization evolutions along the fiber, mainly caused by Polarization Mode Dispersion (PMD). PMD is a form of modal dispersion where two orthogonal polarizations of light in a fiber, which ideally travel at the same speed, actually travel at different speeds due to the random imperfections and asymmetries, causing a random spreading of the optical pulses; unless it is compensated, which is difficult task, this effect ultimately limits the rate at which data can be transmitted over a fiber.

Polarization has a key role also in the development of optical amplifiers, which are critical devices for fiber optic communication and sensing systems. In fact, one of the important properties of the amplifiers is polarization sensitivity. Unfortunately, Fiber Raman Amplifiers (FRA), exhibit Polarization Dependent Gain (PDG). In particular, if not properly controlled, the PDG of Raman amplifiers can be extremely large. Raman amplifiers are based on Stimulated Raman Scattering (SRS) in which a pump photon is scattered into a signal photon and a phonon. PDG is particularly strong for FRAs because in SRS gain is maximum when the pump and the signal are co-polarized.

Besides being an impairment, PDG can be also exploited to control polarization. The Non-Linear *Polarization Pulling* (NLPP) (also named *Polarization Attraction*) is an all-optical way to control the state of polarization of signals which has been proposed in recent years. The cumulative SRS explained above is a way to realize the NLPP. More precisely, the polarization attraction effect enables to align a generic input State of Polarization (SOP) towards a fixed one. This type of polarization pulling, which occurs thanks to the strong polarization dependence of the Raman gain, has the great advantage to completely occur in the optical domain and to be nearly instantaneous. NLPP based on SRS can achieve an high degree of repolarization of the signals and, in certain configurations, it enables to predetermine, with high reliability, the output

SOP knowing the SOP of the pump at the input ([14]). Preliminary experimental results confirming SRS-induced pulling are thus considered the seeds for the development of an innovative all-optical polarization control, suitable also for optical WDM applications thanks to the large Raman gain bandwidth ([15]).

To the aim of verifying the polarization attraction effect in counterpropagating FRAs schemes, the Degree of Polarization (DOP) as a function of the PMD coefficient, as reported in the reference article [14], must be determined experimentally.

This experimental Thesis is propaedeutic for experiments of NLPP with SRS. In fact, the experiments on polarization pulling needs a proper polarimeter which can analyze the signals in the wavelength range where Raman gain is present, i.e. from 1550 nm to 1640 nm, when a pump at 1550nm is used. When a narrow-band filter which can filter these wavelengths is not available, it is necessary to employ a suitable polarimetric technique which should also give information on the spectral composition of the signals, mainly to estimate the Amplified Spontaneous Emission (ASE) due to the SRS. This polarimeter is tested and characterized in this Thesis. There is also the necessity to generate depolarized signals to verify the repolarization capability of the NLPP effect. To meet this need, two different polarization scramblers have been used and systematically tested to characterize the generated polarization scrambled signals.

In the first part of this Thesis (Chapters 1 and 2) a review of the fundamental concepts to be dealt is given. The second part (Chapters 3, 4 and 5) is dedicated to describe the performed experimental activities and the corresponding results. The outline of the Thesis is therefore the following.

- **Chapter 1**: in this Chapter we introduce the concept of polarization. The first part of the Chapter describes some general characteristic of the polarization, with its analytical treatment, introducing the formalism due to Stokes. Here, it is also underlined the usefulness of the so-called Poincaré sphere for the visualization of the SOPs. Moreover, the Jones and Müller matrices for optical devices are introduced, with their properties related to the representation of the polarization of light. The remaining sections of the Chapter concern SRS and FRAs in fiber optics. In particular, the gain and bandwidth of FRAs, as well as the other main characteristics and performance are discussed in detail. The final part of the Chapter deals with the polarization attraction in the counterpropagating configurations of the FRAs.

- **Chapter 2**: the methods for measuring polarization are introduced. In particular, the focus is on the classic quarter-wave plate polarimeter, which is a simple polarimetric method we use in our experimental tests. The measurement of the SOP is obtained by analytical calculations from the detected power. The second part of the Chapter deals with the concept of polarization scrambling, which permits to actively change the SOP using polarization modulation method. The principles of scrambling are introduced, explaining the reasons for which it is employed. The most common types of scramblers are described, underlining their advantages and disadvantages and their typical applications.

- **Chapter 3**: in this Chapter there is a description of the experimental activities performed to test and characterize a polarimetric system in various configurations with a polarized input signal. An interesting drift effect, which had a strong influence on polarization measurements, is described and studied too. Many of the concepts explained in the two previous Chapters about polarization and polarimetric techniques are used here. From an experimental viewpoint, power measurements, which are necessary to measure the SOP employing the polarimetric technique explained in Chapter 2, are performed using two different optical instruments. This aspect, which is mainly due to the necessity of have information on the spectral composition of the signals, makes necessary certain precautions and considerations on polarization measurements.

- **Chapter 4**: SOP and DOP of polarization scrambled signals are measured with the same polarimetric technique, previously tested. In particular, we use both an optical power meter and an optical spectrum analyzer to measure optical power. The main features of the employed scrambler are listed, in particular the scrambling modes are described. Some preliminary experimental tests of these scrambling modes are performed and the corresponding measured DOPs are reported. A set of systematic tests of the scrambling modes is also presented. From the measurements obtained in these tests, some remarks about the quality of the scrambling and about the capability of the OSA to measure the DOP of a scrambled beam are provided.

- **Chapter 5**: with the scrambling system described and tested in the previous Chapter, the measured DOP is frequently not sufficiently low, as expected. This Chapter therefore describes the experimental characterization of a second, more performant polarization scrambler based on piezoelectric squeezers. We verify its characteristics in some different tests. The methods of measuring and analysis are presented. In particular, we focus on the frequency response and on the settling-time when analog step signals are applied to the electrical inputs. Remarks about the scrambling capability of this device are hence provided from the analysis of the measured electrical parameters.

Chapter 1

Concepts about polarization and polarization effects in optical fibers

The primary aim of this initial Chapter is to introduce the concept of polarization. This property of light and, in general, of electromagnetic waves has many important applications, but is a complex issue. Therefore, the first part of the Chapter describes some general characteristic of polarization. After this, an analytical treatment of polarization is presented, introducing the formalism due to Stokes, which is a fundamental tool to represent the state of polarization (SOP) of a light beam. It is also underlined the usefulness of the so-called Poincaré sphere for the visualization of SOPs. Moreover, Jones and Müller matrices for optical devices are introduced, with their properties related to the representation of polarization of light.

The remaining sections of the Chapter concern Raman scattering and Raman amplifiers in fiber optics. The treatment of these topics is quite detailed. In particular, the gain and the bandwidth of Fiber Raman Amplifiers (FRAs), their main characteristics and performance are topics discussed in detail to introduce another argument. In fact, the final part of the Chapter deals with polarization attraction in counterpropagating configurations of FRAs. This effect is an interesting and powerful way to control the SOP of light employing optical nonlinear effects, in this case, stimulated Raman scattering. The discussion of these arguments has been included here because the experimental tests and the results with which this Thesis deals are preparatory to experiments concerning the polarization attraction effect in FRAs.

1.1 The polarization of an electromagnetic field

Polarization is a property of vectorial waves that describes the orientation of their oscillations. Electromagnetic waves, such as light, and gravitational waves exhibit polarization; acoustic waves in a gas or liquid do not have polarization because the direction of vibration and direction of propagation are the same.

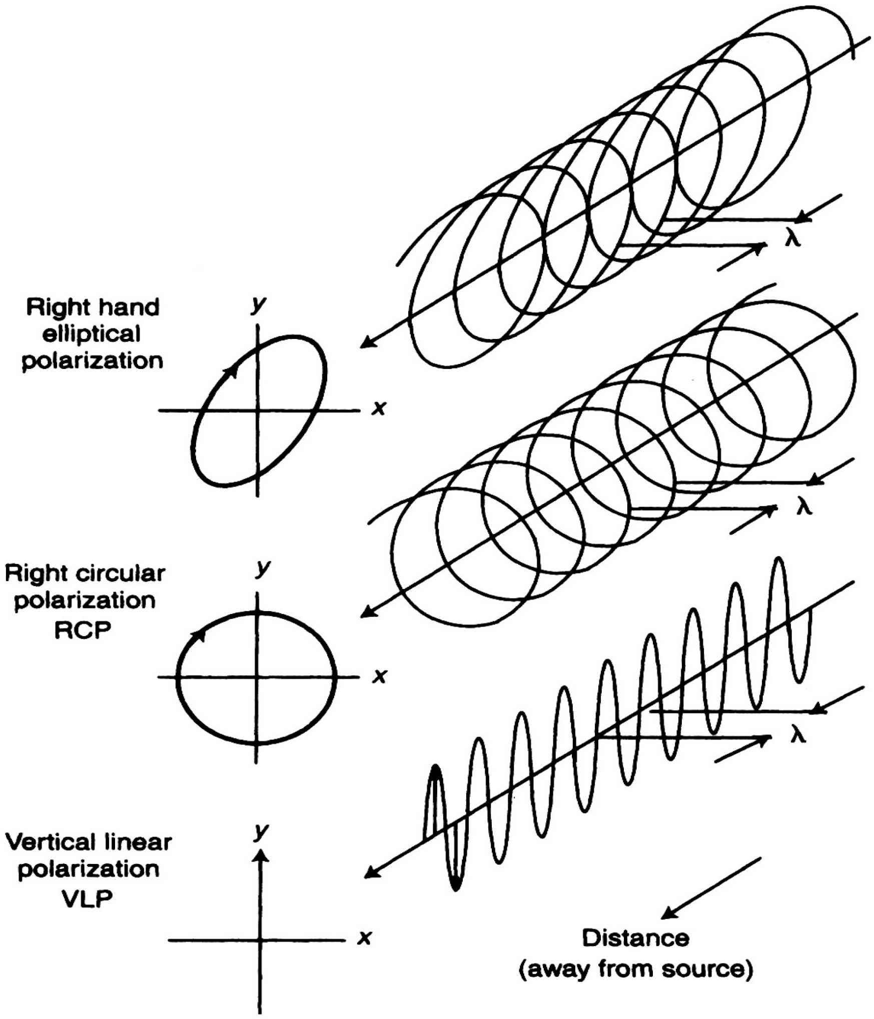

Figure 1.1: Representation of elliptical, circular and linear polarizations. (From [2].)

By convention, polarization of light is described by specifying the orientation of the wave's electric field at a point in space over one period of the oscillation. When light travels in free space, in most cases it propagates as a *transverse wave*, i.e. the plane described by the polarization is perpendicular to the wave's direction of travel. In this case, the electric field may be oriented in a single direction (*linear polarization*), or it may rotate as the wave travels (*circular* or *elliptical polarization*). In the latter cases, the oscillations can rotate on the polarization plane either towards the right or towards the left in the direction of travel. The direction of rotation generated by the propagation of the wave is called the wave's handedness or chirality. In Fig. 1.1 is present a qualitative representation of the types of polarization with the optical signal evolving in its direction of propagation.

In general, the polarization of an electromagnetic wave is a complex issue. For instance, in a waveguide such as an optical fiber, or for radially polarized beams in free space, the description of the wave's polarization is more complicated, as the fields can have longitudinal as well as transverse components. For longitudinal waves such as sound waves in fluids, the direction of oscillation is by definition along the direction of travel, so there is no polarization, as mentioned above. In a solid medium, however, sound waves can be transverse, with the polarization describing a plane perpendicular to the propagation direction. This is important in seismology.

Polarization is significant in many areas of science and technology dealing with wave propagation, such as optics, telecommunications, radar science and seismology. The polarization of light can be measured with a *polarimeter*. A *polarizer* is a device that affects polarization, for instance, making polarized an unpolarized light beam.

However, in optical fibers context, with which this Thesis deals, polarization is a paradoxical parameter. In fact, on the one hand, it provides flexibilities in various applications; some important applications are advanced modulation formats in optical fiber communication systems, polarization-assisted fiber sensor applications, sensitivity-enhanced biomedical applications, etc. On the other hand, unfortunately, polarization is difficult to control and even associated with signal degradation due to random and dynamic polarization evolutions along the fiber, caused mainly by the Polarization Mode Dispersion (PMD). Currently polarization-related impairments are among major hurdles for high performance fiber systems ([1]).

In the next Section, some fundamental analytical considerations about polarization and the most used representation for the polarization state of light are presented.

1.1.1 Representations and analytical treatment of polarization

A monochromatic sinusoidal electromagnetic field in a generic point p may be expressed as:

$$\tilde{E}(t,p) = \sum_{n=1}^{3} \hat{x}_n A_n(p) \cos\left(\omega t + \phi_n(p)\right) \ , \tag{1.1}$$

where $\hat{x}_n$ is the unit vector of the n-th reference axis, and $A_n(p)$ is the amplitude in the point p ([2]). It can be verified that the vector expressed in Eq. (1.1) belongs to the *plane* defined by two vectors $\bar{A}'$ and $\bar{A}''$, such that

$$\tilde{E}(t,p) = \bar{A}'(p)\cos(\omega t) - \bar{A}''\sin(\omega t) \ . \tag{1.2}$$

In a generic 2-dimensional reference frame $[x, y]$ we can write:

$$\bar{A}' = a'_x\hat{x} + a'_y\hat{y} \ , \qquad \bar{A}'' = a''_x\hat{x} + a''_y\hat{y} \ , \tag{1.3}$$

such that the field in this frame yields:

$$\begin{pmatrix} E_x(t) \\ E_y(t) \end{pmatrix} = \begin{pmatrix} a'_x & -a''_x \\ a'_y & -a''_y \end{pmatrix} \begin{pmatrix} \cos(\omega t) \\ \sin(\omega t) \end{pmatrix} \ . \tag{1.4}$$

From this expression it is clear that *the monochromatic field has an elliptical polarization.* An elliptical polarized field in the reference frame of its principal axes $[x', y']$ can be expressed as

$$\tilde{E}'(t) = \begin{pmatrix} E_{x'}(t) \\ E_{y'}(t) \end{pmatrix} = \begin{pmatrix} a\cos(\omega t + \gamma) \\ b\sin(\omega t + \gamma) \end{pmatrix} , \tag{1.5}$$

where γ is a phase constant. In order to represent the field in a generic reference frame, we rotate the ellipse by an angle δ as in Fig. 1.2(a), which corresponds to this matrix multiplication:

$$\begin{aligned} \tilde{E}(t) &= \begin{pmatrix} E_x(t) \\ E_y(t) \end{pmatrix} = \begin{pmatrix} \cos(\delta) & -\sin(\delta) \\ \sin(\delta) & \cos(\delta) \end{pmatrix} \begin{pmatrix} a\cos(\omega t + \gamma) \\ b\sin(\omega t + \gamma) \end{pmatrix} \\ &= \begin{pmatrix} a\cos(\delta) \\ a\sin(\delta) \end{pmatrix} \cos(\omega t + \gamma) - \begin{pmatrix} b\sin(\delta) \\ -b\cos(\delta) \end{pmatrix} \sin(\omega t + \gamma) . \end{aligned} \tag{1.6}$$

Remembering the Steinmetz operator and representation, we can write

$$\tilde{E}(t) = \Re\left\{\bar{E}e^{j\omega t}\right\} , \tag{1.7}$$

where $\bar{E}$ is a complex vector which represents the state of polarization (SOP) in two dimensions through the *ellipse of polarization.* From the previous expressions follows that

$$\bar{E} = \begin{pmatrix} E_x \\ E_y \end{pmatrix} = \begin{pmatrix} a\cos(\delta) + jb\sin(\delta) \\ a\sin(\delta) - jb\cos(\delta) \end{pmatrix} e^{j\gamma} . \tag{1.8}$$

The SOP of a generic field $\bar{E} = (E_x, E_y)$ can be represented introducing the *Stokes' Vector*, evolving on the unit-radius sphere, called the *Poincaré sphere.* The Stokes' vector $\hat{s}$ is defined as

$$\hat{s} = \bar{S} = \begin{pmatrix} s_0 \\ s_1 \\ s_2 \\ s_3 \end{pmatrix} = \begin{pmatrix} E_xE_x^* + E_yE_y^* \\ E_xE_x^* - E_yE_y^* \\ E_xE_y^* + E_yE_x^* \\ -j(E_xE_y^* - E_yE_x^*) \end{pmatrix} = \begin{pmatrix} a^2 + b^2 \\ (a^2 - b^2)\cos(2\delta) \\ (a^2 - b^2)\sin(2\delta) \\ 2ab \end{pmatrix} \tag{1.9}$$

We unambiguously use both the notations $\hat{s}$ and $\bar{S}$ to indicate the Stokes' vector. The four component of the Stokes' vector are therefore expressed in terms of intensities and are real quantities, and can be interpreted as follows. The component s_0 is the intensity of the light, s_1 gives the similarity of the polarization to the horizontal/vertical linear polarizations, s_2 reflects the tendency for ±45° linear polarizations; finally, s_3 denotes the inclination toward right or left handedness.

The $\hat{s}$ vector of Eq. (1.9) can be normalized respect the field intensity s_0 obtaining

$$\hat{s} = \begin{pmatrix} \frac{a^2-b^2}{a^2+b^2}\cos(2\delta) \\ \frac{a^2-b^2}{a^2+b^2}\sin(2\delta) \\ \frac{2ab}{a^2+b^2} \end{pmatrix} = \begin{pmatrix} \cos(2\varepsilon)\cos(2\delta) \\ \cos(2\varepsilon)\sin(2\delta) \\ \sin(2\varepsilon) \end{pmatrix} , \tag{1.10}$$

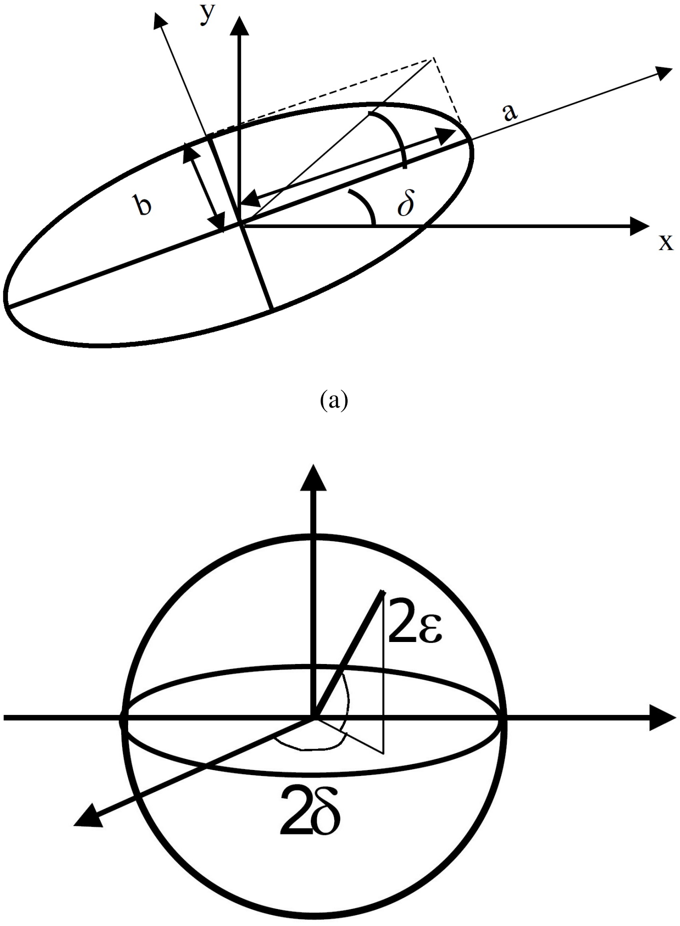

(a)

(b)

Figure 1.2: Rotated polarization ellipse, and representation of relevant angles in the unit radius sphere. (From [2].)

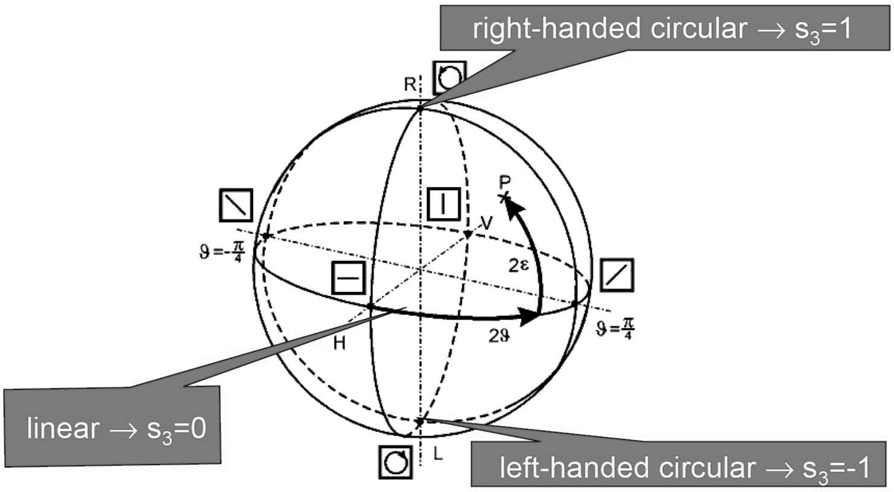

Figure 1.3: Poincaré sphere with azimuthal and ellipticity angles, and indications about the type of polarization depending on the Stokes' vector $\hat{s} = (s_1, s_2, s_3)$. (From [2].)

with δ and ε related to the azimuthal and polar angles (ellipticity), respectively, as depicted in Fig. 1.2(b). It can be simply verified from these expressions of $\hat{s}$ that $s_3 = 0$ corresponds to a linear polarization, $s_3 = 1$ to a right-handed circular polarization and $s_3 = -1$ to a left-handed circular polarization. The normalized Stokes' vectors can be represented graphically on the Poincaré sphere, as represented in Fig. 1.3. This graphic representation is very useful because it gives exhaustive information about the polarization of a light beam, if the Stokes' vector is known. Moreover, also the evolution of the polarization during a certain time-interval can be usefully visualized on the sphere.

Regarding the different representations for the polarization state of light in optical devices, the widely used ones are the Jones matrix and the Müller matrix, with the latter a generalization of the former. The Stokes' parameters are related to them, as explained below. The Jones matrix completely describes polarized light but can only be used for fully polarized light. In particular, the Jones matrix $\mathbf{J}$ of an optical device describes the analytical relation between the field complex vector at the input and the vector at the output of the device, in this way:

$$\bar{E}_{\text{out}} = \mathbf{J}\bar{E}_{\text{in}} \; . \tag{1.11}$$

Instead, the Stokes' parameters and the Müller matrix can describe unpolarized light and use parameters that are easily measurable with an optical power meter. The input and output of Stokes's vector of an optical device can be related with the Müller matrix. In fact, in correspondence to a cascade of n optical devices, with the n-th device at the output of the cascade, it can be verified that

$$\hat{s}_{\text{out}} = \mathbf{M_n M_{n-1}} \cdots \mathbf{M_2 M_1} \hat{s}_{\text{in}} \; . \tag{1.12}$$

Summarizing, any fully polarized, partially polarized, or unpolarized state of light can be rep-

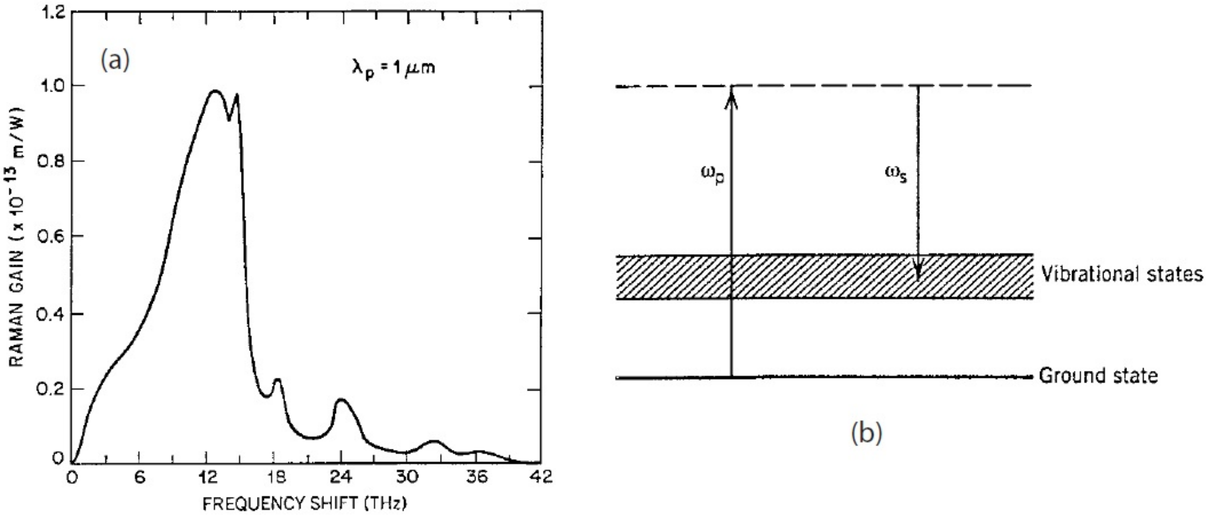

Figure 1.4: (a) Raman gain spectrum of fused silica at λ_p=1 μm and (b) energy levels participating in the SRS process. (From [4].)

resented by a Stokes' vector; any optical element can be represented by a Müller matrix. Consequently, any SOP at the output of an optical device or a cascade of devices can be univocally identified if the the input SOP and the Müller matrices of each device are known.

For further details about the Jones and Müller matrices and their analytical properties, here not essentials, there are many textbooks and articles, for example [2] and [3].

1.2 Stimulated Raman scattering

Spontaneous Raman Scattering occurs in optical fibers when a pump wave (at angular frequency ω_p) is scattered by the silica molecules, as explained in [4]. It can be understood using the energy-level diagram shown in Fig. 1.4(b). Some pump photons give up their energy to create other photons of reduced energy at a lower frequency; the remaining energy is absorbed by silica molecules, which end up in an excited vibrational state with phonons emission. An important difference from Brillouin scattering is that the vibrational energy levels of silica dictate the value of the Raman shift $\Omega_R = \omega_p - \omega_s$. As an acoustic wave is not involved, *spontaneous* Raman scattering is an isotropic process and occurs in all directions.

Similar to the Stimulated Brillouin Scattering (SBS), the Raman Scattering process becomes *Stimulated* (SRS) if the pump power exceeds a threshold value. SRS can occur in both the forward and backward directions in optical fibers. Physically speaking, the beating of the pump with the scattered light in these two directions creates a frequency component at the beat frequency $\omega_p - \omega_s$, which acts as a source that derives molecular oscillations; ω_s is called the *Stokes* *frequency*. Since the amplitude of the scattered wave increases in response to these oscillations, a positive feedback loop sets in. In the case of forward SRS, the feedback process is governed by the following set of two coupled equations [5]:

$$\frac{dI_p}{dz} = -g_R I_p I_s - \alpha_p I_p \ , \tag{1.13}$$

$$\frac{dI_s}{dz} = g_R I_p I_s - \alpha_s I_s \ , \tag{1.14}$$

where I_p and I_s are the intensity of the pump and the signal, respectively, and g_R is the SRS gain. In the case of backward SRS, a minus sign is added in front of the derivative in Eq. (1.14), and this set of equations becomes identical to the SBS case.

The spectrum of the Raman gain depends on the decay time associated with the excited vibrational state. In the case of a molecular gas or liquid, the decay time is relatively long ($\sim$1 ns), resulting in a Raman-gain bandwidth of $\sim$1 GHz. In the case of optical fibers, the bandwidth exceeds 10 THz. Fig. 1.4(a) shows the Raman-gain spectrum of silica fibers. The broadband and multipeak nature of the spectrum is due to the amorphous nature of glass. More specifically, vibrational energy levels of silica molecules merge together to form a band. As a result, the Stokes frequency ω_s can differ from the pump frequency ω_p over a wide range. The maximum gain occurs when the Raman shift $\Omega_R \equiv \omega_p - \omega_s$ is about 13 THz. Another major peak occurs near 15 THz while minor peaks persist for values of Ω_R as large as 35 THz. The peak value of the Raman gain g_R is about 1×10^{-13} m/W at a wavelength of 1 μm. This value scales linearly with ω_p (or inversely with the pump wavelength λ_p), resulting in $g_R \approx 6 \times 10^{-13}$ m/W at 1.55 μm.

Similar to the case of SBS, the threshold power $P_{\mathbf{th}}$ is defined as the incident power at which half of the pump power is transferred to the Stokes field at ω_s at the output end of a fiber length L. An estimate of $P_{\mathbf{th}}$ is in [4]

$$g_R P_{\mathbf{th}} L_{\mathbf{eff}} / A_{\mathbf{eff}} \approx 16 \ , \tag{1.15}$$

where g_R is the peak value of the Raman gain, and $L_{\mathbf{eff}}$ can be approximated by $1/\alpha$. If we replace $A_{\mathbf{eff}}$ by πw^2, where w is the spot size ([4], Section 2.3), $P_{\mathbf{th}}$ for SRS is given by

$$P_{\mathbf{th}} \approx 16\alpha(\pi w^2)/g_R \ . \tag{1.16}$$

If we use $\pi w^2 = 50$ μm^2 and $\alpha = 0.2$ dB/km (common fibers) as the representative values, $P_{\mathbf{th}}$ is about 570 mW near 1.55 μm. It is important to emphasize that Eq. (1.16) provides an order-of-magnitude estimate only as many approximations are made in its derivation. As channel powers in optical communication systems are typically below 10 mW, SRS is not a limiting factor for single-channel lightwave systems. However, it affects the performance of Wavelength Division Multiplexing (WDM) systems considerably; Chapter 8 of [4] deals with this aspect.

Both SRS and SBS can be used to advantage while designing optical communication systems because they can amplify an optical signal by transferring energy to it from a pump beam whose

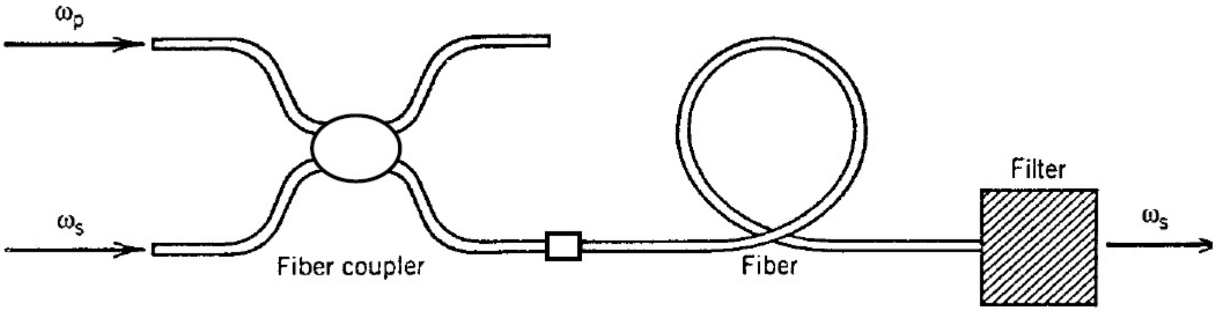

Figure 1.5: Schematic of a fiber-based Raman amplifier in the forward-pumping configuration. (From [4].)

wavelength is suitably chosen; the amplification is all-optical. SRS is especially useful because of its extremely large bandwidth. Indeed, the Raman gain is used routinely for compensating fiber losses in modern lightwave systems, as discussed in Section 1.3.

1.3 Raman amplifiers

A fiber-based Raman amplifier uses *Stimulated Raman Scattering* (SRS) occurring in silica fibers when an intense pump beam propagates through it [4], [5]. The main features of SRS have been discussed in Section 1.2. SRS differs from stimulated emission in one fundamental aspect. Whereas in the case of stimulated emission an incident photon stimulates emission of another identical photon without losing its energy, in the case of SRS the incident pump photon gives up its energy to create another photon of reduced energy at a lower frequency ω_s (inelastic scattering); the remaining energy is absorbed by the medium in the form of molecular vibrations (optical phonons). Thus, Raman amplifiers must be pumped optically to provide gain. Fig. 1.5 shows how a fiber can be used as a Raman amplifier. The pump and signal beams at frequency ω_p and ω_s are injected into the fiber through a fiber coupler. The energy is transferred from the pump beam to the signal beam through SRS as the two beams copropagate inside the fiber. The pump and signal beams counterpropagate in the backward-pumping configuration commonly used in practice; this type of configuration is preferred because of its better noise characteristics [6].

1.3.1 Raman gain and bandwidth

The Raman-gain spectrum of silica fibers is shown in Fig. 1.4; its broadband nature is a consequence of the amorphous nature of glass. The Raman-gain coefficient g_R is related to the optical gain $g(z)$ as $g = g_R I_p(z)$, where I_p is the pump intensity. In terms of the pump power P_p, the gain can be written as

$$g(\omega) = g_R(\omega)(P_p/a_p) , \tag{1.17}$$

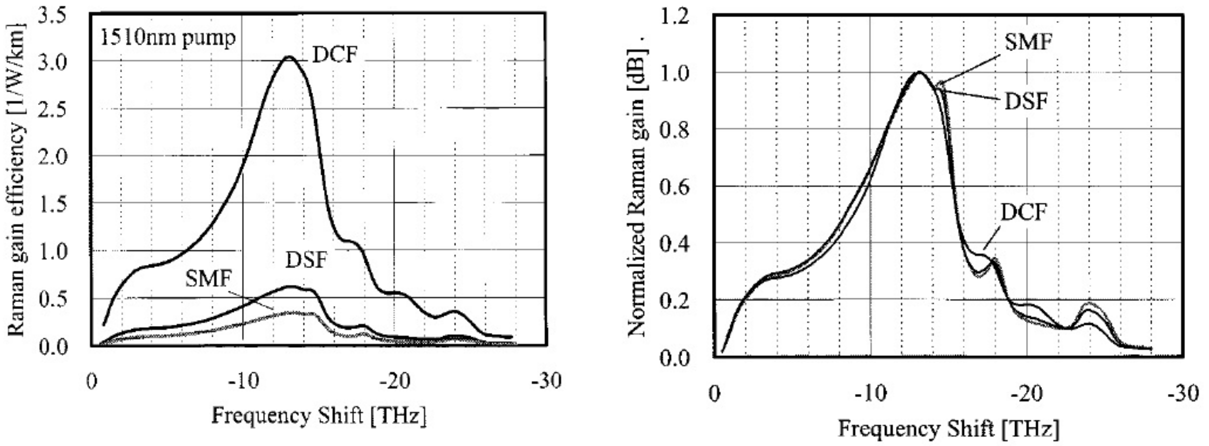

Figure 1.6: Raman-gain spectra (ratio g_R/a_p) for standard (SMF), dispersion-shifted (DSF) and dispersion-compensating (DCF) fibers. (From [4].)

where a_p is the cross-sectional area of the pump beam inside the fiber. Since a_p can vary considerably for different types of fibers, the ratio g_R/a_p is a measure of the Raman-gain efficiency. This ratio is plotted in Fig. 1.6 for three different fibers. A dispersion-compensating fiber (DCF) can be 8 times more efficient than a standard silica fiber (SMF) because of its smaller core diameter. The frequency dependence of the Raman gain is almost the same for the three kinds of fibers as evident from the normalized gain spectra shown in Fig. 1.6. The gain peaks at a Stokes shift of about 13.2 THz. The gain bandwidth $\Delta\nu_g$ is about 6 THz if we define it as the FWHM (half-magnitude) of the dominant peak in Fig. 1.6.

The large bandwidth of fiber Raman amplifiers makes them attractive for fiber-optic communication applications. However, a relatively large pump power is required to realize a large amplification factor. For example, if we use

$$G(\omega) = \exp[g(\omega)L] \tag{1.18}$$

for the amplification factor G, by assuming operation in the unsaturated region, $gL \approx 6.7$ is required for G =30 dB. By using $g_R = 6 \times 10^{-14}$ m/W at the gain peak at 1.55 μm and a_p =50 μm^2, the required pump power is more than 5 W for 1-km-long fiber. The required power can be reduced for longer fibers, but then fiber losses must be included. In Section 1.3.2 there is the discussion of the theory of Raman amplifiers including both fiber losses and pump depletion.

1.3.2 Amplifier characteristics

It is necessary to include the effects of fiber losses because of a long fiber length required for Raman amplifiers. Variations in the pump and signal powers along the amplifier length can be studied by solving the two coupled equations (1.13) and (1.14). In the case of forward pumping, these equations take the form

$$dP_s/dz = -\alpha_s P_s + (g_R/a_p)P_p P_s \ , \tag{1.19}$$

$$dP_p/dz = -\alpha_p P_p - (\omega_p/\omega_s)(g_R/a_p)P_s P_p \ , \tag{1.20}$$

where α_s and α_p represent fiber losses at the signal and pump frequencies ω_s and ω_p, respectively. The factor ω_p/ω_s results from different energies of pump and signal photons and disappears if these equations are written in terms of photon numbers.

Consider first the case of small-signal amplification for which pump depletion can be neglected (the last term in Eq. (1.20)). Substituting $P_p(z) = P_p(0)\exp(-\alpha_p z)$ in Eq. (1.19), the signal power at the output of an amplifier of length L is given by

$$P_s(L) = P_s(0)\exp(g_R P_0 L_{\text{eff}}/a_p - \alpha_s L) \ , \tag{1.21}$$

where $P_0 = P_p(0)$ is the input power and L_{eff} is defined as

$$L_{\text{eff}} = [1 - \exp(-\alpha_p L)]/\alpha_p \ . \tag{1.22}$$

Because of fiber losses at the pump wavelength, the effective length of the amplifier is less than the actual length L; $L_{\text{eff}} \approx 1/\alpha_p$ for $\alpha_p L \gg 1$. Since $P_s(L) = P_s(0)\exp(-\alpha_s L)$ in the absence of Raman amplification ($g_R = 0$), the amplifier gain is given by

$$G_A = \frac{P_s(L)}{P_s(0)\exp(-\alpha_s L)} = \exp(g_0 L) \ , \tag{1.23}$$

where the small-signal gain is defined as

$$g_0 = g_R\left(\frac{P_0}{a_p}\right)\left(\frac{L_{\text{eff}}}{L}\right) \approx \frac{g_R P_0}{a_p \alpha_p L} \ . \tag{1.24}$$

The last relation holds for $\alpha_p L \gg 1$. The amplification factor G_A becomes length independent for large values of $\alpha_p L$. Fig. 1.7 shows variations of G_A with P_0 for several values of input signal powers for a 1.3-km-long Ramana amplifier operating at 1.064 μm and pumped at 1.017 μm. The amplification factor increases exponentially with P_0 initially but then starts to deviate for P_0 >1 W because of gain saturation. Deviations become larger with an increase in $P_s(0)$ as gain saturation sets in earlier along the amplifier length. The solid lines in Fig. 1.7 are obtained by solving Eqs. (1.19) and (1.20) numerically to include pump depletion.

The origin of gain saturation can be explained by the fact that the pump begins to deplete as the signal power P_s increases, since it supplies energy for signal amplification. A decrease in the pump power P_p reduces the optical gain as seen from Eq. (1.17). This reduction in gain is referred to as *gain saturation*. An approximate expression for the saturated amplifier gain

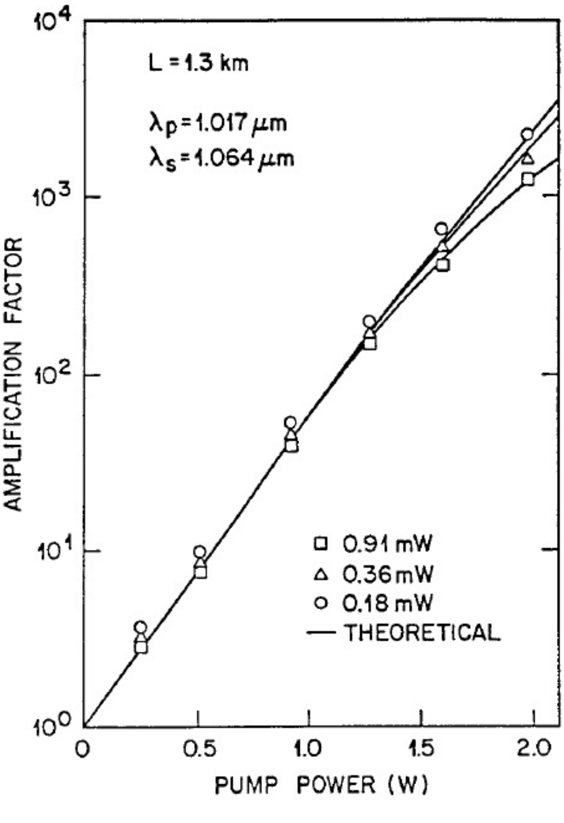

Figure 1.7: Variation of amplifier gain G_0 with pump power P_0 in a 1.3-km-long Raman amplifier for three values of the input power. Solid lines show the theoretical prediction. (From [7].)

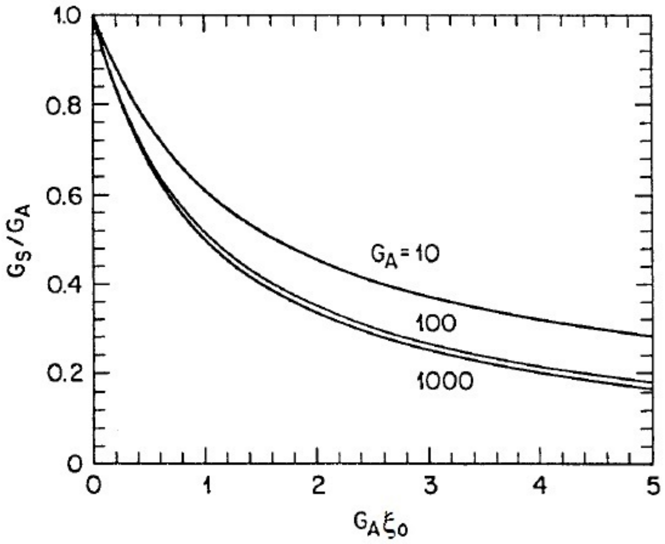

Figure 1.8: Gain-saturation characteristics of Raman amplifiers for several values of the unsaturated amplifier gain G_A. (From [7].)

$G_s = G_A^{(sat)}$ can be obtained assuming $\alpha_s = \alpha_p$ in Eqs. (1.19) and (1.20). The result is given by [5]

$$G_s = \frac{1+\xi_0}{\xi_0 + G_A^{-(1+\xi_0)}}\,, \qquad \xi_0 = \frac{\omega_p}{\omega_s}\frac{P_s(0)}{P_p(0)}\,. \tag{1.25}$$

Fig. 1.8 shows the saturation characteristic by plotting G_s/G_A as a function of $G_A\xi_0$ for several values of G_A. The amplifier gain is reduced by 3 dB when $G_A\xi_0 \approx 1$. This condition is satisfied when the power of the amplified signal becomes comparable to the input pump power P_0. In fact, P_0 is a good measure of the saturation power. Since typically $P_0 \sim 1$ W, the saturation power of fiber Raman amplifiers is much larger than that of other otical amplifiers, for example Semiconductor Optical Amplifiers (SOAs). As typical channel powers in a WDM system are $\sim$1 mW, Raman amplifiers operate in the unsaturated or linear regime, and Eq. (1.24) can be used in place of Eq. (1.25).

Noise in Raman amplifiers stems from spontaneous Raman scattering. It can be included in Eq. (1.19) by replacing P_s in the last term with $P_s + P_{\mathrm{sp}}$, where $P_{\mathrm{sp}} = 2n_{\mathrm{sp}}h\nu_s\Delta\nu_R$ is the total spontaneous Raman power over the entire Raman-gain bandwidth $\Delta\nu_R$. The factor of 2 accounts for the two polarization directions. The factor $n_{\mathrm{sp}}(\Omega)$ equals $[1-\exp(-\hbar\Omega_s/k_BT)]^{-1}$, where k_BT is the thermal energy at room temperature (about 25 meV). In general, the added noise is much smaller for Raman amplifiers because of the distributed nature of the amplification.

1.3.3 Amplifier performance

As seen in Fig. 1.7, Raman amplifiers can provide 20-dB gain at a pump power of about 1 W. For the optimum performance, the frequency difference between the pump and signal beams should correspond to the peak of the Raman gain in Fig. 1.6 (occurring at about 13 THz, optimum Raman shift). In the near-infrared region, the most practical pump source is a diode-pumped Nd:YAG laser operating at 1.06 μm. For such a pump laser, the maximum gain occurs for signal wavelengths near 1.12 μm, i.e. a shift of about 60 nm. However, the wavelengths of most interest for fiber-optic communication systems are near 1.3 and 1.5 μm. A Nd:YAG laser can still be used if a higher-order Stokes line, generated through cascaded SRS, is used as a pump. For instance, the third order Stokes line at 1.24 μm can act as a pump for amplifying the 1.3-μm signal. Amplifier gains of up to 20 dB were measured in 1984 with this technique. An early application of Raman amplifiers was as a preamplifier for improving the receiver sensitivity [8].

The broad bandwidth of Raman amplifiers is useful for amplifying several channels simultaneously. As early as 1988, signal from three DFB (Distributed Feedback) semiconductor lasers operating in the range 1.57-1.58 μm were amplified simultaneously using a 1.47-μm pump. This experiment used a semiconductor laser as a pump source. An amplifier gain of 5 dB was realized at a pump power of only 60 mW. In another interesting experiment [9], a Raman amplifier was pumped by a 1.55-μm semiconductor laser whose output was amplified using an erbium-doped fiber amplifier. The 140-ns pump pulses had 1.4 W peak power at the 1-kHz repetition rate and were capable of amplifying 1.66-μm signal pulses by more than 23 dB through SRS in a 20-km-long dispersion-shifted fiber. The 200 mW peak power of 1.66-μm pulses was large enough for their use for optical time-domain reflection (OTDR) measurements commonly used for supervising and maintaining fiber-optic networks.

The use of Raman amplifiers in the 1.3-μm spectral region has also attracted attention. However, a 1.24-μm pump laser is not readily available (2001). Cascaded SRS can be used to generate the 1.24-μm pump light. In one approach, three pairs of fiber gratings are inserted within the fiber used for Raman amplification. The Bragg wavelengths of these gratings are chosen such that they form three cavities for three Raman lasers operating at wavelengths 1.117, 1.175, and 1.24 μm that correspond to first-, second-, and third-order Stokes lines of the 1.06-μm pump. All three lasers are pumped by using a diode-pumped Nd-fiber laser through cascaded SRS. The 1.24-μm laser then pumps the Raman amplifier and amplifies a 1.3-μm signal. The same idea of cascaded SRS was used to obtain 39-dB gain at 1.3 μm by using WDM couplers in place of fiber gratings [10]. Such 1.3-μm Raman amplifiers exhibit high gains with a low noise figure (about 4 dB) and are also suitable as an optical preamplifier for high-speed optical receivers. In a 1996 experiment, such a receiver yielded the sensitivity of 151 photons/bit at a bit rate of 10 Gb/s [11]. The 1.3-μm Raman amplifiers can also be used to upgrade the capacity of existing fiber links from 2.5 to 10 Gb/s.

Raman amplifiers are called lumped or distributed depending on their design. In the lumped case, a discrete device is made by spooling 1-2 km of a especially prepared fiber that has been doped with germanium or phosphorus for enhancing the Raman gain. The fiber is pumped at a wavelength near 1.45 μm for amplification of 1.55-μm signals. In the case of distributed Raman amplification, the same fiber that is used for signal transmission is also used for signal amplification. The pump light is often injected in the backward direction and provides gain over relatively long lengths (>20 km). The main drawback in both cases from the system standpoint is that high-power lasers are required for pumping. Early experiments often used a tunable color-center laser as a pump; such lasers are too bulky for system applications. For this reason, Raman amplifiers were rarely used during the 1990s after erbium-doped fiber amplifiers became available. The situation changed by 2000 with the availability of compact high-power semiconductor and fiber lasers.

The phenomenon that limits the performance of distributed Raman amplifiers most turns out to be Rayleigh scattering. As discussed in [4], Rayleigh scattering occurs in all fibers and is the fundamental loss mechanism for them. A small part of light is always backscattered because of this phenomenon. Normally, this Rayleigh backascattering is negligible. However, it can be amplified over long lengths in fibers with distributed gain and affects the system performance in two ways. First, a part of backward propagating noise appears in the forward direction, enhancing the overall noise. Second, double Rayleigh scattering of the signal creates a crosstalk component in the forward direction. It is this Rayleigh crosstalk, amplified by the distributed Raman gain, that becomes the major source of power penalty. The fraction of signal power propagating in the forward direction after double Rayleigh scattering is the Rayleigh crosstalk. This fraction is given by [12]

$$f_{\mathbf{DRS}} = r_s^2 \int_0^z dz_1 G^{-2}(z_1) \int_{z_1}^L G^2(z_2) dz_2 \ , \tag{1.26}$$

where $r_s \sim 10^{-4}$ km^{-1} is the Rayleigh scattering coefficient and $G(z)$ is the Raman gain at a distance z in the backward-pumping configuration for an amplifier of length L. The crosstalk level can exceed 1% ($-$20-dB crosstalk) for L >80 km and $G(L)$ >10. Since this crosstalk accumulates over multiple amplifiers, it can lead to large power penalties for undersea lightwave systems with long lengths.

Raman amplifiers can work at any wavelength as long as the pump wavelength is suitably chosen. This property, coupled with their wide bandwidth, makes Raman amplifiers quite suitable for WDM systems. An undesirable feature is that *the Raman gain is somewhat polarization sensitive*. In general, the gain is maximum when the signal and pump are polarized along the same direction but is reduced when they are orthogonally polarized. An approach to solve the polarization problem is pumping a Raman amplifier with two orthogonally polarized lasers. Another requirement for WDM systems is that the gain spectrum be relatively uniform over the entire signal bandwidth so that all channels experience the same gain. In practice, the gain spectrum is flattened by using several pumps at different wavelengths. Each pump creates the gain that mimics the spectrum shown in Fig. 1.6. The superposition of several such spectra then creates relatively flat gain over a wide spectral region. Bandwidths of more than 100 nm have been realized using multiple pump lasers.

Several other nonlinear processes can provide gain inside silica fibers [13]. An example is provided by the parametric gain resulting from FWM (Four-Wave Mixing). The resulting fiber amplifier is called a *parametric amplifier* and can have a gain bandwidth larger than 100 nm. Parametric amplifiers require a large pump power (typically >1 W) that may be reduced using fibers with high nonlinearities. They also generate a pahse-conjugated signal that can be useful for dispersion compensation. Fiber amplifiers can also be made using stimulated Brillouin scattering (SBS) in place of SRS [5]. The operating mechanism behind Brillouin amplifiers is essentially the same as that for fiber Raman amplifiers in the sense that both amplifiers are pumped backward and provide gain through a scattering process. Despite this formal similarity, Brillouin amplifiers are rarely used in practice because their gain bandwidth is typically below 100 MHz. Moreover, as the Stokes shift for SBS is $\sim$10 GHz, pump and signal wavelengths nearly coincide. These features render Brillouin amplifiers unsuitable for WDM lightwave systems although they can be exploited for other applications.

1.4 Polarization attraction

Nonlinear polarization pulling (NLPP) has been proposed as a way to control the state of polarization (SOP) of signals. It is based on optical nonlinear effects [13]. In particular, such a pulling can by obtained by exploiting Brillouin amplification, counterpropagating four-wave mixing processes, or fiber Raman amplifiers (FRAs). Moreover, depending on the actual configuration, some of the above effects may act together. More specifically, in FRAs, the signal component parallel to the pump experiences a higher Raman gain compared with the orthogonal component. This cumulative process along the fiber can realize the NLPP. Signal and pump can copropagate or counterpropagate in the fiber. Although copropagating schemes can achieve high signal repolarization, the synthetized output SOP is not predictable. On the contrary, in a counterpropagating scheme the signal output SOP is determined by the pump input SOP, and it is predictable.

1.4.1 Polarization attraction in counterpropagating schemes

In [14], the limitations of polarization attraction in counterpropagating randomly birefringent FRAs are numerically determined, taking into account the effects of nonlinear polarization rotation, pump depletion and orthogonal Raman gain. In that article, it is shown that a counterpropagating FRA is effective in attracting the signal toward a predetermined SOP settled by the pump input SOP. Moreover, it is shown that pump depletion plays an important role in achieving signal repolarization in high polarization mode dispersion (PMD) fibers, and that the maximum achievable mean degree of polarization (DOP) of the output signal is a function of the mean signal gain only.

In particular, the interaction of the signal $\overline{S}$ and of the backward propagating pump $\overline{P}$ is described in the Stokes space by the following equations [14]:

$$\begin{aligned}
\frac{d\overline{P}}{dz} &= \alpha_p \overline{P} + \frac{\omega_p}{\omega_s}\frac{g}{2}\left[S_0\overline{P} + P_0\overline{S} + \mu(3S_0\overline{P} + P_0\overline{S} - 2P_0\overline{S}_3)\right] \\
&\quad -(\underline{M}\,\omega_p\overline{b} + \overline{W}_p) \times \overline{P}\ , \qquad (1.27) \\
\frac{d\overline{S}}{dz} &= -\alpha_s \overline{S} + \frac{g}{2}\left[P_0\overline{S} + S_0\overline{P} + \mu(3P_0\overline{S} + S_0\overline{P} - 2S_0\overline{P}_3)\right] \\
&\quad +(\omega_s\overline{b} + \overline{W}_s) \times \overline{S}\ , \qquad (1.28)
\end{aligned}$$

where $P_0 = |\overline{P}|$, $S_0 = |\overline{S}|$, $\overline{P}_3 = P_3\hat{e}_3$ and $\overline{S}_3 = S_3\hat{e}_3$; the parameters are defined as follows: the signal and pump angular frequency are $\omega_s = 2\pi c/\lambda_s$ and $\omega_p = \omega_s + \Omega_R$, where $\lambda_s = 1550$ nm and $\Omega_R = 2\pi f_R$, $f_R = 13.2$ THz is the Raman frequency shift. The attenuation coefficients for the signal and pump are, respectively, $\alpha_s = 0.2$ dB/km and $\alpha_p = 0.273$ dB/km. The coefficient μ is the ratio between the orthogonal and parallel silica Raman gain coefficients. The vector $\omega\overline{b}$ describes the random linear birefringence of the fiber at frequency ω, and the matrix $\underline{M}$ = diag(1, 1, -1) accounts for the counterpropagation of the pump. The other coefficients account for the self- and cross-phase modulation [14].

In [14] the nonlinear system of (1.27) and (1.28) with the two boundary conditions $\overline{S}^{\text{in}} = \overline{S}(z=0)$, $\overline{P}^{\text{in}} = \overline{P}(z=L)$ is solved by a shooting algorithm. The PMD coefficient D is given by $D = 2\pi L_C\sqrt{2(\mathrm{e}^{-L/L_C} + L/L_C - 1)}/(\omega_s L_B\sqrt{L})$, where L_C, L_B and L are, respectively, the correlation, the beat and the fiber lengths. For a single fiber realization, the DOP of the output signal $\overline{S}^{\text{out}} = \overline{S}(z=L)$ is defined as

$$\text{DOP} = \frac{\sqrt{\sum_{i=1}^{3}\langle S_i^{\text{out}}\rangle_{\text{sop}}^2}}{\langle S_0^{\text{out}}\rangle_{\text{sop}}}\ , \tag{1.29}$$

where the average $\langle\cdot\rangle_{\text{sop}}$ is taken over 100 signal input random SOP uniformly distributed on the Poincaré sphere.

Fig. 1.9 shows the mean DOP of the output signal as a function of D obtained with numerical integration, with $L = 2$ km and $L_C = 10$ m. The signal input power is fixed at $S_0^{\text{in}} = 1$ mW; the pump input power P_0^{in} is varied from 1 W to 10 W, while the pump SOP is kept fixed at $\hat{P}^{\text{in}} = (1,0,0)^T$. Solid curves refer to the complete system of (1.27) and (1.28), whereas dashed curves refer to the undepleted pump approximation, which is achieved by neglecting the signal contributions in (1.27).

In the complete model in [14], for a fixed pump power the DOP is almost constant both for the very low and the high PMD regimes. For very low PMD, high DOP (>0.9) is achieved for pump input power higher than 3 W. In this region the effect of the birefringence is negligible and

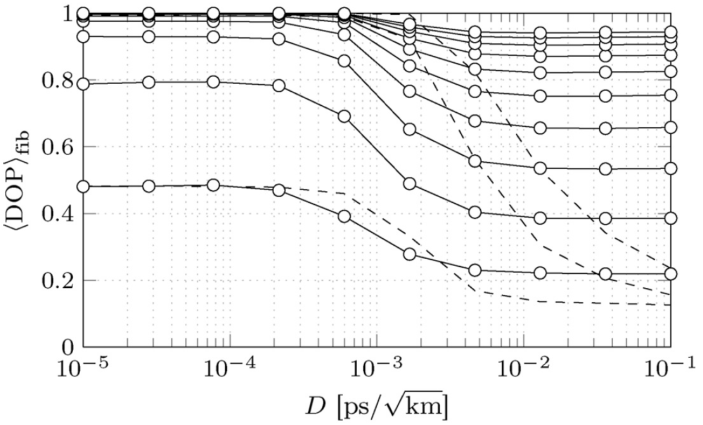

Figure 1.9: Mean signal output DOP as a function of the PMD coefficient D. The signal input power is $S_0^{\text{in}} = 1$ mW. The pump SOP is $\hat{P}^{\text{in}} = (1, 0, 0)^T$. Solid curves, from the bottom to the upper, correspond to pump input power P_0^{in} increasing from 1 W to 10 W, and refer to the complete system of (1.27) and (1.28). Dashed curves refer to the undepleted pump approximation, and correspond, from lower to upper, to $P_0^{\text{in}} = 1,\ 5,$ and 10 W. (From [14].)

the fiber can be considered isotropic. For increasing PMD, random birefringence reduces the effective Raman gain, lowering the DOP; nevertheless, DOP larger than 90% can still be reached for pump power higher than 8 W.

Pump depletion plays a crucial role in this system. In particular, if the undepleted regime is considered (dashed curves) the achievable DOP drastically decreases. The positive influence of depletion can be explained considering the term $\overline{\rho} = S_0\overline{P} + P_0\overline{S}$, which describes parallel Raman gain/depletion (see (1.27) and (1.28)). In fact, $\overline{\rho}$ acts in exactly the same way both on the pump and on the signal polarizations, forcing them to align each other. When the signal power is small compared to the pump power, the term $\overline{\rho}$ in (1.27) may be neglected, but when the signal power becomes comparable with the pump power, the same term gains importance. This effect is visible only for moderate to high PMD, because only in this regime Raman attraction is hampered by fiber birefringence. Indeed, in copropagation the term $\overline{\rho}$ acts on pump and signal with opposite signs [16]. Therefore, in copropagation depletion hampers polarization attraction.

Defining the main gain G as $G = \langle \langle S_0^{\text{out}} \rangle_{\text{sop}} / S_0^{\text{in}} \rangle_{\text{fib}}$, it is interesting to observe the variations of the mean signal output DOP and the mean gain G as a function of the fiber length L. Fig. 1.10(a) and (b) shows these functions, for $D = 0.05$ ps/$\sqrt{\text{km}}$. We may note that for high sinal power an increase of the fiber length does not increase significantly Raman amplification and pulling; on the other hand, the increased fiber length enhances the scrambling effect of PMD, worsening the PMD. Clearly the lower the saturation value of the gain, the stronger this effect.

Fig. 1.10(c) shows the mean of the angle θ between the mean signal output SOP, $\langle \hat{S}^{\text{out}} \rangle_{\text{sop}}$, and the pump input, SOP, $\underline{M}\hat{P}^{\text{in}}$. Actually, $\langle \theta \rangle_{\text{fib}}$ indicates that effectively the signal, when attracted, is attracted toward the pump, thus overcoming the unpredictability of synthetized SOP

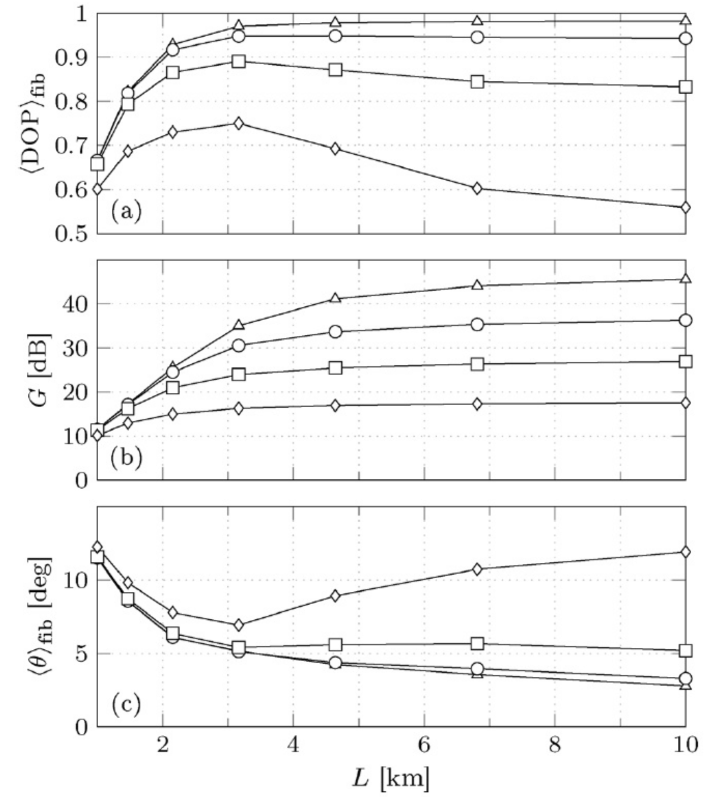

Figure 1.10: (a) Mean signal output DOP, (b) gain G, and (c) signal-pump angle θ as a function of the fiber length. Triangles, circles, squares and diamonds refer to signal input power $S_0^{\text{in}} = 0.1, 1, 10,$ and 100 mW, respectively. (From [14].)

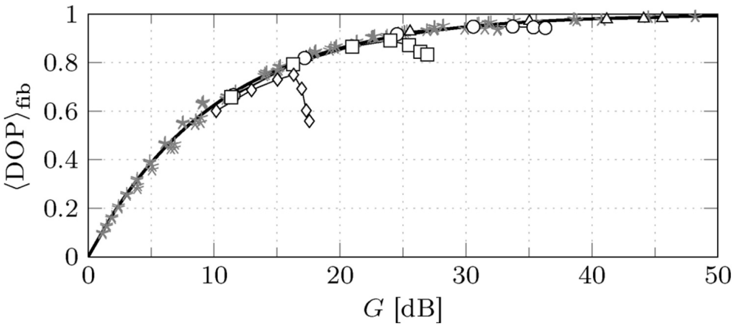

Figure 1.11: Mean DOP as a function of the signal gain G, for a PMD coefficient $D = 0.05$ ps/$\sqrt{\text{km}}$. Stars are obtained by varying fiber length L in the range from 1 to 10 km and pump (signal) input power in the range from 1 to 5 W (0.01 to 1 mW). (From [14].)

of copropagating schemes [16].

Fig. 1.11 shows the signal output mean DOP as a function of the mean gain G, defined above. The empty marks refer to the curves of Fig. 1.10, whereas the stars are obtained by varying the fiber length and the input power of signal and pump. In [14], the data have been empirically interpolated by the following function:

$$\langle\mathrm{DOP}\rangle_{\mathrm{fib}} = 1 - \mathrm{e}^{-G_{\mathrm{dB}}/\Gamma} , \tag{1.30}$$

where $G_{\mathrm{dB}} = 10\log_{10} G$ and $\Gamma \approx 10.2$ (solid curves in the figure). Actually,(1.30) provides an estimate of the expected output DOP for a given mean gain G, or, conversely, it provides the required gain to reach a desired DOP. That specific gain can be obtained by appropriately choosing the fiber length, the signal and pump input powers in such a way that the gain does not saturate. For example, a gain of about 25 dB is sufficient to have DOP > 0.9, with a dispersion $D = 0.05$ ps/$\sqrt{\text{km}}$ (standard fibers).

Chapter 2

Polarimetric techniques and systems, and polarization scramblers

After having presented the concept of polarization, with its main characteristics and important aspects, we introduce the methods for measuring it. In particular, the focus is on the classic quarter-wave plate polarimeter, which is a simple polarimetric method we use in our experimental tests. This polarimeter is based on a quarter-wave plate followed by a polarizer. The measurement of the SOP is obtained by analytical calculations from the detected power.

The second part of the Chapter deals with the concept of polarization scrambling, which permits to actively change the SOP using polarization modulation method. The principles of scrambling are introduced, explaining the reasons for which it is employed. The most common types of scramblers are described, underlining their advantages and disadvantages. A detailed overview of the applications of the scramblers is presented, illustrating some of the experimental setups in which they are employed.

2.1 Polarimetric techniques and systems

A *polarimeter* is an optical instrument used to determine the polarization state of a light beam. The polarimeter plays a key role for example for PMD measurements in an optical fiber. There are two groups of polarimeters: 1) the space-division mode and 2) the time-division mode. In the first group, the light is split int four beams, which are processed in parallel, whereas the second group uses a rotation stage to adjust the polarization components.

There are different optical setups used to measure the polarization state of light. The criteria in selecting a polarimetric arrangement are simplicity, accuracy, precision and stability. A classic polarimetric setup is constituted by a quarter-wave plate followed by a linear polarizer, described for example by Collett ([3]). There are many setups similar to this one, for example the rotating wave plate Stokes' polarimeter, which is used for PMD measurements at the National Institute

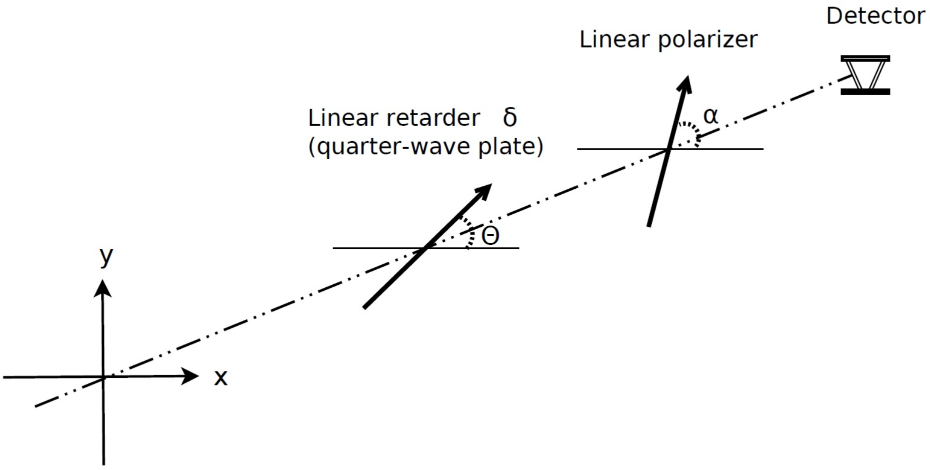

Figure 2.1: Schematic layout of the polarimeter. The quarter-wave plate is mounted on a rotation stage with azimuth θ, δ is the retardation angle, and α is the linear polarizer azimuth. The reference for azimuths is the x-axis.

of Standard and Technology.

Now we describe and study the classic quarter-wave plate polarimeter, which is used in our experiments described in the next Chapters. The setup has two optical elements: a quarter-wave plate (linear retarder) and a linear polarizer, as depicted in Fig. 2.1. Both optical elements are mounted in two rotation stages, which enable full control of the azimuth for each optical element. These two optical elements can be included in a single device, called Polarization Controller (PC), which enables to control them separately. The coordinate system used in the analytical model of the polarimeter is presented in Fig. 2.1.

The Müller matrix for a linear retarder with a phase shift of δ and a fast axis (i.e., that direction having a low refractive index) with an azimuth of θ with respect to the coordinate system described in Fig. 2.1 is given in the following expression (2.1):

$$\mathbf{M}(\delta,\theta) = \begin{pmatrix} 1 & 0 & 0 & 0 \\ 0 & \cos(4\theta)\sin^2(\delta/2)+\cos^2(\delta/2) & \sin(4\theta)\sin^2(\delta/2) & -\sin(\delta)\sin(2\theta) \\ 0 & \sin(4\theta)\sin^2(\delta/2) & \cos^2(\delta/2)-\cos(4\theta)\sin^2(\delta/2) & \sin(\delta)\cos(2\theta) \\ 0 & \sin(\delta)\sin(2\theta) & -\sin(\delta)\cos(2\theta) & \cos(\delta) \end{pmatrix} \tag{2.1}$$

The Müller matrix associated with an ideal quarter-wave plate can be found when the phase shift between the two components of the optical beam (divided by the birefringent wave plate) is

$\delta = \pi/2$. In this case we found that

$$\mathbf{M}(\delta,\theta) = \begin{pmatrix} 1 & 0 & 0 & 0 \\ 0 & \frac{1}{2}(1+\cos(4\theta)) & \frac{1}{2}\sin(4\theta) & -\sin(2\theta) \\ 0 & \frac{1}{2}\sin(4\theta) & \frac{1}{2}(1-\cos(4\theta)) & \cos(2\theta) \\ 0 & \sin(2\theta) & -\cos(2\theta) & 0 \end{pmatrix} . \tag{2.2}$$

For a linear polarizer that is rotated with an azimuth α, as indicated in Fig. 2.1, the Müller matrix is

$$\mathbf{P}(\alpha) = \frac{1}{2}\begin{pmatrix} 1 & \cos(2\alpha) & \sin(2\alpha) & 0 \\ \cos(2\alpha) & \cos^2(2\alpha) & \cos(2\alpha)\sin(2\alpha) & 0 \\ \sin(2\alpha) & \cos(2\alpha)\sin(2\alpha) & \sin^2(2\alpha) & 0 \\ 0 & 0 & 0 & 0 \end{pmatrix} . \tag{2.3}$$

The output Stokes' vector emerging from the linear polarizer $\mathbf{P}$, just before the photodetector, can be expressed by the following matrix product, as explained in Sec. 1.1.1:

$$\bar{S}_{\text{out}} = \mathbf{P}(\alpha)\cdot\mathbf{M}(\delta,\theta)\cdot\bar{S}_{\text{in}} \;, \tag{2.4}$$

where $\bar{S}_{\text{in}} = (s_0, s_1, s_2, s_3)$ is the Stokes' vector at the input of the quarter wave plate.

The measurable intensity is enclosed in the first term of the output Stokes' vector. In fact, the intensity measured by a detector after a quarter-wave plate and a polarizer is the first Stokes' parameter of the output beam that travels through the optical system. By selecting a horizontal position for the polarizer ($\alpha = 0$) and an ideal quarter-wave plate ($\delta = \pi/2$) the intensity of the output beam is

$$I\left(s_0, s_1, s_2, s_3, \frac{\pi}{2}, \theta, 0\right) = \frac{s_0}{2} + \frac{s_1}{2}\left(\frac{1}{2} + \frac{1}{2}\cos(4\theta)\right) + \frac{s_2}{4}\sin(4\theta) - \frac{s_3}{2}\sin(2\theta) \tag{2.5}$$

where the Stokes' parameters s_0, s_1, s_2, and s_3 can be calculated using the intensity versus the azimuth of the quarter-wave plate. Putting this system after an optical fiber, the measurement of intensity (optical power) enables the determination of all the Stokes' parameters of the light at the output of the fiber.

Given the intensity versus the quarter-wave plate azimuth ($I(\theta)$), the Stokes' parameters are calculated by the analysis of the Fourier coefficients. From this analysis, the following expressions are obtained:

$$\begin{aligned} s_0 &= \frac{1}{\pi}\left(\int_0^{2\pi} I(\theta)d\theta - 2\int_0^{2\pi} I(\theta)\cos(4\theta)d\theta\right) \\ s_1 &= \frac{4}{\pi}\int_0^{2\pi} I(\theta)\cos(4\theta)d\theta \\ s_2 &= \frac{4}{\pi}\int_0^{2\pi} I(\theta)\sin(4\theta)d\theta \\ s_3 &= -\frac{2}{\pi}\int_0^{2\pi} I(\theta)\sin(2\theta)d\theta \;. \end{aligned} \tag{2.6}$$

Analogous relations apply even if the optical intensity $I(\theta)$ is measured only in correspondence of N_{ang} angles chosen in this way: $\theta_k = \pi k/N_{\text{ang}}$, for $k = 0, 1, \ldots, N_{\text{ang}}-1$, with $N_{\text{ang}} \geq 4$. In this case, in effect, it suffices to replace the integral operators with sums to obtain exactly the same relations. This fact derives from the following equality, which can be simply verified:

$$\sum_{k=0}^{N_{\text{ang}}-1} e^{jM\theta_k} = \frac{1-e^{jM\pi}}{1-e^{jM\pi/N_{\text{ang}}}} = 0 \ , \qquad \forall\ M \text{ even integer} \ . \tag{2.7}$$

2.2 Polarization scramblers

Polarization property of light beams is an important factor in high-speed optical communication network system design. As the bit rate increases, fiber optic communication systems have become increasingly sensitive to polarization related impairments. Such impairments include polarization mode dispersion (PMD) in optical fibers, polarization dependent loss (PDL) in passive optical components, polarization dependent modulation (PDM) in electro-optic modulators, polarization dependent gain (PDG) in optical amplifiers, polarization dependent center wavelength (PDW) in WDM filters, polarization dependent response (PDR) in receivers, and polarization dependent sensitivity (PDS) in sensors and coherent communication systems.

Polarization scrambling can be used to mitigate many polarization related impairments. It is called *scrambled* if the SOP of a totally polarized light is made to vary randomly at a relatively low rate. At any instant of time, the SOP is well defined and DOP is close to 1. However, on a time average, DOP is close to zero. Therefore, the DOP of a scrambled light depends on the average time or the detection bandwidth of the observer ([18]). This is a crucial point for measuring polarization.

2.2.1 Principles of polarization scrambling

A polarization scrambler actively changes the SOP using polarization modulation method. Several polarization scramblers based on different technologies are available today, including $LiNbO_3$ based scramblers, resonant fiber coil based scramblers, and fiber squeezer based scramblers, as depicted in Fig. 2.2.

$LiNbO_3$ scramblers use electro-optic effect to modulate the state of polarization. For example, a $LiNbO_3$ phase modulator can be used as a scrambler when the input SOP is linearly polarized 45 degrees with respect to the applied modulation electric field. Such a scrambler is of high speed, however, suffers from high insertion loss, high PDL, high residual amplitude modulation (activation loss), high sensitivity to input polarization state, and high cost due to inserting a waveguide in the fiber line. Multiple modulation sections with different electric field directions, as shown in Fig. 2.2A, may be used to make the device less polarization sensitive but with increased complexity and cost.

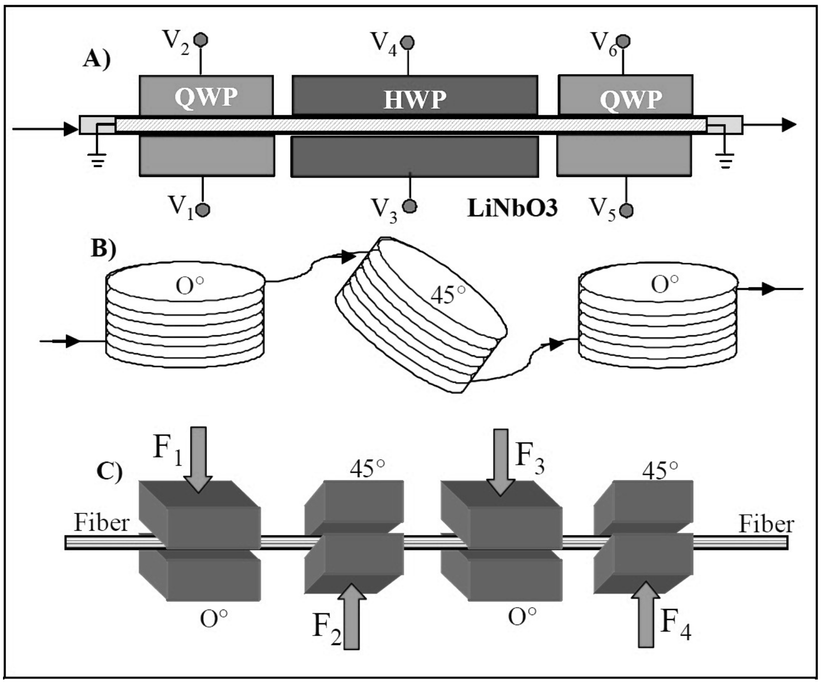

Figure 2.2: Illustration of different polarization scramblers. A) $LiNbO_3$ based, B) Fiber resonant coil based, and C) fiber squeezer based. (From [18].)

Resonant fiber coil based scrambler is constructed by winding fiber around an expandable piezoelectric cylinder. Applying an electric field to the cylinder causes it to expand, which in turn induces a birefringence in the fiber via photo-elastic effect. If the frequency of the electrical field is in resonance with the piezo-electric cylinder, the induced birefringence will be large enough to cause sufficiently large polarization modulation with a relatively low voltage applied. In practice, multiple fiber cylinders with different orientations may be cascaded to make the scrambler less polarization sensitive, as show in Fig. 2.2B. Compared with the $LiNbO_3$ scramblers, the expanding fiber coil based scramblers have the advantages of low insertion loss, low PDL, and low cost. On the other hand, they suffer from large size, low scrambling speed, and large residual phase modulation resulting from the significant fiber stretching when the fiber coil expands.

Squeezing fiber can induce large birefringence in the fiber via photo-elastic effect and cause large polarization modulation if the input polarization is 45 degrees from the squeezing axis. Polarization insensitive scrambler can be constructed by cascading multiple fiber squeezers oriented 45 degrees from each other, as shown in Fig. 2.2C. The device can be operated either resonantly at higher scrambling frequencies or non-resonantly at lower scrambling frequencies. Compared with the $LiNbO_3$ scrambler, the device has the benefit of low insertion loss, low PDL, and low cost. Compared with the fiber coil scrambler, it has the advantage of small size, low residual phase modulation, and scrambling flexibility. In addition, it has the advantage of low residual phase modulation and residual amplitude modulation (activation loss) over both the $LiNbO_3$ and fiber coil scramblers. Low residual phase modulation is important for avoiding interference related noise in optical systems and low residual amplitude modulation is critical for using the scrambler for PDL and DOP measurement of optical devices.

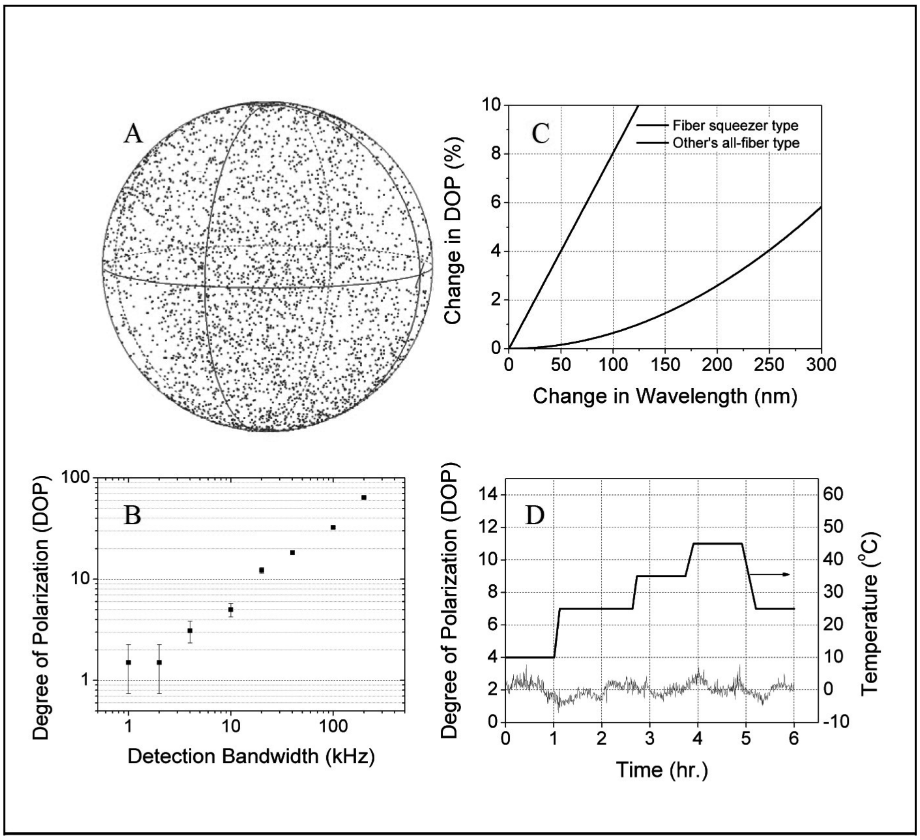

Figure 2.3: Typical fiber squeezer based scrambler performance data. (From [18].)

The performance of the scrambler is generally measured by the degree of polarization (DOP) of the scrambled light over a certain period of time and the uniformity of the SOP Poincaré sphere coverage. In practice, the wavelength sensitivity and temperature sensitivity of the performance of the scrambler are also important for real world applications. Fig. 2.3A shows the (excellent) scrambling uniformity on the Poincaré Sphere of a General Photonics scrambler, while Fig. 2.3B shows its DOP as a function of detector bandwidth. The wavelength sensitivity is illustrated in Fig. 2.3C. As can be seen, a multi-stage fiber squeezer scrambler is much less sensitive to wavelength changes. Experimental results also indicate that the fiber squeezer scrambler is less sensitive to temperatures changes, as shown in Fig. 2.3D.

Operation lifetime is always an important parameter to consider for system and industrial applications. Indeed, without proper treatment and protection, the fiber may break in a short period of time. Some constructors have spent a great deal of effort in finding fiber failure mechanisms under stress and corresponding methods for protection. For example, General Photonics declares that with its proprietary and patented fiber protection recipe, the fiber in their squeezers under maximum operation stress has an estimated mean time to failure (MTTF) of 2 billion years. Such a result could be understood considering that the stress in a polarization-maintaining fiber induced by the two stress rods is on the same order of magnitude as the stress applied to the fiber by the fiber squeezer. In our continued endurance test, the fiber squeezers have passed one trillion (1012) activation cycles and the number is expected to rise as the test continues.

Scramblers can also be classified by the driving frequency. For fiber squeezer based scramblers, the driving frequencies of the different squeezers are different. To obtain the best result, they should not be the harmonic or sub-harmonic of each other. For some scramblers, the driving frequencies of the scramblers are factory-set and cannot be changed. Therefore, the scrambling rate for such scramblers is fixed. Such scramblers are generally designed for the highest possible scrambling rate by using the resonant nature of the piezo-electric transducers. Also miniature scramblers for hand-held and field instrument have been designed. For this type of scramblers, the scrambling rate can be changed from a few hertz to few tens of kilohertz either by a push bottom switch or via a computer command.

2.2.2 Applications of polarization scramblers

Polarization scramblers have numerous applications in optical communication networks, fiber sensor systems, and test and measurement systems. As shown in Fig. 2.4A, a polarization scrambler can be used at the transmitter side to minimize polarization-dependent gain (PDG) of Erbium doped fiber amplifiers (EDFA) in ultra-long haul systems. For this application, the scrambling rate should be significantly faster than the inverse of the gain recover time constant of the fiber amplifiers (on the order of 10 kHz).

The scramblers can also be used to assist the monitoring of PMD in a WDM system, as illustrated in Fig. 2.4B. Generally speaking, the PMD can be monitored by measuring the degree of polarization (DOP) of the optical signal propagated through the fiber. Small DOP usually indicates a large PMD effect. However, such a measurement may be erroneous if the input SOP to the transmission fiber is substantially aligned with the principal state of polarization (PSP) of the fiber. For such a situation, the measured DOP is always large. A scrambler at the transmitter side can be used to effectively eliminate such an anomaly. Furthermore, it enables a polarimeter in the PMD compensator at the receiver side to identify the PSP, which in turn speed up PMD compensation. Other optical network applications include signal to noise ratio monitoring of WDM channels if a polarizer is placed after a scrambler.

Polarization scrambler can also be used to eliminate the polarization fading of a fiber sensor, as shown in Fig. 2.4C. In such a system, the envelope of the response curve is independent of the polarization fluctuation.

Placing a scrambler in front of a polarization sensitive instrument, such as a diffraction grat-

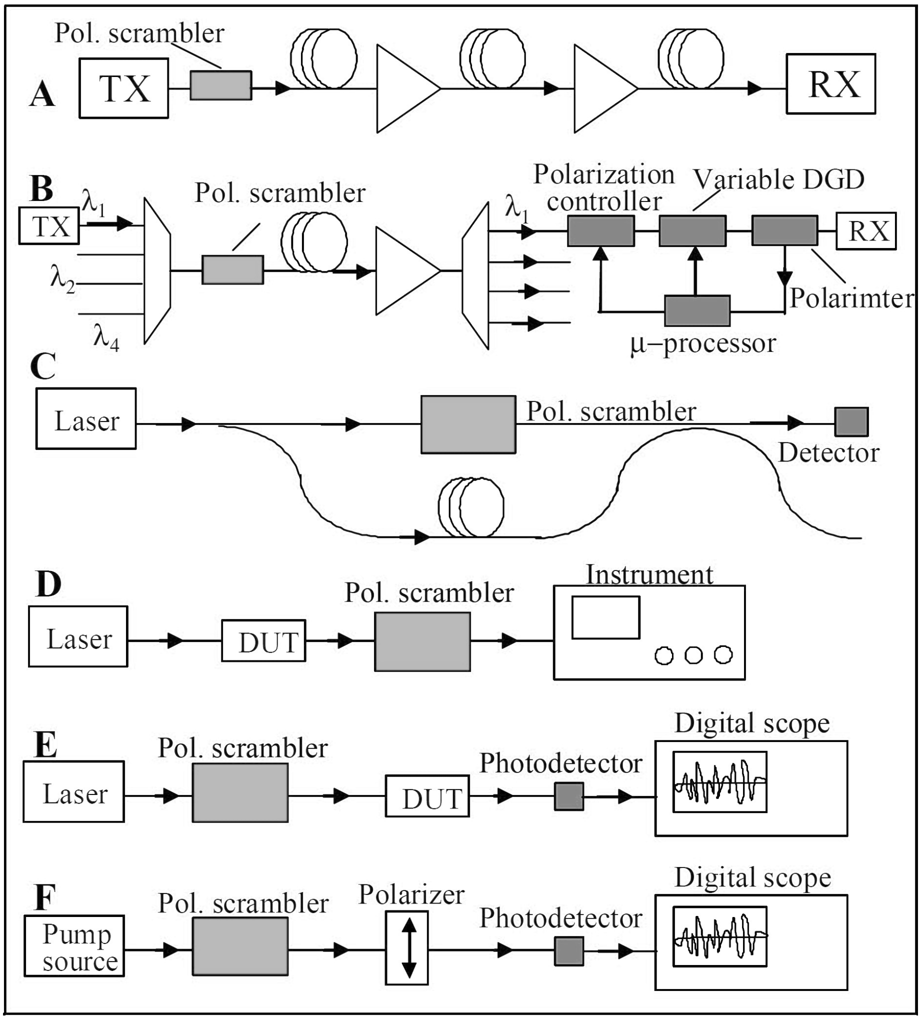

Figure 2.4: Illustration of different applications of polarization scramblers. (From [18].)

ing based optical spectrum analyzer (OSA), can effectively eliminate its polarization dependence, as shown in Fig. 2.4D, if the scrambling rate is sufficiently faster than the detector speed in the instrument. In addition, as illustrated in Fig. 2.4E, polarization scramblers can be used to measure the polarization-dependent loss (PDL) of a device under test (DUT) with the help of a digital scope.

Raman amplifiers generally exhibit strong PDG if the pump laser is highly polarized. To minimize the PDG, a depolarized pump source must be used. The DOP of the pump source directly relates to the PDG of the amplifier and therefore must be carefully characterized. DOP can be measured using expensive polarimeter-based polarization analyzing instruments. However, such instruments are not accurate for low DOP (<5%) sources. Polarization scrambler again can be used to accurately measure the DOP with a digital scope, as illustrated in Fig. 2.4F. Assuming the maximum and minimum voltages measured with the digital scope are V_{max} and V_{min} respectively, it can be demonstrated that the DOP of the light source can be calculated using the following formula:

$$\mathrm{DOP} = \frac{V_{\mathrm{max}} - V_{\mathrm{min}}}{V_{\mathrm{max}} + V_{\mathrm{min}}}\,. \tag{2.8}$$

It can be observed that this is another simple method for DOP measuring, alternative to that presented in Sec. 2.1. In this setup there is not the necessity of a rotational stage thanks to the polarization scrambling.

In summary, polarization scramblers are important devices for fiber optic communications, fiber sensors, and fiber optic test and measurement applications. With low insertion loss, low back reflection, low residual amplitude and phase modulation, low wavelength and temperature sensitivity, low cost, and small form factor, fiber squeezer based scrambler modules are specially suited for OEM applications, where they can be readily integrated into various network equipment, fiber sensor systems, and test and measurement instruments.

Chapter 3

A polarimetric system with a polarized input signal

In this Chapter there is a description of the experimental activities performed to test and characterize a polarimetric system in various configurations with a polarized input signal. The acquired data are elaborated to evaluate its accuracy. An interesting drift effect, which had a strong influence on polarization measurements, is described and studied too. Many of the concepts explained in the two previous Chapters about polarization and polarimetric techniques are used here.

From an experimental viewpoint, in particular, power measurements, which are necessary to measure the SOP employing the polarimetric technique explained in Chapter 2, are performed employing two different optical instruments. This aspect, which is mainly due to the necessity of have information on the spectral composition of the signals, makes necessary certain precautions and considerations on polarization measurements.

3.1 Initial experimental setup

In this first step of measurements, we want to test a polarimetric system in its initial configuration. The experimental configuration and activities are explained in detail.

The optical source is tuned at $\lambda_S = 1640$ nm, the polarimetric system is formed by a Polarization Controller (PC) followed by an Optical Power Meter (PM). Instruments are connected via GPIB to a computer. In particular, the experimental setup is constituted by these devices:

- Laser source (tunable): *Anritsu TUNICS-Plus*;
- Polarization Controller: *HP8169A*;
- Optical Power Meter: *ILX-Lightwave FPM-8210*;
- Fiber optic patch cords, FC/APC type, length 1 m.

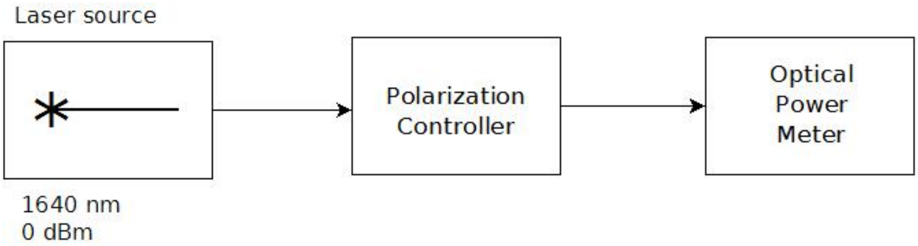

Figure 3.1: Initial configuration with laser source and the polarimetric system. The quarter-wave plate of the PC is rotated to measure the SOP of the signal.

In Fig. 3.1 is schematically represented the experimental configuration.

The generated incoherent and polarized optical signal is nominally centered at $\lambda_S = 1640$ nm, with a linewidth of 150 kHz and a total power of 0 dBm.

Initially the angles of rotation of the polarizer and of the half-wave plate of the PC are set to $0°$ for simplicity. Quarter-wave plate is instead uniformly rotated from $0°$ to $(180° - 180°/N_{\text{ang}})$, by angles of $180°/N_{\text{ang}}$, with N_{ang} to be chosen properly. This realizes the so called *HQP technique* for the measure of the *State of Polarization* (SOP) of a signal. This technique is formally explained in Chapter 2.

The built-in display filter of the power meter is set in "medium" modality, for which the instrument acquires 10 samples during intervals of 0.5 s and provides the arithmetic mean of their values. For a measurement of SOP, N_{ang} measurements of optical power are required. Consequently it is useful that the PM operates in a sufficiently rapid modality.

As mentioned above, the aim of this experimental step is to measure and characterize the uncertainty on the measurements of SOP and DOP as a function of few fundamental parameters, in particular N_{ang}. Nevertheless, during some preliminary tests it has been evident that the system drifts with the temperature, i.e. the measurements variate with the environment temperature. This effect, here named *temperature drift*, must be studied and characterized, at least in some important cases, as in 3.1.1.

3.1.1 Temperature drift of the experimental setup

To study this temperature effect it is necessary to do a simplification. We arbitrarily set $N_{\text{ang}} = 6$ for the polarimetric system, providing that other values for this parameter will be tested in the next experimental step. Moreover, the temperature test is made for $\lambda_S = 1640$ nm and repeated for $\lambda_S = 1550$ nm, to observe eventual variations. The test starts about ten minutes after turning on the instruments, and it ends after about an hour; during this time period, the room temperature is varied by the air conditioning system to cover a sufficiently wide interval of values, and it finally stabilizes. The environment temperature is measured by a standard 0.1 °C-accuracy thermometer, which is positioned near the instrumentation. It must be noticed that also the temperature insides the packages of the instruments should be measured because it is

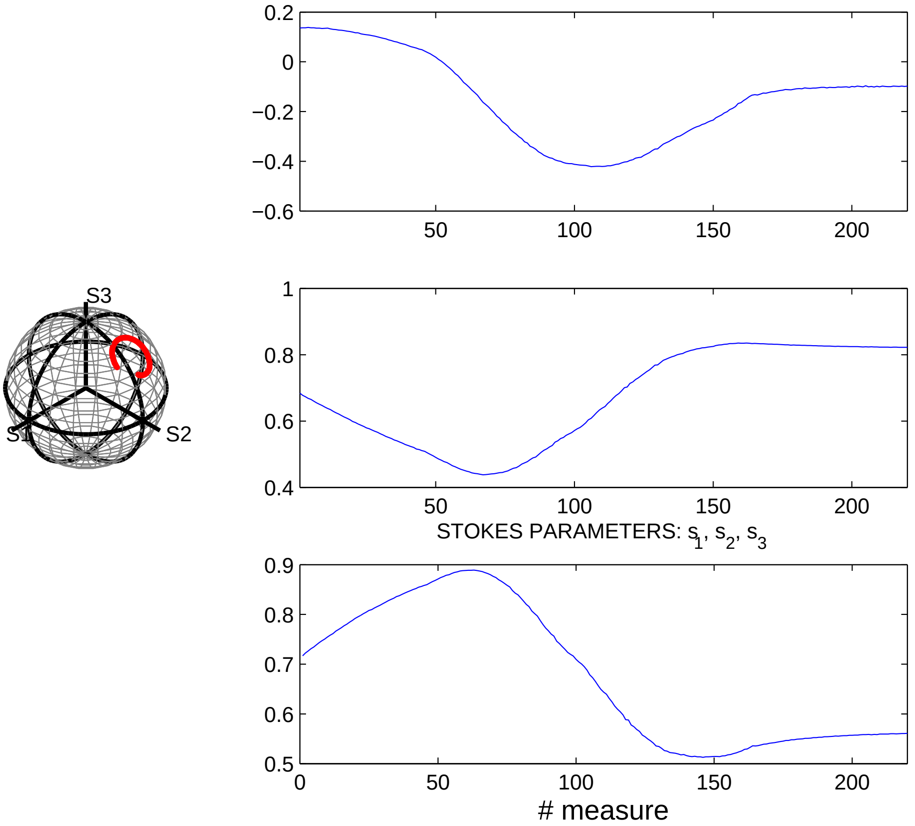

Figure 3.2: SOP evolution with the corresponding Poincaré sphere during the test at $\lambda_s = 1640$ nm (the same of Figg. 3.3 and 3.4). The x-axis corresponds to the time interval [0, 63] minutes. The Stokes' parameters, constituting the SOP, are *normalized* to s_0.

probably different from the room temperature, but such a measurement could be very difficult to do without proper instrumentation.

In the first test we set $N_{\text{ang}} = 6$ and $\lambda_s = 1640$ nm. It lasts 65 minutes, that correspond to 220 measurements of SOP and DOP, provided by the polarimetric system and the numerical analysis. Measured SOPs (Stokes' parameters s_1, s_2, s_3) during the test and the corresponding Poincaré sphere are represented in Fig. 3.2; measured DOPs and the temperature evolution during the test are represented in Figg. 3.3 and 3.4, respectively. We observe that the minimum temperature is 18.5 °C and the maximum is 22.9 °C.

In the second test, made in a different day, we set $N_{\text{ang}} = 6$ and $\lambda_s = 1550$ nm. It lasts 55 minutes, that correspond to 193 measurements of SOP and DOP, provided by the polarimetric system and the numerical analysis. Measured SOPs (Stokes' normalized parameters s_1, s_2, s_3) during the test and the corresponding Poincaré sphere are represented in Fig. 3.5; measured DOPs and the temperature evolution during the test are represented in Figg. 3.6 and 3.7, respectively. It can be noted that the minimum temperature is 18.4 °C and the maximum is 23.5 °C.

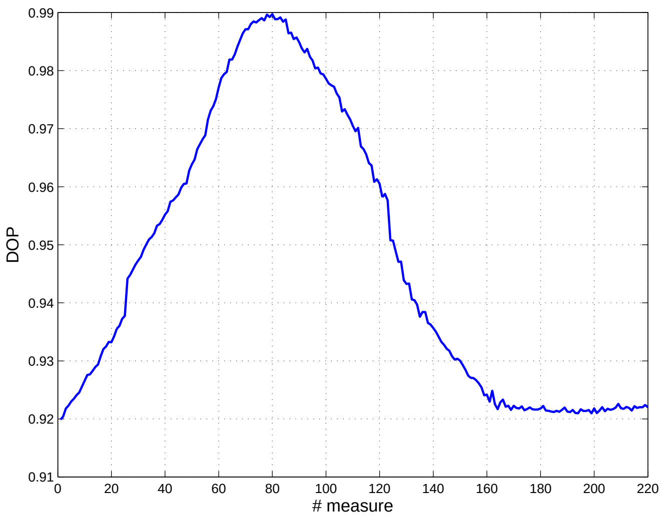

Figure 3.3: DOP evolution during the test at $\lambda_s = 1640$ nm.

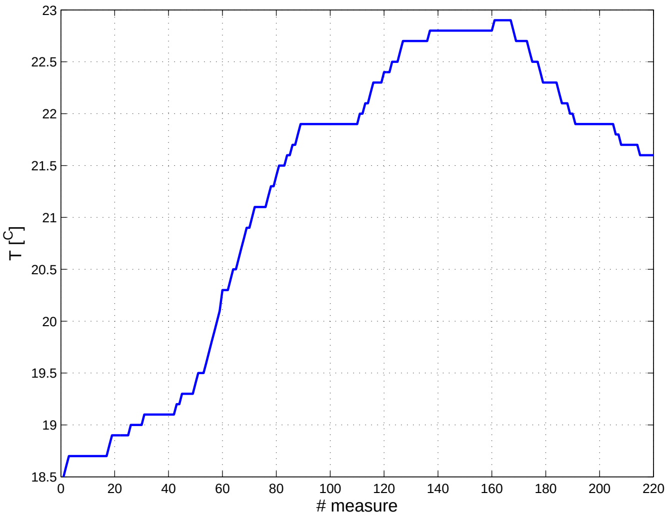

Figure 3.4: Room temperature evolution during the test at $\lambda_s = 1640$ nm.

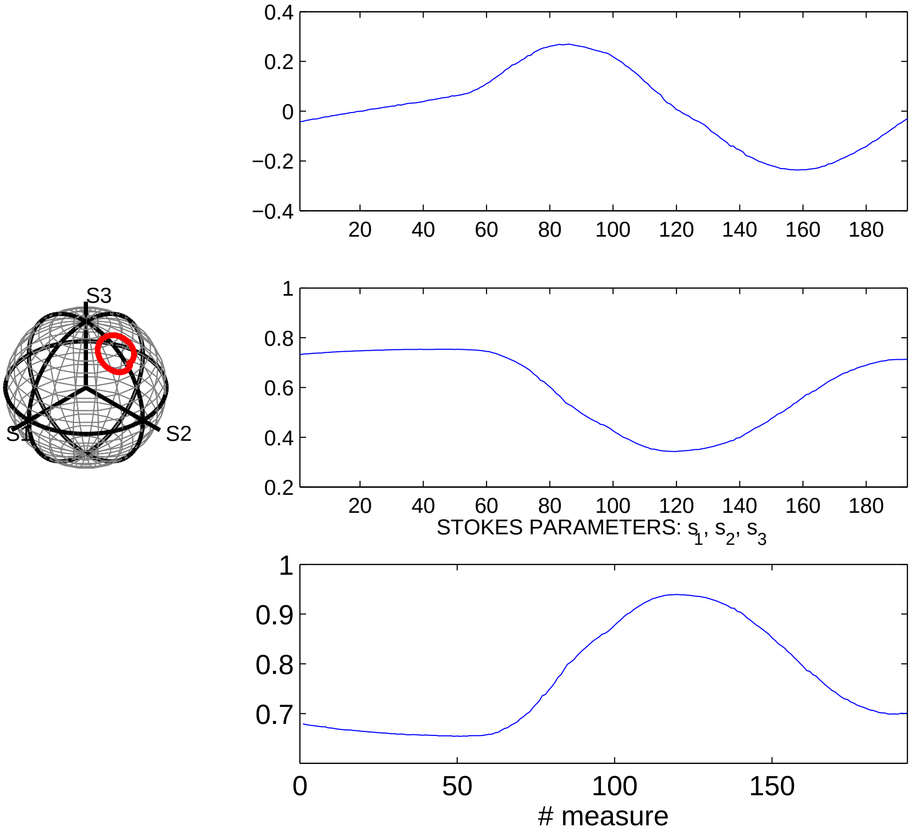

Figure 3.5: SOP evolution with the corresponding Poincaré sphere during the test at $\lambda_s = 1550$ nm (the same of Figg. 3.6 and 3.7). The x-axis corresponds to the time interval [0, 55] minutes. The Stokes' parameters, constituting the SOP, are *normalized* to s_0.

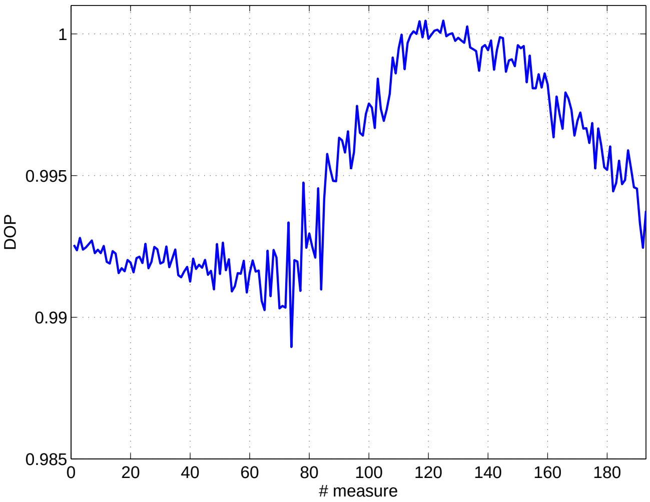

Figure 3.6: DOP evolution during the test at $\lambda_s = 1550$ nm.

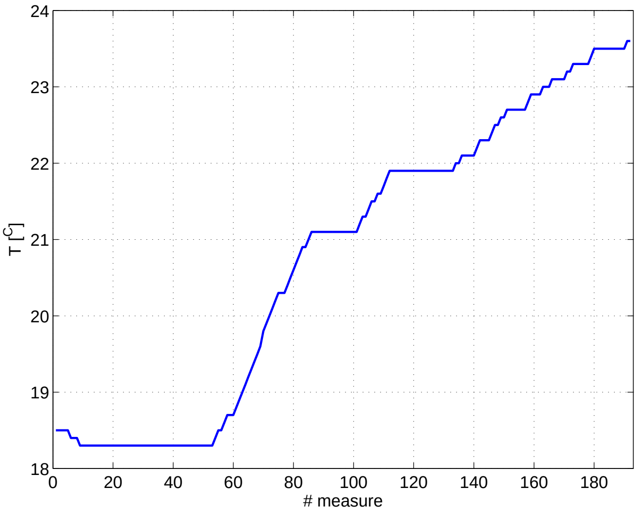

Figure 3.7: Room temperature evolution during the test at $\lambda_s = 1550$ nm.

The following observations are deduced:

- a strong dependence of the measurements of SOP and DOP on the temperature has been proven. In particular, although this dependence is difficulty quantifiable, the measured value of DOP increases with the temperature, even if the source has constant polarization. This effect could impair the quality of the measurements. Consequently, during the experimental steps, the temperature should be kept as constant as possible. This could be not possible, therefore the *temperature drift* effect will be compensated by numerical analysis, assuming constant temperature in sufficiently short temporal intervals;

- the *temperature drift* effect appears in both the considered values of the laser emission wavelength ($\lambda_s = 1640$ nm and 1550 nm).

For the sake of completeness, we make another experimental test, in which the temperature variations are not very large. In particular, by manually controlling the air conditioning system of the room, 0.3-degree temperature fluctuations around 24.6 °C are obtained. It must be underlined that this temperature control is difficulty repeatable. This test lasts 114 minutes, that correspond to 400 measurements of SOP and DOP, provided by the polarimetric system and the numerical analysis. Measured SOPs (Stokes' parameters s_1, s_2, s_3) during the test and the corresponding Poincaré sphere are represented in Fig. 3.8; DOP evolution is depicted in Fig. 3.9. It is evident that the variations of SOP and DOP are much smaller than the two previous cases.

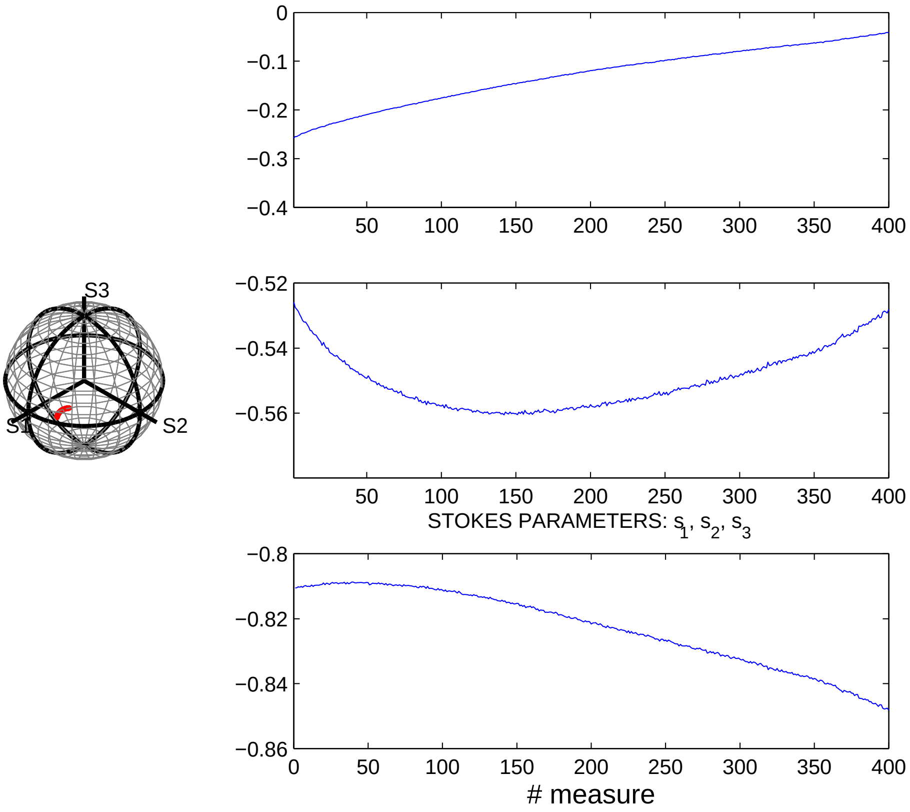

Figure 3.8: SOP evolution with the corresponding Poincaré sphere during the test at $\lambda_s = 1640$ nm with small fluctuations of temperature (the same test of Fig. 3.9). The x-axis corresponds to the time interval [0, 114] minutes. The Stokes' parameters, constituting the SOP, are *normalized* to s_0.

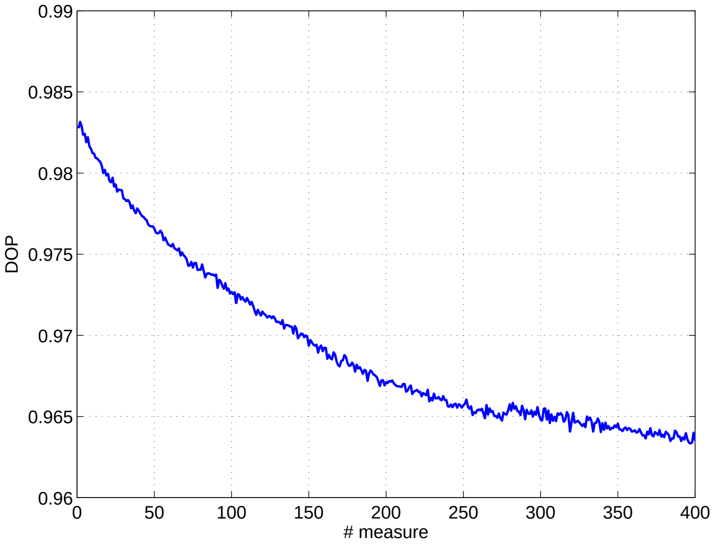

Figure 3.9: DOP evolution during the test at $\lambda_s = 1640$ nm with small fluctuations of temperature.

3.1.2 Evaluation of the optimal value of N_{ang}

In this step the experimental setup is the same as the previous tests (Fig. 3.1), as explained in the introduction of this section. Laser source, PC and PM are configured in the same way. The room temperature is kept as constant as possible, to reduce the effect of the *temperature drift*, which unfortunately is always present. We perform in succession these experimental sets:

- 400 measurements of SOP (total duration 94 min), with $N_{\text{ang}} = 5$;
- 400 measurements of SOP (total duration 113 min), with $N_{\text{ang}} = 6$;
- 400 measurements of SOP (total duration 181 min), with $N_{\text{ang}} = 7$.

The third set lasts much longer because the Polarization Controller approximates the angle $180°/7$ producing a delay in the execution of the controller software script. Since the durations of the set of measurements are not short, the effect of the drift cannot be neglected, i.e. the mean value of the SOP tends to vary slightly. Consequently, we proceed to a statistical analysis based on consecutive time windows, each one with a duration of 5, 15, 30 or 60 minutes; we consider also a time window of 181 minutes, which is equivalent to an analysis without time windowing. The idea beyond this approach is to compensate the effect of the drift assuming constant SOP and DOP during a single time window. More precisely, defining $\overline{\text{SOP}}_i = \left(\overline{s_{1,i}}\,, \overline{s_{2,i}}\,, \overline{s_{3,i}}\right)$ the mean value of the SOP in the time window i, in each of the *analysis time windows* we calculate this quantity

$$error_{\text{SOP},i} = \frac{\sqrt{\left(s_1 - \overline{s_{1,i}}\right)^2 + \left(s_2 - \overline{s_{2,i}}\right)^2 + \left(s_3 - \overline{s_{3,i}}\right)^2}}{\sqrt{\left(\overline{s_{1,i}}\right)^2 + \left(\overline{s_{2,i}}\right)^2 + \left(\overline{s_{3,i}}\right)^2}} \tag{3.1}$$

which corresponds to the Euclidean distance d between the "instantaneous" SOP and $\overline{\text{SOP}}_i$, with d normalized to the norm of $\overline{\text{SOP}}_i$. The normalization is performed precisely to compensate the effect of temporal variation of the SOP. The value of $error_{\text{SOP}}$ gives an indication of the error that is committed on the measurement of the SOP, as a function of N_{ang} and of the duration of the analysis time window.

From the measurements of SOP collected in the three experimental sets described above, we calculate $error_{\text{SOP}}$ for all the values of N_{ang} and of the duration of the windows. In Fig. 3.10 there are the histograms of $error_{\text{SOP}}$ in the various cases. From the observation of these plots, it can be deduced that the shorter are the windows, the smaller is $error_{\text{SOP}}$. This aspect is quite obvious because during short time intervals the variations of the SOP are moderate, and consequently the standard deviation of $error_{\text{SOP}}$ is smaller in comparison with the cases with larger time windows. It can be noted also that increasing N_{ang}, $error_{\text{SOP}}$ decreases on average. This effect is related to the polarimetric technique here adopted, which provides more precise measurements with a greater number of rotations of the quarter-wave plate (N_{ang}). From considerations deriving from the statistical theory, we suppose that the histograms of $error_{\text{SOP}}$ calculated in the case of a single

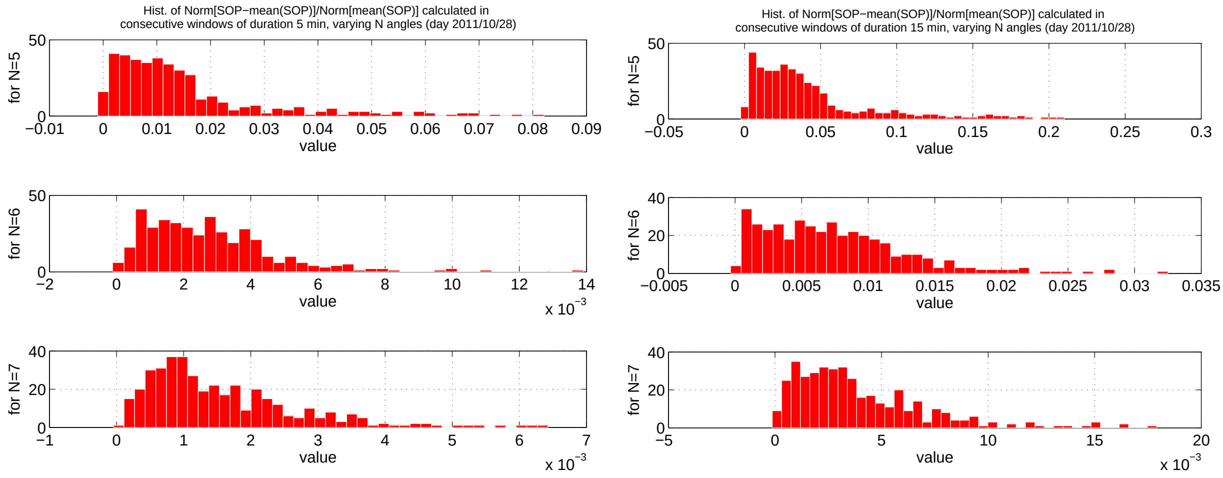

Hist. of Norm[SOP−mean(SOP)]/Norm[mean(SOP)] calculated in consecutive windows of duration 5 min, varying N angles (day 2011/10/28)

Hist. of Norm[SOP−mean(SOP)]/Norm[mean(SOP)] calculated in consecutive windows of duration 15 min, varying N angles (day 2011/10/28)

(a) 5-minutes analysis windows (b) 15-minutes analysis windows

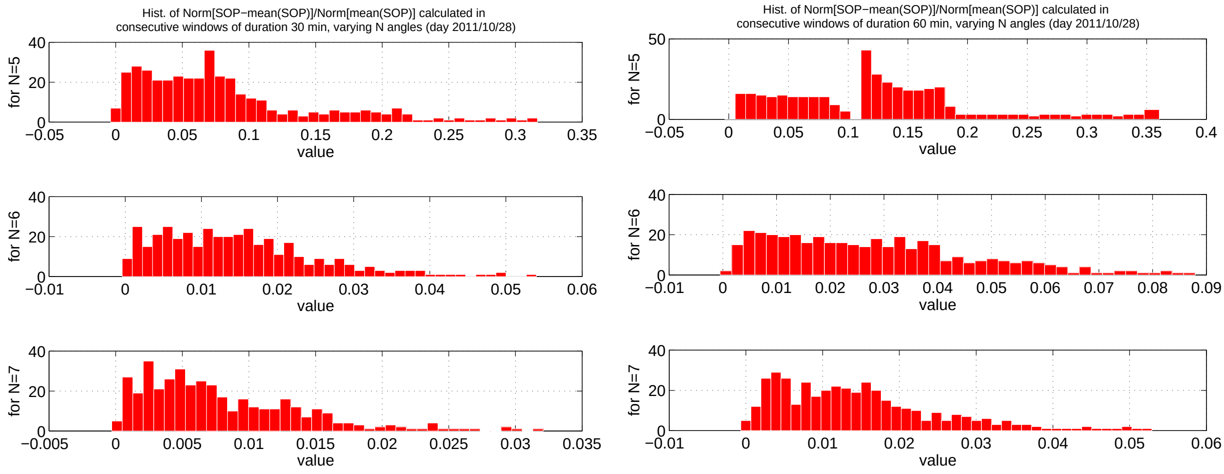

Hist. of Norm[SOP−mean(SOP)]/Norm[mean(SOP)] calculated in consecutive windows of duration 30 min, varying N angles (day 2011/10/28)

Hist. of Norm[SOP−mean(SOP)]/Norm[mean(SOP)] calculated in consecutive windows of duration 60 min, varying N angles (day 2011/10/28)

(c) 30-minutes analysis windows (d) 60-minutes analysis windows

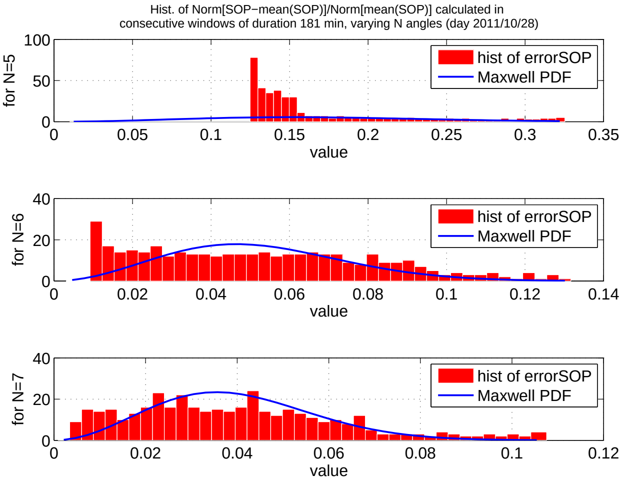

Hist. of Norm[SOP−mean(SOP)]/Norm[mean(SOP)] calculated in consecutive windows of duration 181 min, varying N angles (day 2011/10/28)

(e) 181-minutes analysis window

Figure 3.10: Histograms of $error_{\text{SOP}}$, with $N = N_{\text{ang}} = 5$, 6 or 7 and variable durations of the analysis time windows.

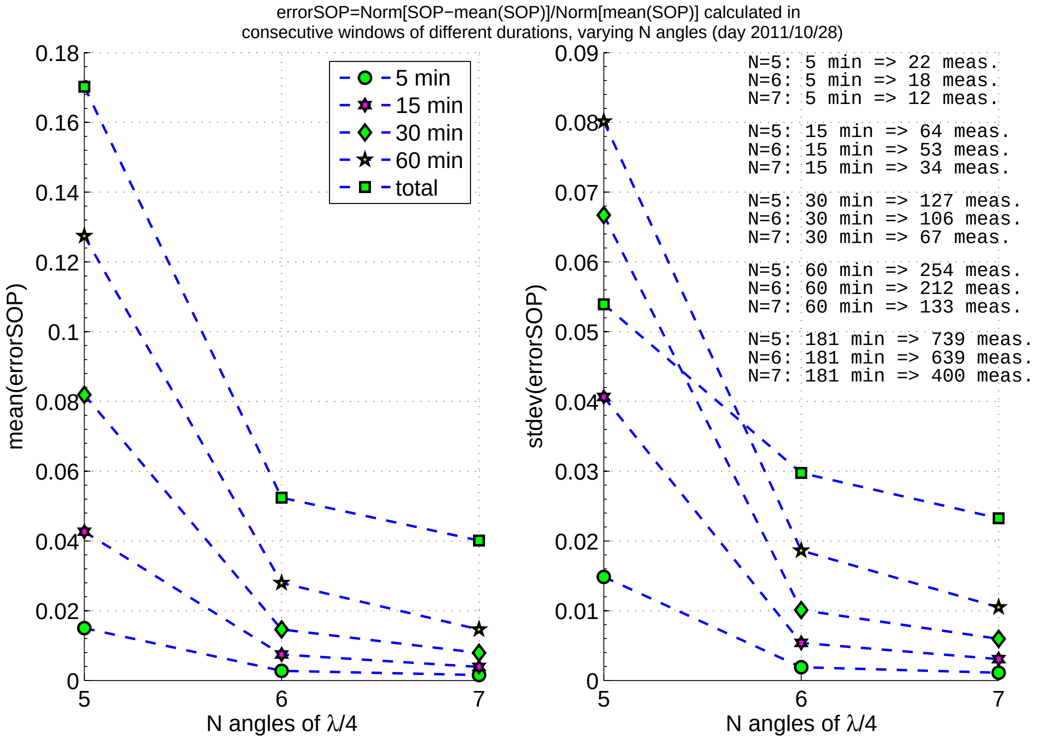

Figure 3.11: Mean and standard deviation of $error_{\text{SOP}}$, with $N = N_{\text{ang}} = 5$, 6 or 7 and variable durations of the analysis time windows (reported in the rectangle-box legend).

time window (of 181 minutes) is approximately Maxwellian, i.e. we assume that $error_{\text{SOP}}$ has a Maxwellian probability density function (PDF). Although this aspect is not studied in depth here, in Fig. 3.10(e) there is the superposition of the histograms and the theoretical PDF mentioned above. From this qualitative comparison it appears that $error_{\text{SOP}}$ has a Maxwellian distribution, at least in certain cases.

Actually, it is necessary to have another type of visualization of the statistical properties of $error_{\text{SOP}}$ in all the cases. More precisely, after having evaluated $error_{\text{SOP}}$ in each time window ($error_{\text{SOP},i}$) with variable N_{ang}, it is useful to calculate its mean and standard deviation; this means that after fixing the time duration of the windows and N_{ang}, we calculate the mean and standard deviations of the values (one for each window) of $error_{\text{SOP}}$. These quantities are represented in the plots of Fig. 3.11. It is clear that by increasing N_{ang} from 5 to 6 we obtain a significant improvement on $error_{\text{SOP}}$, whose mean and standard deviation are reduced by a factor of more than 2 (in most cases) with a slight increment of the measurement time. Otherwise, varying N_{ang} from 6 to 7 produces a large increment of the measurement time with an unimportant decrease of the mean and standard deviation of $error_{\text{SOP}}$. From such considerations it follows that the best compromise is obtained for $N_{\text{ang}} = 6$. This value will be used in the next experimental steps.

To conclude this section, we observe that from these calculations emerges that an analysis of the acquired data based on time windows could be very useful to compensate drift effects caused by phenomena externals to the systems. It can permit to separate the external drift effects from the internal ones, which must be characterized in detail to use the measurement system.

3.2 Measurements of SOP using Power Meter and OSA

The polarimetric system used before was constituted by a polarization controller and an optical power meter (Fig. 3.1), which enables accurate SOP and DOP measurements. But this configuration does not permit to acquire information about the spectral composition of the optical signal; this is due to the fact that the power meter can only measure the power distributed in a large wavelength range, typically $[800,\ 1650]$ nm. However, in other experimental steps it could be necessary to have a visualization and an accurate measure of the spectral composition of the signal in a small span centred around a certain wavelength (e.g., 1550 nm or 1640 nm). For example, in fact, in the experiments regarding the polarization-pulling effect based on Raman scattering (explained in Sec. 1.4), there is the necessity to analyse the optical spectrum to verify the presence of nonlinear effects. To meet this need an Optical Spectrum Analyzer (OSA) is employed. The chosen OSA is an *Anritsu MS9710B*. Some of the main specifications declared by the constructor of this instrument ([17]) are:

- Wavelength Range: 600 to 1750 nm;
- Wavelength Accuracy: ± 0.3 nm;
- Setting Resolution: 0.07, 0.1, 0.2, 0.5, 1 nm;
- Polarized Light Dependency: $\leq \pm 0.05$ dB (at 1550 nm).

Nevertheless, we have no information about the capacity of the OSA to provide a SOP measurement when it is part of a polarimetric system, or, more precisely, the accuracy of SOP measurements produced by this instrument is unknown. A way to solve this uncertainty is to employ a second instrument, which must be considered sufficiently precise, and use it as a reference for the measurements. Here the reference instrument for the measure of SOP is the optical power meter (PM) *ILX-FPM8210* already used; it is considered accurate because the polarimetric system employing it (Fig. 3.1) gives substantially the same results of the very precise polarimeter *Profile-PAT9000B*, as explained in 3.1. Consequently, the optical power at the output of the polarization controller (PC) is equally divided by a 50/50 power splitter, at whose two optical outputs are connected PM and OSA, respectively. It must be underlined that PM and OSA are theoretically insensitive to the polarization of the signal and, in fact, the variations of polarization after PC are not considered in the implemented polarimetric system. This new experimental setup is represented in Fig. 3.12.

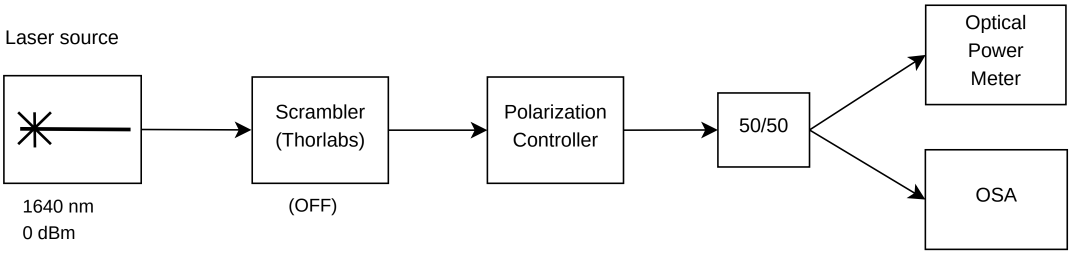

(a)

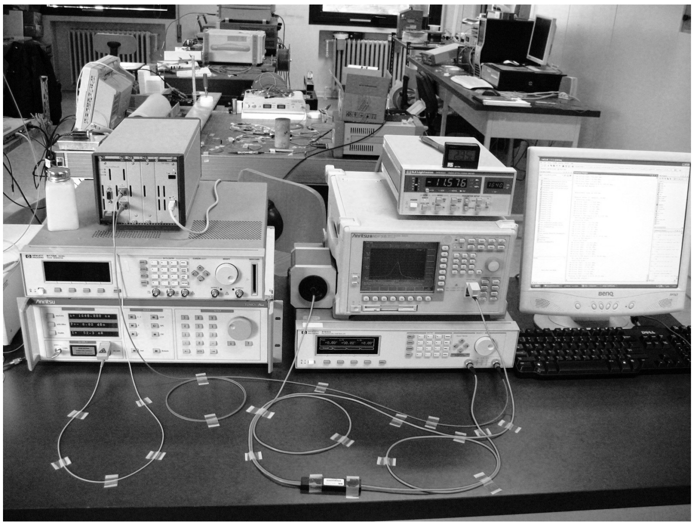

(b)

Figure 3.12: Schematic representation (a) and picture (b) of the second experimental configuration with laser source and the polarimetric system. The optical power is measured at the outputs of the power splitter by OSA and PM.

The laser source is an *Anritsu TUNICS-Plus*, the same used previously. The generated optical signal at 1640 nm propagates in a fiber and passes through a *Polarization Scrambler* (*Thorlabs TXP5004*). During this experimental step the scrambler is kept off and it is therefore totally equivalent to a typical fiber optic patch cord, which causes a negligible loss in optical power. We observe that the power losses introduced by the experimental devices are unimportant in a polarimetric system, provided that these losses do not vary during the measurements. The scrambler will be turned on in another experimental set (see Chapter 4). The signal hence arrives to the PC, which is the first device of the polarimetric system. As mentioned before, the optical power at the output of the PC is equally divided by a 50/50 power splitter and the power measurements are made in parallel by PM and OSA.

A key point for this experimental setup is the configuration of the instruments. For PM, its built-in display filter is sequentially set in three different modalities, for each of which power measurements are provided, as explained below. These modalities correspond to different display filter update rate, and are:

- "slow", corresponding to acquiring 100 samples during intervals of 5 s and providing the arithmetic mean of their values;
- "medium", corresponding to acquiring 10 samples during intervals of 0.5 s and providing the arithmetic mean of their values;
- "fast", corresponding to acquiring 1 sample during intervals of 0.05 s.

We can already observe that these modalities should be chosen depending on the rate of variations of the optical power (i.e., of the SOP). For OSA, we choose this configuration, which in case will be modified later:

- $\lambda_{\text{center}} = 1640$ nm;
- span: 2 nm;
- 51 wavelength-points (uniformly distributed) in the span;
- 1000 power acquisitions for each wavelength-point, and an average of them;
- resolution: 0.07 nm;
- Video-BandWidth: VBW = 10 Hz.

This means that the OSA acquires optical power in 51 points with a distance of $2/(51-1) = 0.04$ nm from each other, in the range from 1639 nm to 1641 nm. For each of this wavelength-points, the instrument makes 1000 power measurements of the signal in rapid succession, and provides the arithmetic mean of these power values. It must be observed that only the value of the optical power at 1640 nm is necessary to measure the SOP and the DOP of the signal, which is centred at 1640 nm. In fact, when we analyse the data acquired by OSA to evaluate the SOP, we consider only the wavelength-point to which corresponds the maximum power; this wavelength-point should be in the mid of the 51 points of the acquisition, i.e. the 25th or 26th point, taking into account the chosen resolution. Hence a wavelength span of 2 nm seems unnecessarily large for the measurements of SOP performed here. Despite all this, we set the span to 2 nm because during other experimental steps it will be necessary to estimate the *Amplified Spontaneous Emission* (ASE) at the receiver, whose evaluation requires to acquire the optical spectrum in a sufficiently large span around $\lambda_{\text{center}} = 1640$ nm. It is therefore important to use this value for the span and adapt to this choice, since this set of experiments is propaedeutic to others. Anyway, the chosen number (1000) of power acquisitions for each wavelength-point is the maximum for this instrument, and consequently it allows the best averaging and hence a more accurate power measurement for each point in the span. On the other hand, choosing the minimum number of wavelength-points (51) in the span speeds up power acquisitions.

3.2.1 Preliminary test of measurements with OSA

The configuration described above must be initially tested to verify that there are not large mismatches between measurements provides by PM and OSA. This is not a quantitative test, which will be followed by an accurate comparison of the measurements provided by the two instruments, discussed in 3.2.2.

The test consists in measuring SOP using OSA and, in succession, PM in the three different modalities of display filter update rate. In detail, remembering that a polarization measurement requires 6 successive power acquisition (with $N_{\text{ang}} = 6$), we start a measurement with OSA (lasting 110 s) and when it is finished we start a measurement with PM in "slow" modality (lasting $6 \cdot 5 = 30$ s). After this, a measurement in "medium" modality and one in "fast" modality are executed in succession. More precisely, to reduce the total duration of the test, we start contemporaneously the OSA and the first PM measurements and we make sure that they terminate at the same time inserting appropriate breaks between the 6 power acquisitions by PM (one for each angle of rotation of the quarter-wave plate of the PC). With this solution we save 30 s for each set of four SOP measurements, which are obtained in 120 s. We repeat all this for 63 times, for a total duration of 126 minutes. However, it must be observed that each of the four measurements refers to different instants, in the time between which there can be variations of the state of polarization. Furthermore, with this measuring mode, we have no precise information about the possible SOP variations during the 110 s required by OSA for the 6 successive acquisitions of the optical spectrum in the span. This aspect will be treated experimentally in 3.2.2.

The values of the SOP measured with OSA and PM in "slow" modality are represented in Fig. 3.13. The other two PM modalities provide values nearly identical to those represented for

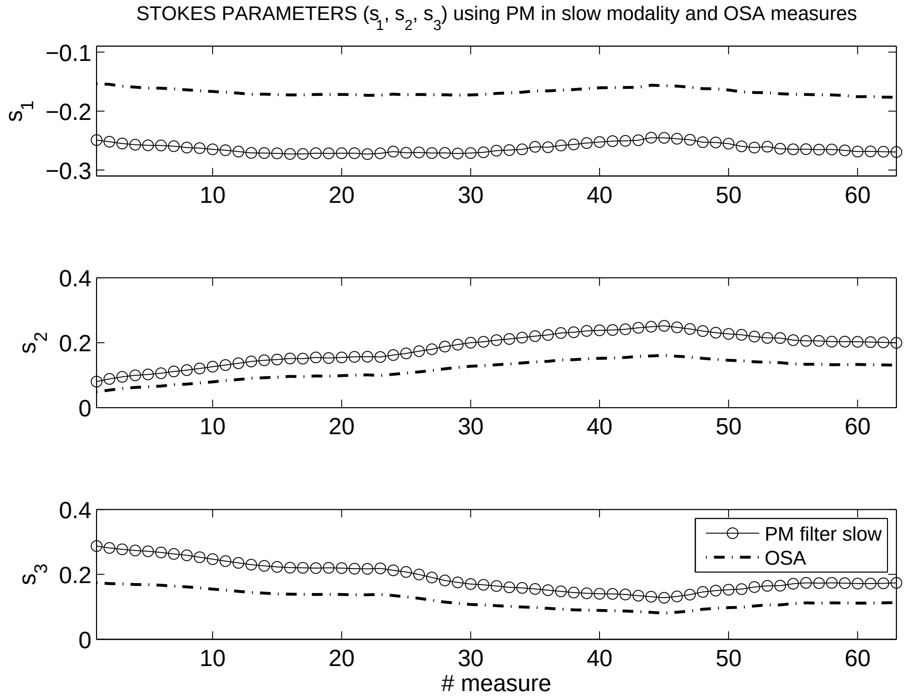

Figure 3.13: SOP measured with OSA and with PM in "slow" modality of the display filter.

PM. Having measured SOP, we can also obtain DOP measurements by analytical calculations. DOPs values are visualized in Fig. 3.14. Two considerations can be made from the observation of these plots. First of all, SOP and DOP are not constant during the test even if the laser source emits a signal with constant polarization. This is probably due to the fact that the system temperature varies causing a drift on SOP, already observed in the previous experimental steps. There could be other causes of this phenomenon, such as not-well defined fluctuations of the behaviour of devices and instrumentation. The second consideration is the fact that the curves of SOP and DOP measured with OSA are very similar to those measured with PM, except for a variable shift. This suggests that the chosen configuration does not causes blunders. However, the measurement method should be suitably modified to obtain information about the possible variations of the polarization during a measurement with OSA.

3.2.2 Variations of SOP during a measurement with OSA

A measurement of SOP executed by the chosen OSA inserted in our polarimetric system lasts more than 110 s, which could be a too much long time interval to measure a state of polarization. This creates the need to have information about the potential variations of the polarization during a measurement with OSA, as mentioned before. This need must be satisfied even if this causes an increment of measurement time itself or other perturbations.

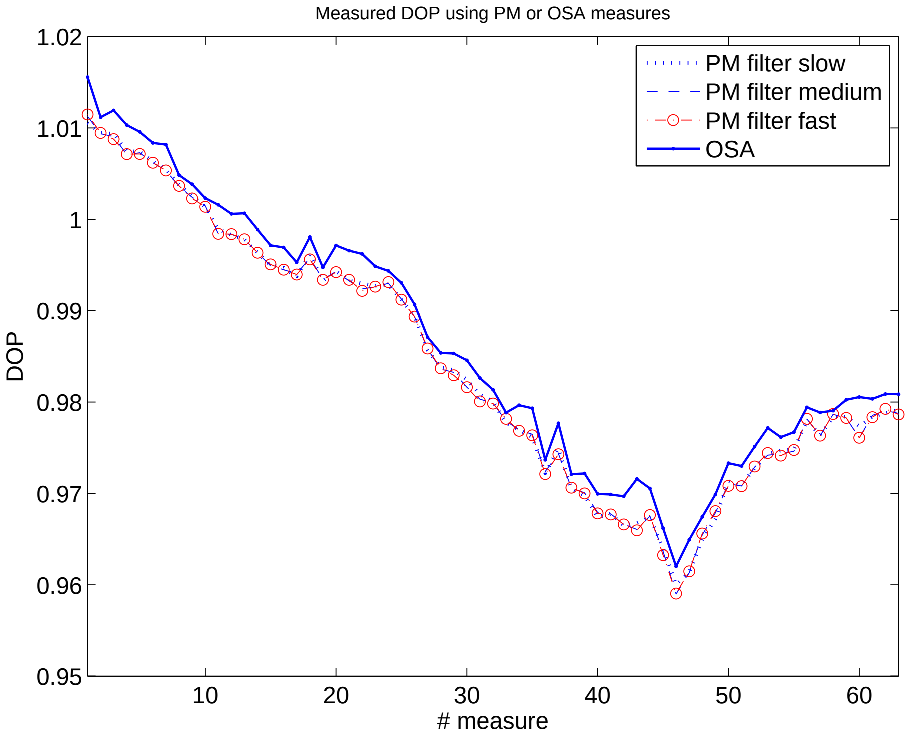

Figure 3.14: DOP measured with OSA and with PM in three different modalities of display filter update rate. Observe that the three PM curves are superimposed.

The experimental setup and configuration are the same, already used and described at the beginning of this section (3.2). Regarding measurement method, in particular, six measurements of optical power are made with OSA, one for each angle of rotation ($N_{\text{ang}} = 6$) of the quarter-wave plate of the polarization controller, thus obtaining one measurement of SOP. Between an acquisition of optical power in the 2 nm-span by OSA and the next, a complete measurement of SOP is executed by PM in “fast” modality. The “fast” modality is chosen here because we have already proved that the results it gives are sufficiently similar to those of other modalities and obviously because it is faster in its execution. Consequently, during a measurements of SOP by OSA we obtain six values of SOP by PM, equally distributed in time. This is achieved through an appropriate scheduling, which is managed by MATLAB® software installed in the computer that controls the instrumentation by GPIB, as already done in all the previous experimental steps.

In this way it is estimated how much SOP and DOP vary during the execution of a measurement with OSA, which would take about 120 s if PM was not running. Moreover, if the values obtained with OSA are very close to those obtained with PM, a confirm of the accuracy of OSA measurements will be obtained, at least in these experimental conditions and except for measurement uncertainties.

The test lasts 256 minutes, equivalent to 109 measurements of SOP. Hence, a single measurement taken with OSA, during which PM operates as explained above, lasts 140 s.

In Fig. 3.15 there is the representation of the PM and OSA measurements of the Stokes' vector components as functions of time. Fig. 3.16 contains a magnification of the previous plot on the temporal axis which emphasizes the fact that a single OSA measurement corresponds to several PM measurements in this particular test. Moreover, in Fig. 3.17 there is the visualization of the difference between the values provided by the two instruments, in all the three components of the Stokes' vector. From the observation of these plots it can be only noted that the trends of the measurements deriving from the two instruments are very similar with apparently low point by point differences. Consequently we calculate the percentage relative deviation between the two measured Stokes' vectors, defined as $\left|\left(s_i^{(\text{PM})}(t) - s_i^{(\text{OSA})}(t)\right)/s_i^{(\text{PM})}(t)\right| \times 100$ with $i = 1, 2, 3$, and represent this interesting vector in Fig. 3.18. It is evident that there are instants in which the gap between the values is relatively high, probably due to fast variations of SOP to which PM is sensitive but OSA is not because of its low speed of measurement. Regarding the third component of the Stokes' vector s_3, we observe that the percentage deviation between the two measured values is extremely high during an interval around the middle of the test; the reason of this phenomenon is that s_3 is nearly zero in that interval and hence the percentage variation is not very significant therein. Nevertheless, the percentage deviation between the two measurements is most often lower than 10%, which is another confirmation of the measurement accuracy of the OSA. In section 3.2.3 uncertainties on measured SOPs and DOPs are calculated enabling to determine whether these measurements are really reliable.

It is worthwhile to analyze also the Stokes' unit vector (or versor), i.e. the Stokes' vector normalized to its norm; this norm corresponds to the total power s_0. In this way, the point de-

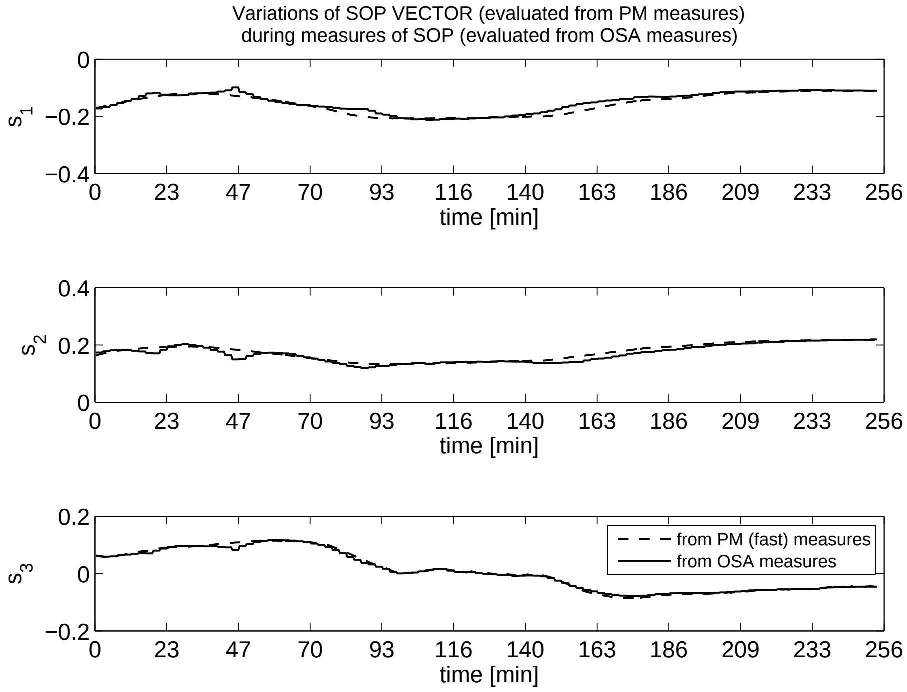

Figure 3.15: Stokes' vector components measured from PM and OSA power measurements during the test. A measurement provided by OSA corresponds to 6 PM measurements in this test.

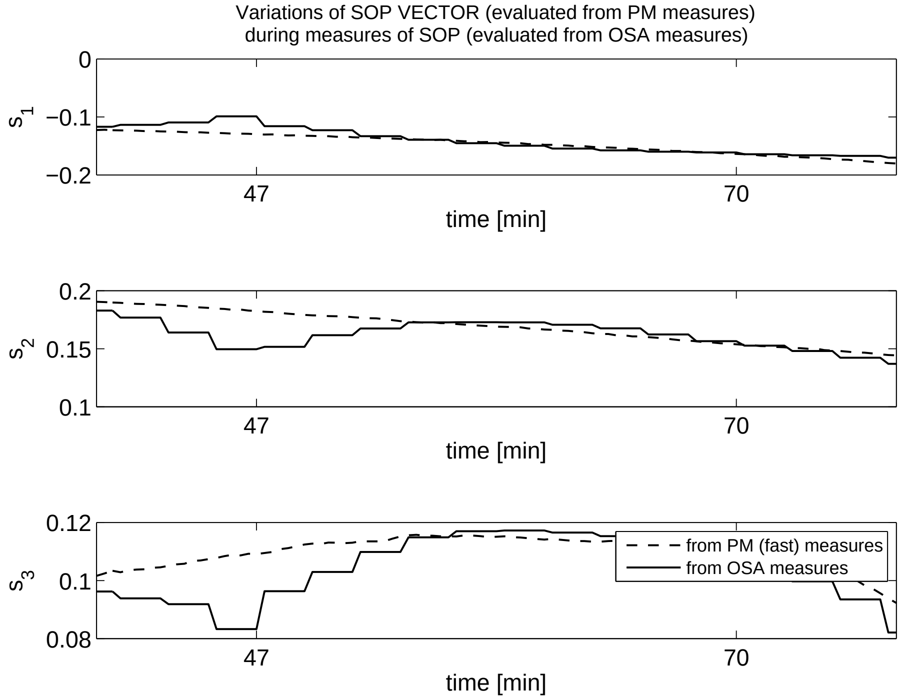

Figure 3.16: Magnifications on the time-axis of the plots contained in Fig. 3.15.

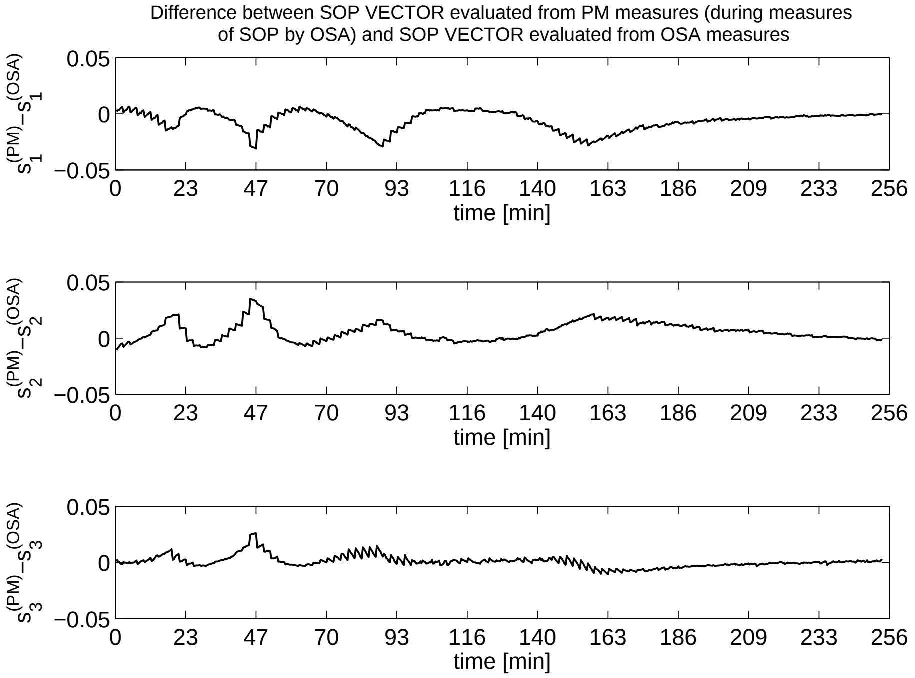

Figure 3.17: Difference between Stokes' vector measured with PM and Stokes' vector measured with OSA, as a function of time during the test.

scribing the polarization lies on the surface of the Poincaré sphere with radius 1, and this displays the state of polarization of the *polarized part of the laser beam*. Figg. 3.19 and 3.20 visualize the components of the Stokes' versor measured during the test and a magnification on the temporal axis of them, respectively. In Fig. 3.21 there is the representation of the vectorial difference between the two measured Stokes' unit vectors as a time function. From the observation of these plots it is clear that the two instruments provide measurements of the polarized part substantially coincident. In fact, representing the percentage relative deviation between the two measured Stokes' versors (defined as above) in Fig. 3.22, it is deduced that the relative deviation between the components of the two unit vectors is almost always lower than 3%, except for particular instants. This observation proves that the used OSA enables accurate polarization measurements of the polarized component of the signal.

After having measured SOP by evaluating Stokes' vectors, it is important to measure and analyse the degree of polarization. The evolution of DOP during the test, measured using our polarimetric technique and both the instruments configured as explained above, is reported in Fig. 3.23. Fig. 3.24 contains a magnification on the temporal axis of the plot of Fig. 3.23. It can be observed that DOP is relatively high, typically great than 0.95, as it must be, since the laser source is polarized. Another observation is that DOP is not constant, for the same reasons explained for the previous experimental steps, in which it has been observed the same phenomenon. The fact to emphasize is that the trend of the DOP measured with OSA follows

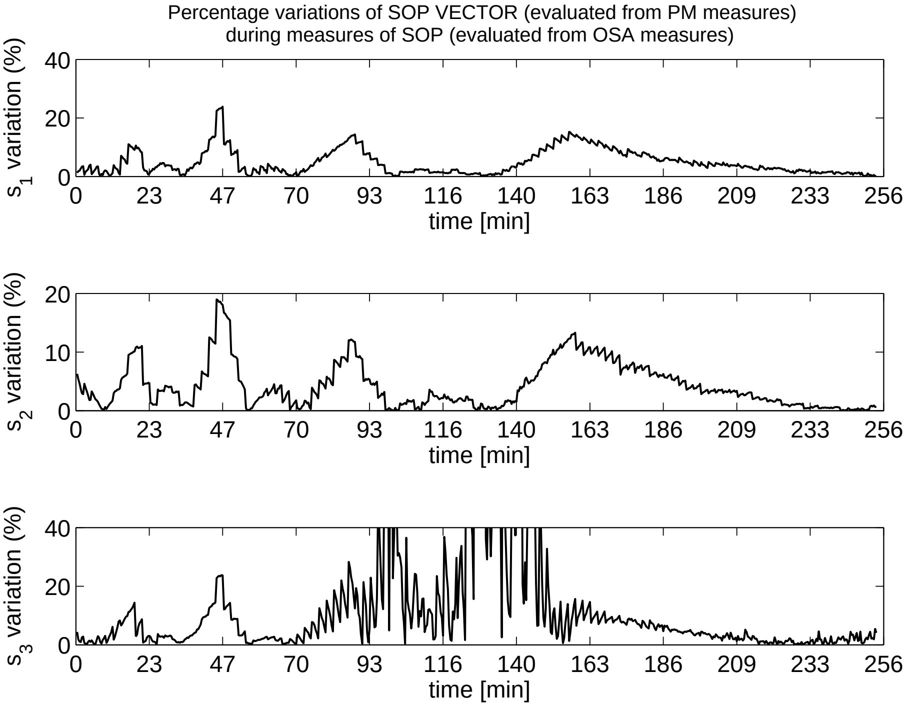

Figure 3.18: Percentage deviation of Stokes' vector measured with OSA from the same vector measured with PM, as a function of time. The deviation is obtained by normalizing the difference of the components to the component measured with PM, at the same instant.

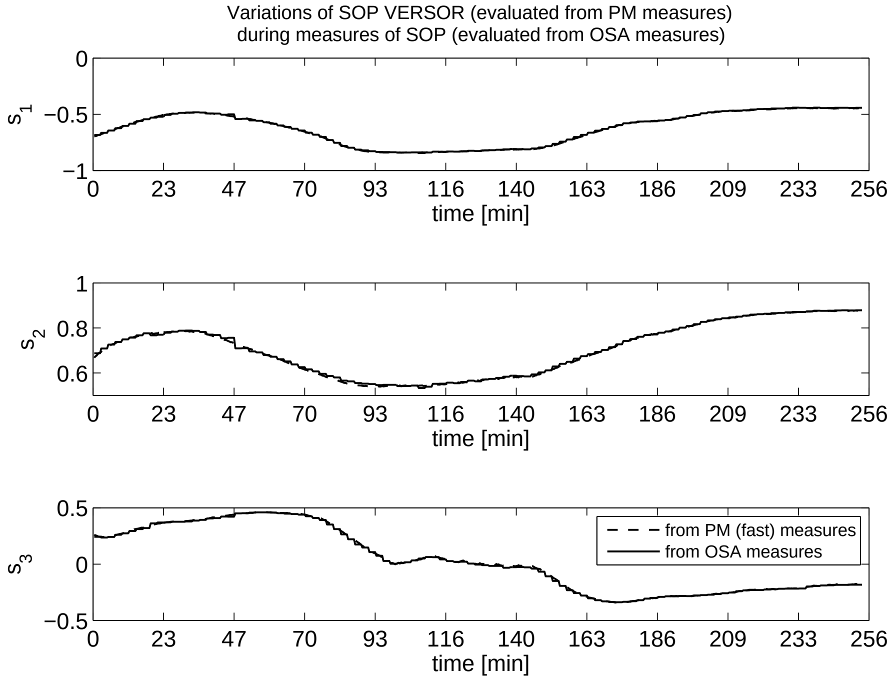

Figure 3.19: Stokes' unit vector components measured from PM and OSA power measurements during the test. A measurement provided by OSA corresponds to 6 PM measurements in this test.

the trend deriving from PM measuring, in the sense that the deviation between the two curves appears to be sufficiently limited. The lower acquisition rate of OSA is the main cause of local differences between the two DOP curves. The absolute difference between the DOP values measured with the two instruments, averaged on all measurements, is 0.0031.

To get more information, the percentage deviation between the two DOP is plotted (Fig. 3.25), having defined it as the difference between the two DOP evolutions normalized to the DOP evaluated from PM at the same instant. This percentage deviation is quite variable, as expected, but it is always lower than 2.5% and almost everywhere lower than 1%. The fact that the mean of the DOP percentage deviation is 0.5% proves that DOP measurements deriving from OSA power detections are always close to those measured with PM. Consequently, we consider DOP values provided by OSA reliable. It must be remarked that it is necessary to evaluate the uncertainties of these measurements to quantify this reliability. Sec. 3.2.3 deals with this aspect.

3.2.3 Measurements uncertainties

We want to evaluate the uncertainties of the measurements provided by the polarimetric system; in particular, the focus is on the DOP measurements obtained with OSA. In fact, the polarimeter schematized in Fig. 3.12(a) could be used without the power meter in other experiments, because

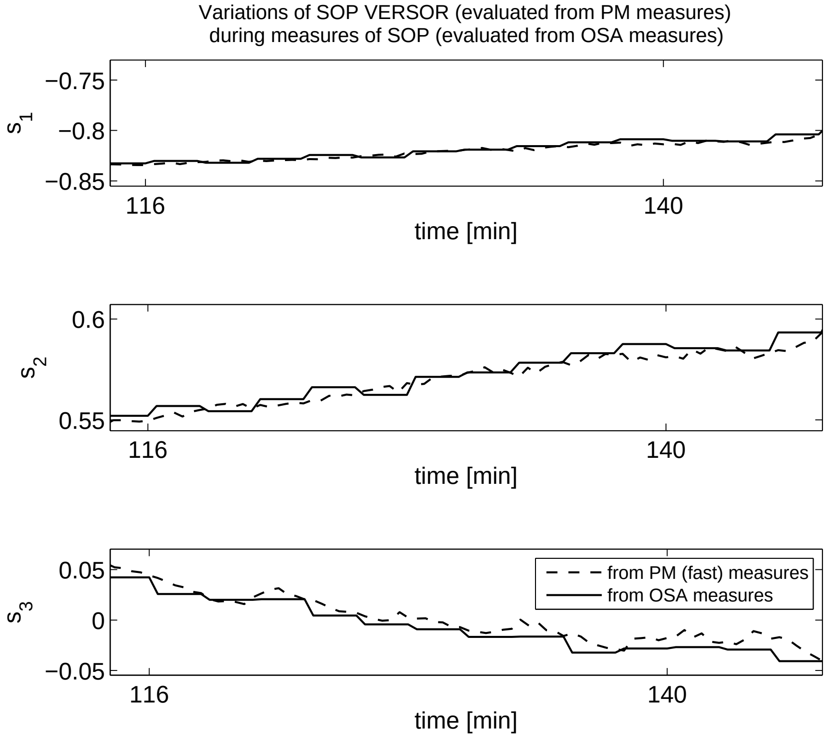

Figure 3.20: Magnifications on the time-axis of the plots contained in Fig. 3.19.

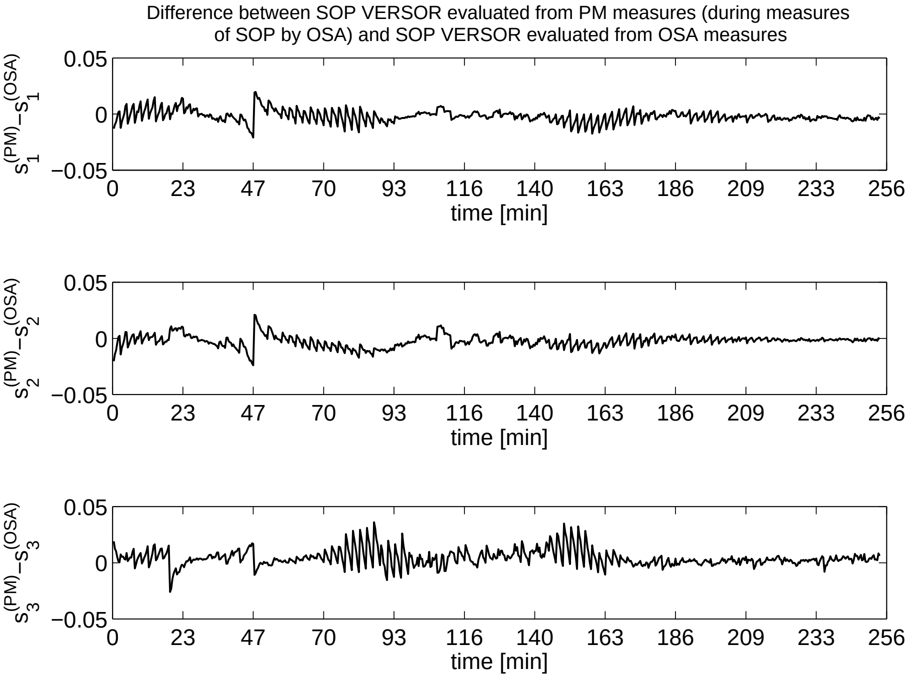

Figure 3.21: Difference between Stokes' unit vector measured with PM and Stokes' unit vector measured with OSA, as a function of time during the test.

only the OSA gives information about the spectrum of the signal. As explained before, in this set of experiments the PM is used as a reference to characterize the polarization measurements obtained using the spectrum analyzer.

The evaluation of the uncertainties is a complex and interesting issue, which can be resolved using different approaches. The first approach followed here is characterized by the propagation of the uncertainties. If C_1, C_2, C_3 are variables with *standard uncertainties* u_1, u_2, u_3, respectively, the theory of propagation of uncertainty gives these expressions for the standard deviations $u(\cdot)$ of the following functions of variables:

$$u(C_1^2) = 2\sqrt{C_1^2 u_1^2} \tag{3.2}$$

$$u\left(\sqrt{C_1^2 + C_2^2 + C_3^2}\right) = \sqrt{(C_1^2 + C_2^2 + C_3^2)^{-1}\,(C_1^2 u_1^2 + C_2^2 u_2^2 + C_3^2 u_3^2)} \tag{3.3}$$

$$u(C_1/C_2) = \sqrt{\frac{1}{C_2^2}\,u_1^2 + \frac{C_1^2}{C_2^4}\,u_2^2}\;. \tag{3.4}$$

Consequently, having defined the degree of polarization as

$$\mathrm{DOP} = \frac{\sqrt{S_1^2 + S_2^2 + S_3^2}}{S_0} \tag{3.5}$$

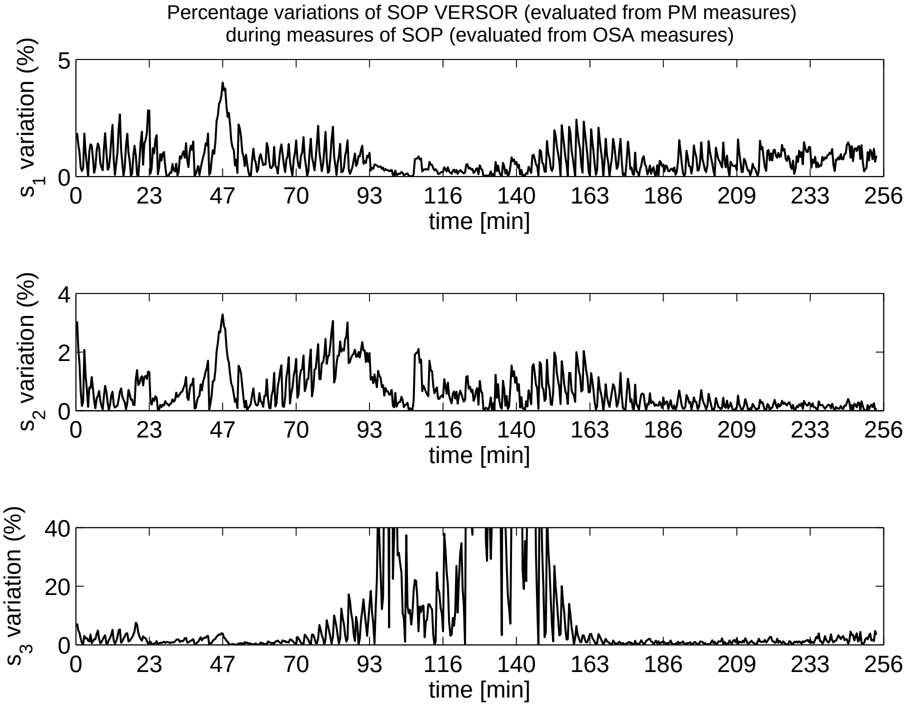

Figure 3.22: Percentage deviation of Stokes' unit vector measured with OSA from the same vector measured with PM, as a function of time. The deviation is obtained by normalizing the difference of the components to the component measured with PM, at the same instant.

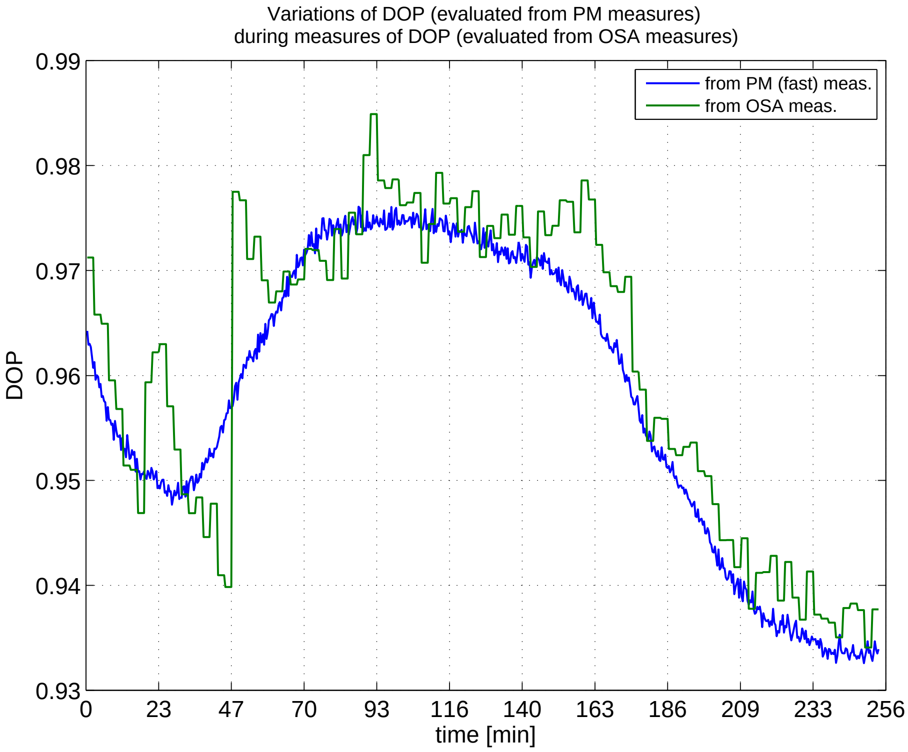

Figure 3.23: DOP measured using PM and OSA. A measurement provided by OSA corresponds to 6 PM measurements in this test.

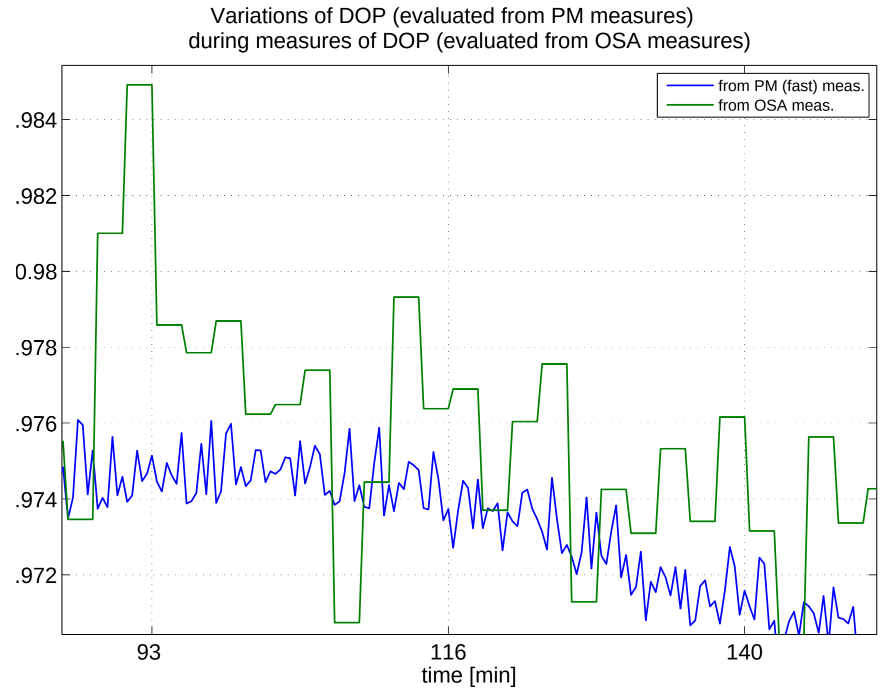

Figure 3.24: Magnifications on the time-axis of the plots contained in Fig. 3.23.

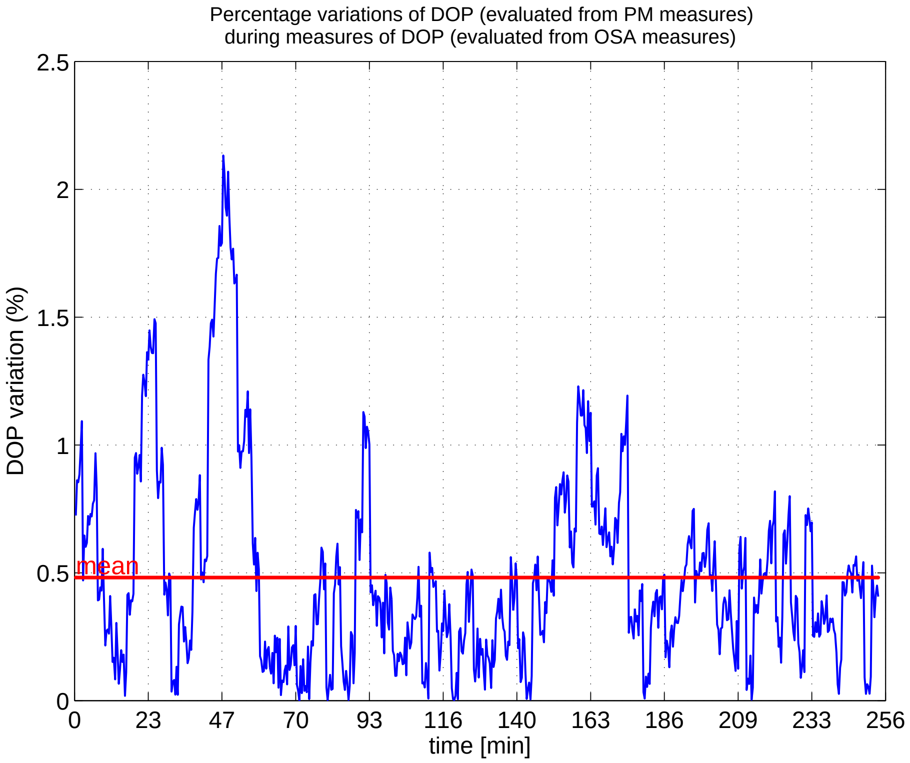

Figure 3.25: Percent. deviat. of DOP measured with OSA from DOP measured with PM as a time function.

we found that its standard uncertainty is

$$u(\text{DOP}) = \sqrt{\frac{1}{S_0^2}\,\frac{S_1^2 u_{S_1}^2 + S_2^2 u_{S_2}^2 + S_3^2 u_{S_3}^2}{S_1^2 + S_2^2 + S_3^2} + \frac{S_1^2 + S_2^2 + S_3^2}{S_0^4}\, u_{S_0}^2} \tag{3.6}$$

where u_{S_i} is the uncertainty in the measurement of the i-th Stokes' parameter. This expression requires the knowledge of the uncertainties of the measured values of the Stokes' vector components, which are still unknown. It is therefore convenient to consider a different approach, based on the statistic of the already measured values.

Regarding the SOP, we define this vector

$$\bar{S}\,'^{(\text{OSA})} = \frac{S_0^{(\text{PM})}}{S_0^{(\text{OSA})}}\,\bar{S}^{(\text{OSA})} \tag{3.7}$$

and this quantity

$$\Delta'_{\text{SOP}} = \text{norm}\left(\bar{S}\,'^{(\text{OSA})} - \bar{S}\,^{(\text{PM})}\right) \ . \tag{3.8}$$

Defining $< \Delta'_{\text{SOP}} >$ the arithmetic mean of all the N values of Δ'_{SOP} in a set of N measurements, we suppose that $< \Delta'_{\text{SOP}} >= 0$. In fact, considering the set of measurements represented in Figg. 3.13 and 3.14, and already analyzed, results that $< \Delta'_{\text{SOP}} > \sim 10^{-4}$. This proves that the measurements of the polarized part of the signal obtained with OSA are substantially identical to those obtained with PM.

To continue the analysis, a simplification is necessary. To evaluate the uncertainties of the DOP values obtained with OSA, we assume that the PM measurements, which are used as a reference, have uncertainties equal to zero. This is an acceptable assumption, which could be eventually changed if there is the necessity of a more rigorous analysis. Defining the scalar quantity with sign

$$\delta_{\text{DOP}} = \text{DOP}_{\text{OSA}} - \text{DOP}_{\text{PM}} \ , \tag{3.9}$$

it is important to focus on its arithmetic mean $< \delta_{\text{DOP}} >$, which is calculated averaging all the DOP measurements made in an experimental set. The scalar $< \delta_{\text{DOP}} >$ can be interpreted as a systematic error of DOP measurements committed using OSA. We can also define its standard deviation as

$$\sigma_{\delta_{\text{DOP}}} =< (\delta_{\text{DOP}} - < \delta_{\text{DOP}} >)^2 > \tag{3.10}$$

where the symbols $< \cdot >$ mean that the quantity is calculated as the arithmetic mean of all the values in the experimental set, as above. The quantity $\sigma_{\delta_{\text{DOP}}}$ can be considered as a random error committed in DOP measuring.

We decide to use the following expression to quantify the uncertainty of the DOP measurements obtained with OSA:

$$\varepsilon_{\text{DOP}} = |< \delta_{\text{DOP}} >| + \sigma_{\delta_{\text{DOP}}} + \xi \ , \tag{3.11}$$

where ξ indicates a corrective term which takes into account other uncertainty's factors. For example, ξ can include the uncertainties caused by temperature drift phenomena and, especially, by the power meter, which inevitably introduces errors, although it is used as a reference in our tests. The Eq. (3.11) refers to a worst-case/precautionary approach, i.e. the value assigned to the uncertainty is maximum.

We consider the same set of measurements represented in Figg. 3.13 and 3.14, analyzed in Sec. 3.2.1, in which the measuring method is standard. From calculations, results that $< \delta_{\text{DOP}} > \simeq 3 \cdot 10^{-3}$ and $\sigma_{\delta_{\text{DOP}}} \simeq 8 \cdot 10^{-4}$. A reasonable choice is therefore: $\varepsilon_{\text{DOP}} = 1 \cdot 10^{-2}$. This is the precautionary value we assign to the absolute uncertainty of DOP measurements deriving from OSA power acquisitions.

An observation is that using the measurements of PM in "slow" modality and "fast" modality, substantially the same value for $< \delta_{\text{DOP}} >$ is obtained, and the same for $\sigma_{\delta_{\text{DOP}}}$.

To conclude this analysis, it is important to verify that the results obtained when we have studied the variations of SOP during a measurement with OSA (Sec. 3.2.2) are compatible with the results of the evaluation of uncertainties. Referring to DOP measurements of Fig. 3.23, it has already been calculated that the absolute difference between the DOP values measured with the two instruments, averaged on all measurements, is 0.0031. We have also noted that the percent deviation between the two DOP curves (which are close to 1) is almost always lower than 1%. Moreover, although this difference is an averaged value, it is lower than the uncertainty value of 0.01. This proves that our uncertainty analysis is compatible with the experimental results. More precisely, the absolute difference between the two curves is nearly always lower than the uncertainty. We conclude that DOP measurements obtained with OSA are sufficiently accurate, in the sense that their measuring error is lower than the uncertainty assigned to them, on average.

Chapter 4

The polarimetric system with a polarization scrambled input signal

After having tested and characterized the polarimetric systems with a polarized optical signal at the input (Chapter 3), we want to use the same polarimeter to measure the polarization of a scrambled input signal. SOPs and DOPs are measured with the same polarimetric technique explained in Sec. 2.1. In particular, we use both optical power meter and optical spectrum analyzer to measure optical power, which is necessary to evaluate SOP and DOP with the chosen polarimetric technique.

The main features of the employed scrambler are listed, in particular its scrambling modes are described. Some preliminary experimental tests of these scrambling modes are performed and the corresponding measured DOPs are reported. Different sets of systematic tests of the scrambling modes, in which some scrambling parameters are varied, are also presented. From the measurements obtained in these tests, some remarks about the quality of the scrambling and about the capability of the OSA to measure the DOP of a scrambled beam are provided.

4.1 Experimental setup

The experimental setup is constituted by the same devices, described and used in the previous experiments. They are the laser source Anritsu TUNICS-plus, the polarization controller HP8169A, an optical power divider, the power meter ILX-Lightwave FPM-8210, the optical spectrum analyzer Anritsu MS9710B, some fiber optic patch cords and a polarization scrambler. The setup is represented schematically in Fig. 4.1(a). The configuration of the instruments is the same as before, with eventual variations to suit the type of measurements to be performed. However, how the instruments are set up is explained later, when measuring method will be presented.

To make scrambled the polarization of the signal, a SOP scrambler *Thorlabs TXP5004-DPC5500* is employed. More precisely, this device is a *Deterministic Polarization Controller*,

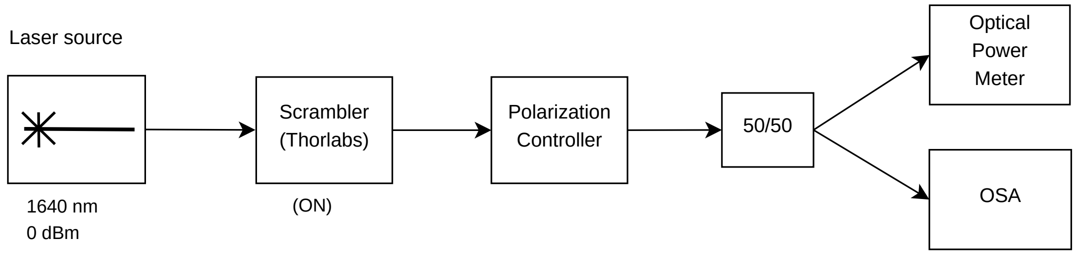

(a)

(b)

Figure 4.1: Schematic representation (a) of the experimental configuration with laser source, the polarimetric system and the scrambler Thorlabs. The optical power is measured at the outputs of the power splitter by OSA and PM. Picture (b) of the scrambler Thorlabs.

and it is controlled by software installed on a computer. It is depicted in Fig. 4.1(b). As one of the aims of this experimental step is to characterize this new device, it is useful and interesting to consider the features declared by its constructor ([19]), which are listed here for the sake of convenience:

- well defined polarization variations;
- uniform coverage of SOPs within a well defined grid on the Poincaré sphere within a preset time frame;
- depolarization of polarized light sources to a well defined DOP;
- event-triggered randomized SOP;
- 6 scrambling modes.

The constructor declares also that to adjust to the requirements of high or low speed applications like PDL measurements and depolarization this SOP Scrambler offers six modes of operation ([19]), three of which are considered here:

- “Deterministic Randomizer”: generates an ideal random distribution of successive SOPs and guaranties a complete coverage of the Poincaré sphere with a uniform distribution. Feedback from the internal inline polarimeter is used to place every calculated target SOP with high precision;
- “Deterministic SOP Scanner”: this mode periodically generates a grid of equally distributed SOPs on the Poincaré sphere and guarantees a complete and uniformly distributed coverage. Feedback from the internal inline polarimeter is used to place every calculated target SOP with high precision;
- “Fast Deterministic SOP Scanner”: this mode is faster but less accurate than deterministic mode. Feedback from the internal inline polarimeter is used only to control the start point of the SOP trajectory.

These scrambling modalities will be tested in the next experimental steps. In particular, some different parameters of the scrambling modalities will be tested and, in correspondence to them, the settings of PM and OSA will be chosen to measure properly SOP and DOP.

4.2 Preliminary tests of the scrambler

It is necessary to perform some preliminary tests to gather information on the chosen scrambling modalities using our polarimeter. All the three filtering modalities of the power meter (PM) are considered, as already done (Chapter 3): “slow”, “medium” and “fast”. The configuration of the OSA is the same:

- $\lambda_{\text{center}} = 1640$ nm;
- span: 2 nm;
- 51 wavelength-points (uniformly distributed) in the span;
- 1000 power acquisitions for each wavelength-point, and an average of them;
- resolution: 0.07 nm;
- Video-BandWidth: VBW = 10 Hz.

Regarding the measuring method, the timing of the four power acquisitions (three from PM, one from OSA) is such that the total time of measurement is minimized. In detail, the power acquistion with PM in "slow" modality is initiated, then a complete acquistion in the 2 nm-span is made with OSA, and when this is complete the PM is stopped. Just after this, the same measurement is performed with PM in "medium" and then "fast" modality. We remark that the power meter in "slow" filtering modality requires 5 s to complete correctly its very averaged measurement. To measure SOP, all this is repeated six times ($N_{\text{ang}} = 6$), one for each angle of rotation of the quarter-wave plate of the polarization controller.

In the next steps the three scrambling modes are tested for the first time.

4.2.1 "Deterministic Randomizer" scrambling mode

The scrambler is configured as follows:

- SOP grid: 20 deg;
- control period: 150 μs;
- control steps per SOP: 5.

The test consists of 70 successive measurements of SOP and DOP by the polarimeter with the chosen scheduling of the acquisitions. In Fig. 4.2(a) there is the evolution of the Stokes' parameters measured by PM in "slow" filtering during the test. The corresponding Poincaré sphere is represented in Fig. 4.2(b). We note that measured Stokes' parameters have mean values close to zero and large standard deviations, as it must be to have a good coverage of the sphere. The curves representing DOP measured by PM and OSA are plotted in Fig. 4.3. In Tab. 4.1 there are the mean values of DOP in this test, in all the instrumental cases.

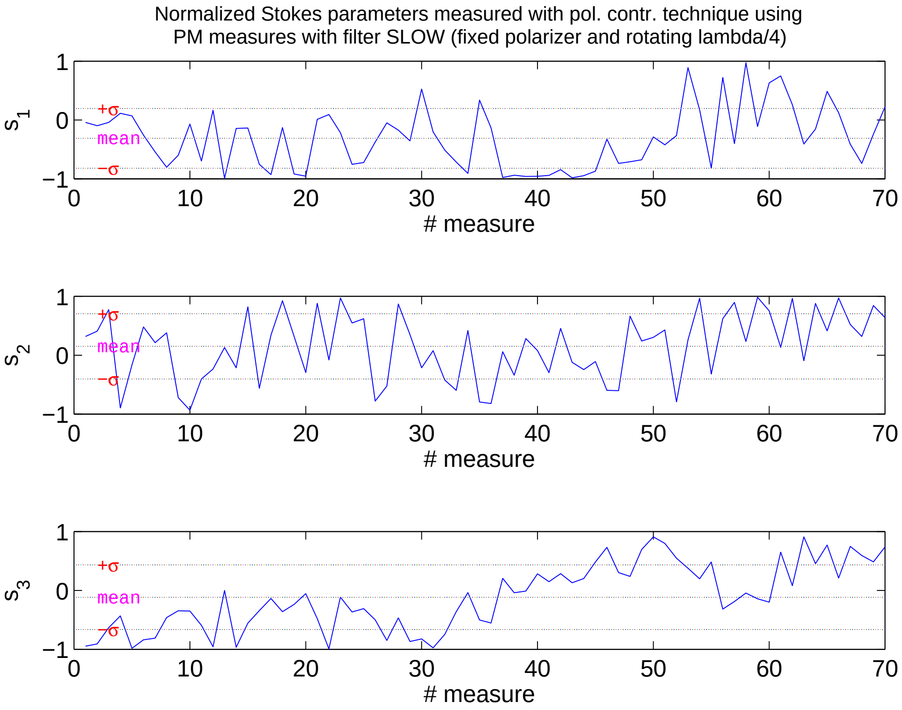

(a)

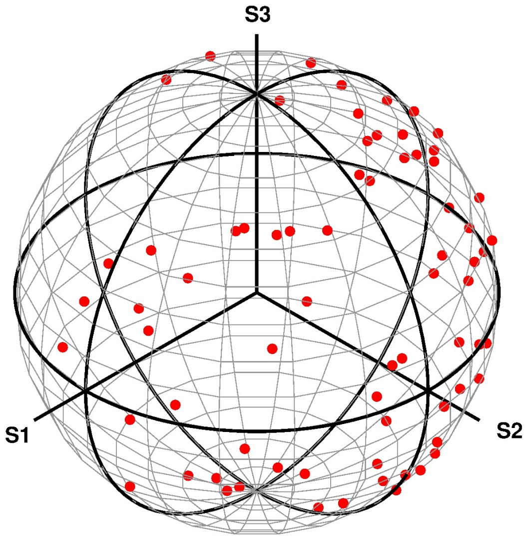

(b)

Figure 4.2: Stokes' parameters (a) and corresponding Poincaré sphere (b) measured in the test by PM in "slow" filtering modality. The scrambler is set in "Deterministic Randomizer" mode.

	PM “slow” mod.	PM “medium” mod.	PM “fast” mod.	OSA
mean of DOP	0.0091	0.0181	0.0563	0.0335

Table 4.1: Mean values of DOP in the test.

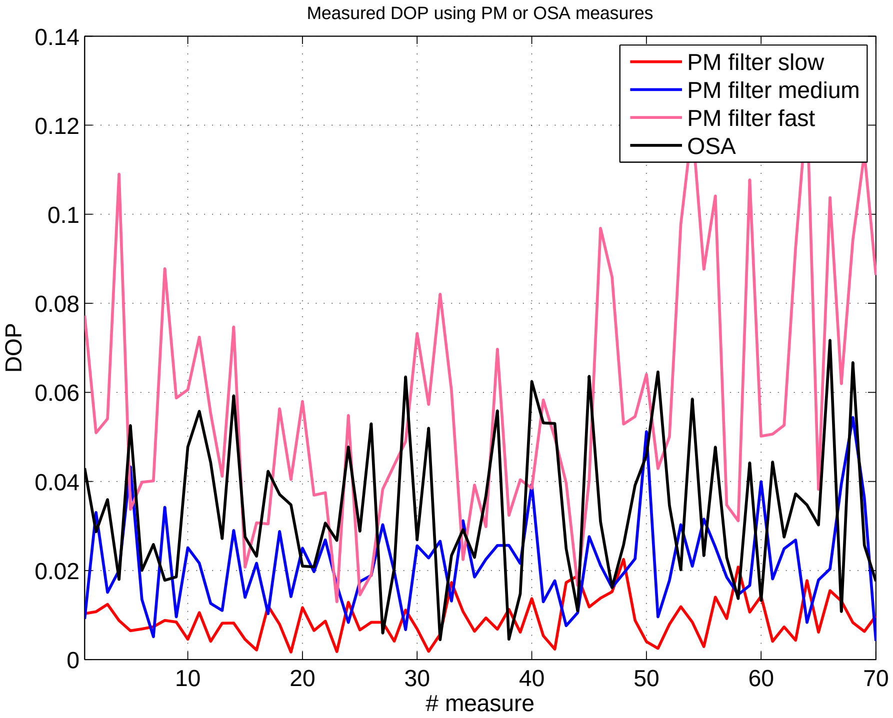

Figure 4.3: Evolution of DOP measured with the two instruments during the test, with scrambler set in “Deterministic Randomizer” mode.

4.2.2 “Deterministic SOP Scanner” scrambling mode

The configuration of the scrambler is:

- SOP grid: 20 deg;
- control period: $150\ \mu$s;
- control steps per SOP: 1;
- coverage time: 16.15 ms.

The test consists of 86 successive measurements of SOP and DOP by the polarimeter with the chosen scheduling of the acquisitions. DOP evolutions measured by PM and OSA are plotted in Fig. 4.4. In Tab. 4.2 there are the mean values of DOP in the test, in all the instrumental cases. It must be said that the scrambler operating in this modality does not appear to provide

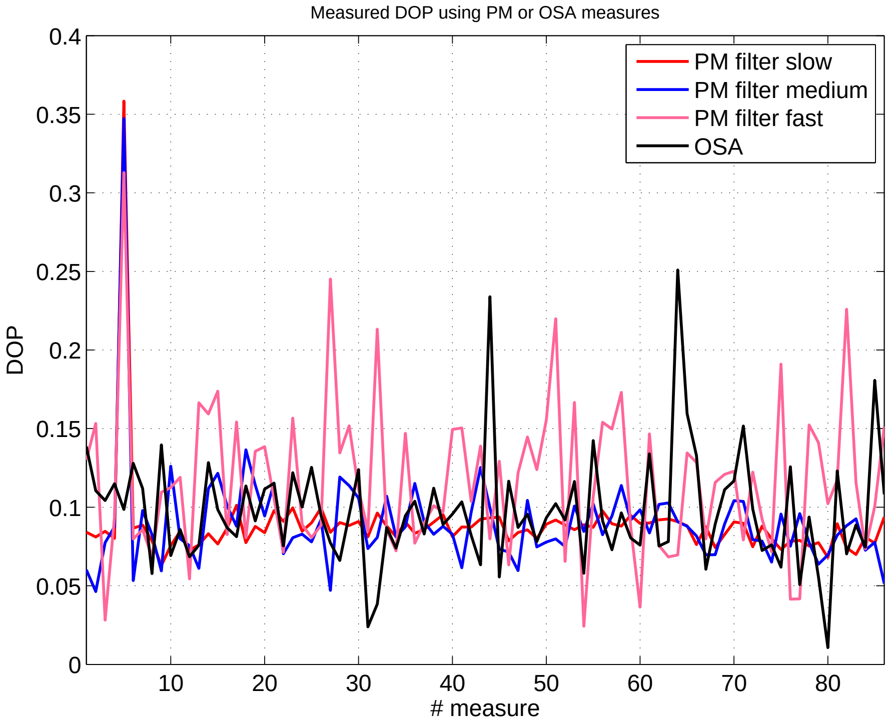

Figure 4.4: Evolution of DOP measured with the two instruments during the test, with scrambler set in "Deterministic SOP Scanner" mode.

stable results. In particular, we have repeated this test with the same configuration more times obtaining very different mean values of DOP. Although this test is not systematic, it can already be deduced that this scrambling modality is problematic.

	PM "slow" mod.	PM "medium" mod.	PM "fast" mod.	OSA
mean of DOP	0.0884	0.0899	0.1171	0.0977

Table 4.2: Mean values of DOP in the test.

4.2.3 "Fast Deterministic SOP Scanner" scrambling mode

The scrambler is configured as follows:

- SOP grid: 20 deg;
- control period: $100\ \mu$s;
- control steps per SOP: 1;
- coverage time: 15.93 ms.

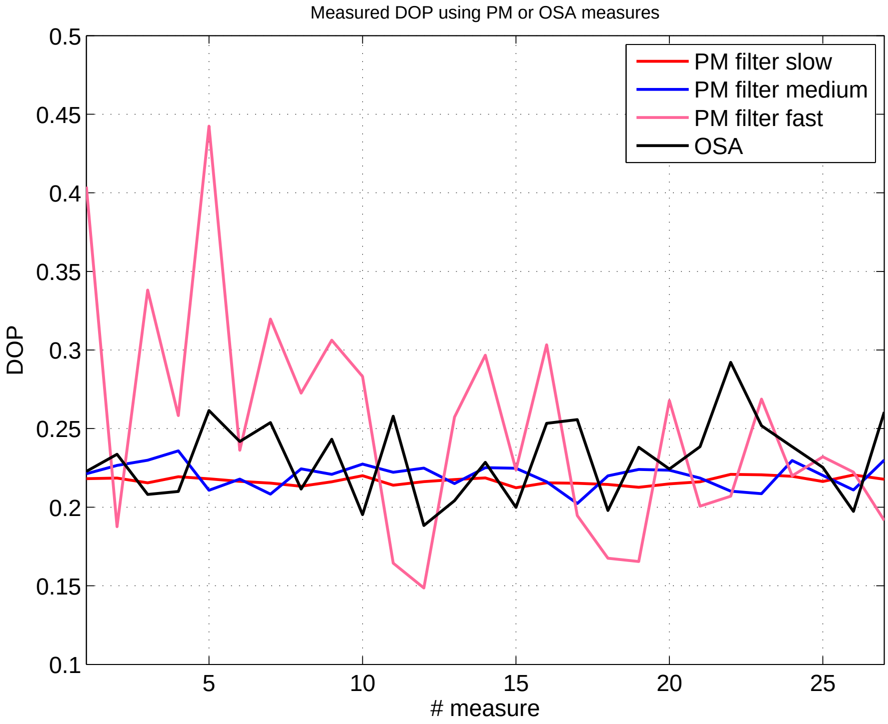

Figure 4.5: Evolution of DOP measured with the two instruments during the test, with scrambler set in "Fast Deterministic SOP Scanner" mode.

The test consists of 26 successive measurements of SOP and DOP by the polarimeter with the chosen scheduling of the acquisitions. The number of measurements made is so low because we immediately realize that DOP is too high; hence, this scrambling modality is less interesting. Nevertheless, the curves of DOP measured by PM and OSA are plotted in Fig. 4.5. In Tab. 4.3 there are the mean values of DOP in this test, in all the instrumental cases.

	PM "slow" mod.	PM "medium" mod.	PM "fast" mod.	OSA
mean of DOP	0.2168	0.2203	0.2511	0.2309

Table 4.3: Mean values of DOP in the test.

4.2.4 Observations

From this first not systematic analysis it can be deduced that only the "Deterministic Randomizer" scrambling mode allows to obtain a sufficiently low DOP (<0.01 in the best case) and good repeatability. The "Deterministic SOP Scanner" mode does not give repeatable results in terms of DOP. The "Fast Deterministic SOP Scanner" mode is characterized by too high values of DOP.

Consequently, probably only the first scrambling mode is exploitable in an experiment in which it is necessary to generate a scrambled signal with low DOP and with good repeatability.

Another interesting observation is that the mean values of DOP obtained with OSA are always greater than those measured by PM in "medium" modality but lower than those measured by PM in "fast" filtering modality. This suggests that the *detection bandwidth* of the OSA with this configuration is between the bandwidth of PM in "fast" modality and that in "medium" modality.

4.3 Systematic characterization of the scrambler

We systematically test the 3 modes of scrambling, varying their characteristic parameters. Measurements are carried out with PM (set in its three modes of filtering) and with OSA, as the precedent experimental step. The configuration of the OSA is the same as in Sec. 4.2. The chosen configurations of the scrambler, the numbers of measurements and the measured DOP values in the tests are all listed in Tab. 4.4 and Tab. 4.5. The values of DOP in the tables are obtained by an arithmetic mean of all the values obtained during the test. Concerning the measurements deriving from the power meter acquisitions, only those get with PM in "slow" filtering modality are reported because they are the most accurate, as already noted. The numbers of measurements done in the tests are different because the measurements last long and the amount of available time for a test is not always the same.

From the analysis of the data contained in the tables, it is deduced that the "Deterministic SOP Scanner" scrambling mode enables low DOP values only in certain cases. This fact is linked to the coverage time of the sphere. In fact, approximately, the higher the coverage time, the higher the measured DOP value. This is intuitive because the time interval "given" to a measuring of DOP is limited. This aspect must be taken into account when choosing the configuration to properly exploit this scrambling modality. It is also clear that the "Fast Deterministic SOP Scanner" is not good in all the cases, since DOP measured in correspondence to it is typically high. On the other hand, the "Deterministic Randomizer" mode of our scrambler enables to measure low values of DOP (< 0.09) with both the tested configurations. Consequently, this scrambling modality is certainly the most useful in this context.

We also note that with the chosen configuration of the OSA, the value of DOP measured by this instrument can significantly differ from the value obtained with PM in "slow" filtering. This is due to the fact that the OSA provides a single measurement of the peak of the optical power in the span, calculated as the arithmetic mean of 1000 successive acquisitions at the same wavelength. Moreover, the measuring of OSA at the wavelength of the peak lasts less than the measuring of the PM with "slow" filter. This is a key point in our experiment, as explained in Sec. 2.2 about the relation between the measurement of DOP and the detection bandwidth of the instrument.

We can therefore consider acquiring the optical signal in the same span, with the same res-

Scrambling mode	Chosen scrambling parameters	Number of measur.	DOP from PM “slow” mod. (averaged)	DOP from OSA (averaged)
Deterministic Randomizer	-SOP grid: 20 deg -Control period: 150 μs -Control steps per SOP: 1	74	0.0289	0.0535
	-SOP grid: 20 deg -Control period: 150 μs -Control steps per SOP: 5	68	0.0178	0.0849
Deterministic SOP Scanner	-SOP grid: 15 deg -Control period: 300 μs -Control steps per SOP: 1 -Coverage time: 56.15 ms	69	0.0363	0.2099
	-SOP grid: 20 deg -Control period: 150 μs -Control steps per SOP: 1 -Coverage time: 16.15 ms	82	0.0355	0.1067
	-SOP grid: 25 deg -Control period: 150 μs -Control steps per SOP: 1 -Coverage time: 11.80 ms	80	0.1591	0.1833
	-SOP grid: 10 deg -Control period: 150 μs -Control steps per SOP: 1 -Coverage time: 63.02 ms	56	0.0425	0.1253
	-SOP grid: 5 deg -Control period: 150 μs -Control steps per SOP: 1 -Coverage time: 248.80 ms	53	0.2631	0.3144
	-SOP grid: 30 deg -Control period: 150 μs -Control steps per SOP: 1 -Coverage time: 7.168 ms	78	0.0651	0.1004

Table 4.4: Systematic characterization of the scrambler Thorlbas set in the first two modes: chosen parameters and measured DOP values.

Scrambling mode	Chosen scrambling parameters	Number of measur.	DOP from PM “slow” mod. (averaged)	DOP from OSA (averaged)
Fast Deterministic SOP Scanner	-SOP grid: 20 deg -Control period: 100 μs -Control steps per SOP: 1 -Coverage time: 15.93 ms	78	0.0734	0.1730
	-SOP grid: 15 deg -Control period: 100 μs -Control steps per SOP: 1 -Coverage time: 24.49 ms	60	0.4846	0.5888
	-SOP grid: 6 deg -Control period: 100 μs -Control steps per SOP: 1 -Coverage time: 149.30 ms	60	0.4846	0.5888
	-SOP grid: 25 deg -Control period: 100 μs -Control steps per SOP: 1 -Coverage time: 9.118 ms	50	0.5429	0.6339

Table 4.5: Systematic characterization of the scrambler Thorlbas set in “Fast Deterministic SOP Scanner” mode: chosen parameters and measured DOP values.

olution (which is the minimum) but with more sampling points, so that the distance between a wavelength-point in the span and the adjacent is less than the resolution selected for the acquisition. In so doing, exploiting an instrumental limit, it is possible to obtain more power measurements corresponding to the same wavelength (within the limit of resolution), each of which calculated as the arithmetic mean of 1000 acquisitions. Hence, the power measurements corresponding to the peak (in variable number, depending on the number of points of the acquired span) will be averaged out. We name this operation *peak averaging*. Therefore, an increase in the number of points in the span analysed by OSA causes an increase in the *equivalent* time duration of DOP measuring by OSA itself. Consequently, the value of this DOP measurement should become smaller and hence more comparable with that obtained with PM in “slow” filtering. This is caused by the fact that the measured value of the degree of polarization inherently depends on the time duration of the measurement itself. It must be noted that this is an indirect method of measuring the optical power at the central wavelength, whence the adjective “equivalent”.

Taking into account all this, new experimental tests are made. The configuration of the OSA is therefore:

- $\lambda_{\text{center}} = 1640$ nm;
- span: 2 nm;
- $51, 101, 251, 501, 1001,$ or 1001 wavelength-points (sampling points) uniformly distributed in the span;
- 1000 power acquisitions for each wavelength-point, and an average of them;
- resolution: 0.07 nm;
- Video-BandWidth: VBW = 10 Hz.

Regarding the scrambler, reminding the results obtained before, we choose the "Deterministic Randomizer" mode with the configuration that enables the best results in terms of DOP. For the sake of completeness, we decide to test also the "Deterministic SOP Scanner" mode with the same value for the parameters. This configuration of the scrambler's parameters, the same for both the tested modes, is:

- SOP grid: 20 deg;
- Control period: 150 μs;
- Control steps per SOP: 1.

All the parameters characterizing the performed tests and the DOP values measured in three different modalities are listed in Tab. 4.6. The measurements of DOP are always obtained by the arithmetic mean of all the measurements of DOP during the test. In the table there are also the durations of a single measurement in all the tests, which are characterized by different numbers of sampling points in the span acquired by OSA.

From the analysis of the data contained in Tab. 4.6, it is evident that an increase in the number of sampling points in the span produces a significant increase in the measuring durations, arriving to values greater than 10 min. This fact could be deleterious if there is the necessity to collect a certain number of measurements or, even worse, if an observation of a rapidly variable phenomena is required during the experiment. But an increase in the number of sampling point induces also a decrease in the measured value of DOP using the "peak averaging", as expected. But this happens only for the "Deterministic SOP Scanner" scrambling mode, because the period of generation of the SOPs grid on the sphere of this mode is already smaller than the acquiring time of a single point in the span. This makes useless increasing the equivalent measurement time conveniently produced employing the "peak averaging". With the "Deterministic Randomizer"

Scrambling mode	Number of sampling points OSA	Number of measur.	Time per measur. of SOP [min]	DOP from PM "slow" mod. (averaged)	DOP from OSA without *peak averaging* (averaged)	DOP from OSA with *peak averaging* (averaged)
Deterministic Randomizer	51	74	2.2	0.0289	0.0535	0.0535
	101	41	3.4	0.0353	0.0752	0.0649
	251	23	7	0.0301	0.0548	0.0384
	501	14	12	0.0217	0.0528	0.0292
	1001	14	12.5	0.0577	0.0575	0.0349
	2001	24	14	0.0164	0.0514	0.0229
Deterministic SOP Scanner	51	69	2.2	0.0363	0.2099	0.2099
	101	43	3.4	0.1350	0.1504	0.1528

Table 4.6: Systematic characterization of the scrambler Thorlbas without or with the use of *peak averaging* to measure DOP with OSA: chosen parameters and measured DOP values.

mode, instead, the "peak averaging" has a significant effect beacause a longer time means a greater coverage of the sphere by the generated SOP points, since they are randomly generated.

Summarizing, the measured DOP values obtained with OSA can be very close to those deriving from PM, and hence sufficiently low, if the scrambler is set in its best scrambling configuration and if the "peak averaging" is employed. But this approach produces a significant increase in the duration of the polarization's measuring.

Chapter 5

Characterization of a more performant polarization scrambler

With the scrambling system described and tested in the previous Chapter, the measured DOP is frequently not sufficiently low, as expected. The main cause is due to structural limitations of the OSA. Nevertheless, with the already performed tests on scrambling, many information about the accuracy of the polarimeter has been collected. This Chapter therefore describes the experimental characterization of a second, more performant polarization scrambler based on piezoelectric squeezers. The constructor declares that this device is very performant, in the sense that it should guarantee a good coverage of the Poincaré sphere with a scrambling frequency of 1 kHz. We verify its characteristics in some different tests. The methods of measuring and analysis are presented. In particular, we focus on the frequency response and on the settling-time when analog step signals are applied to the electrical inputs. Considerations about the scrambling capability of this device are hence deduced from the measured electrical parameters.

5.1 Characteristics of the new scrambler

We want to test and characterize a *General Photonics PCD-M02*, which is depicted in Fig. 5.1. This device contains a PolaRITE$^{\text{TM}}$III polarization controller based on piezoelectric squeezers. The piezoelectric actuators are controlled by a MPD-001 multiple channel driver board. The constructor declares high precision, low noise, low drift and high voltage for this card ([21]). The card provides sufficient driving voltage to drive up to four piezoelectric actuators. The output driving voltages are controlled by external analog or digital signals.

This device can be used mainly for three purposes: *Dynamic polarization control*, *Polarization stabilization* and, specially for our tests, *Polarization scrambling*.

Regarding the Dynamic polarization control, the PCD-M02 can be used to transform any arbitrary input state of polarization (SOP) to arbitrary output SOP. With the aid of a polarization

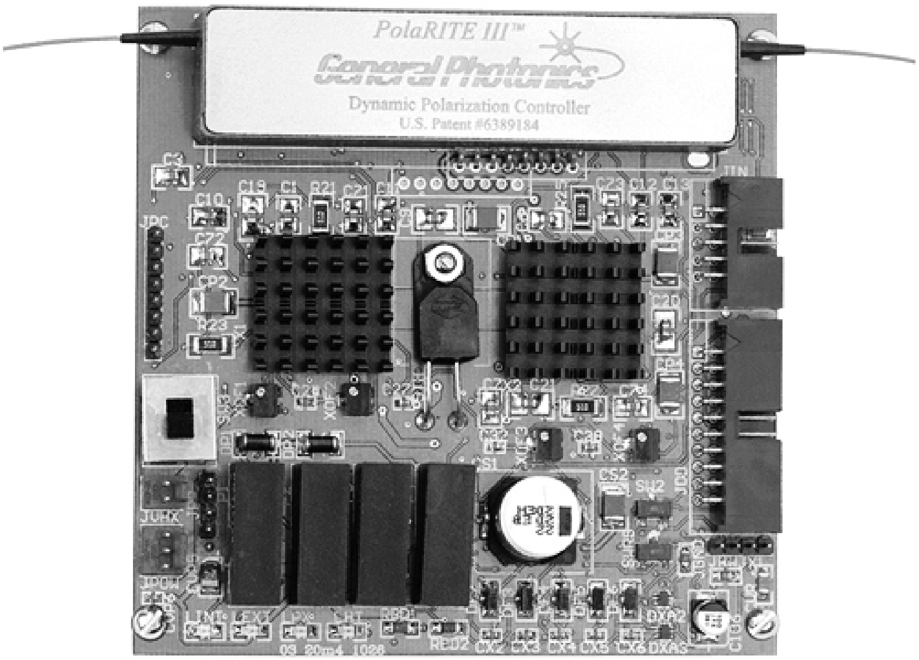

Figure 5.1: General Photonics PCD-MO2 package, containing an all fiber dynamic polarization controller module (with scrambling capability) and its controller board. (From [21].)

detection device, it is possible for the user to electronically control the voltage applied to each channel to adjust the out SOP. For the Polarization stabilization, using the appropriate feedback electronics and control algorithm, this device can be part of a polarization stabilization system. The feedback signal can be the maximum (or minimum) optical power output through a polarizer, ore the maximum (or minimum) output voltage of a modulation signal.

We use the PCD-M02 for its polarization scrambling capability. In particular, with reference to the characteristics declared by the constructor ([21]), it can be used as a low speed polarization scrambler to randomize the input SOP. The control signals, one for each electrical input channel, can be 4 random step voltages or 4 sine-wave voltages with the following peak-to-peak voltage and frequency relationship:

$$V_{i,pp} = 1.531 V_{\pi,i} \ , \quad i = 1, \ldots, 4 \ , \tag{5.1}$$

$$n f_i \neq m f_j \ , \quad n = \pm 1, \pm 2, \ldots, \quad i, j = 1, \ldots, 4, \ \text{and } i \neq j \ , \tag{5.2}$$

where $V_{\pi,i}$ is the half-wave voltage for the i-th channel[1]. The scrambling frequencies are unfortunately limited by power supply constraints or circuit current limits. For a PolaRITE II/III in off-resonance mode, the *declared maximum scrambling frequency is about* 1 *kHz*. The low polarization dependent loss (PDL) and the polarization scrambling capability can be very useful in optical components PDL measurement.

5.2 Measurement of the frequency response of the scrambler

It is necessary to collect information about the frequency response of this device. In particular, we want to know the value of the maximum frequency we can assign to the electrical input signal. Substantially, after having measured the frequency response, the -3dB bandwidth is evaluated. The aim of this experimental test is therefore to obtain a qualitative and precautionary measurement of the frequency range in which the scrambler can operate without producing significant distortions to the output signal.

To perform this experimental activity, the setup represented in Fig. 5.2 is employed. The laser source generates an optical signal with a wavelength of 1550 nm and a power of 0 dBm, which is directed to a manual polarization controller and then to the optical input of the General Photonics scrambler.

The electrical signals are generated by a National Instruments DAQ board (*NI-USB 6211*), which is also capable to detect external signals. The outputs and the inputs of this board are all characterized by high impedance. The DAQ board is controlled by LabView software installed in a computer. The electrical output of the DAQ board is connected to the channel1 of the scrambler, whose optical output is detected by a proper photo-diode. The photo-diode has a very

---

[1] In this context, the half-wave voltage is the voltage required for inducing a phase change of 180° along a circumference (on the Poincaré sphere) to the input SOP.

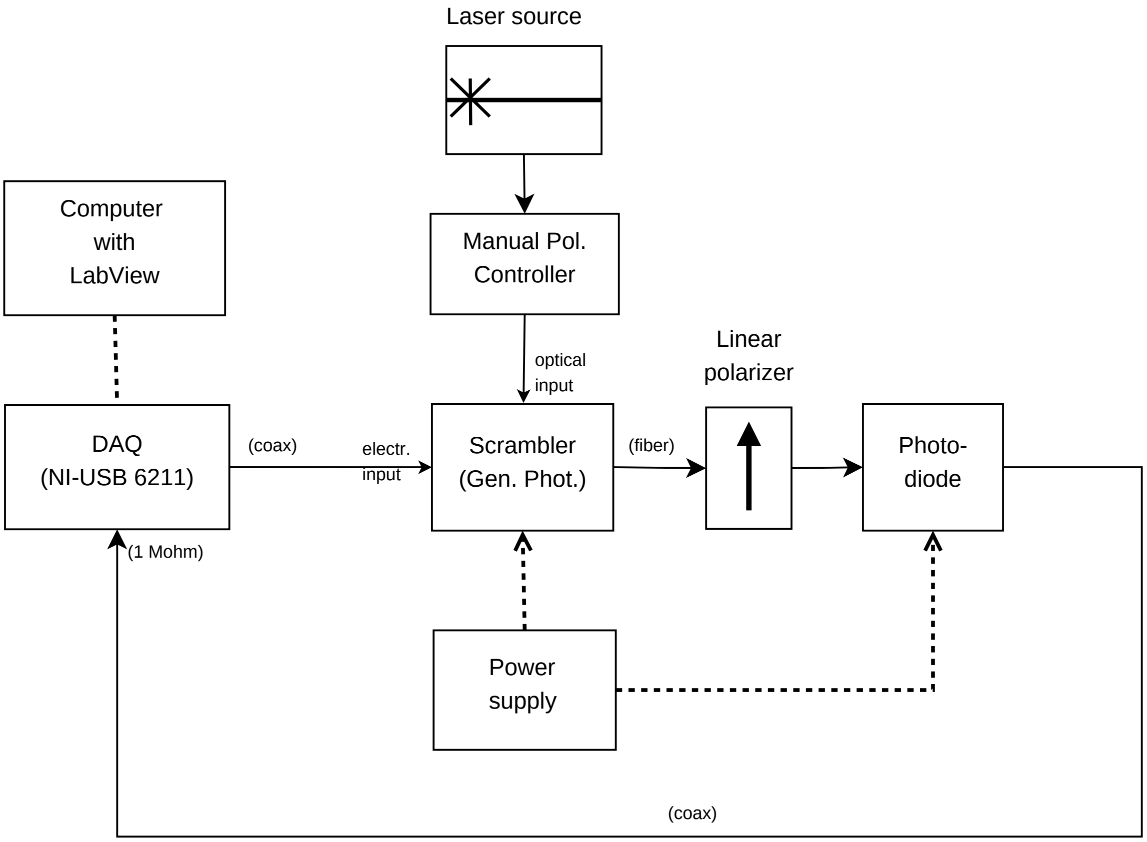

Figure 5.2: Experimental setup for the measurement of the dependence of the forward transmission coefficient of the scrambler from frequency.

large bandwidth and a good responsivity (44 V/W). The experimental setup, represented in Fig. 5.2, contains also a manual polarization controller and a linear polarizer. These devices enable to maximize the polarized optical power at the input of the photo-diode by a proper alignment of the polarization controller to the input SOP.

Regarding the measuring method, we use the Swept-Sine Analysis. Swept-Sine is a signal processing technique used to obtain the frequency response of a system by applying a swept in frequency of input/excitation tones and analysing the response to each of them. In detail, a swept sine measurement is a sine sweep that steps through a specified sequence of frequency points. At each frequency, the source tone is maintained and the inputs to the analyzer (the DAQ board in our case) are measured only at that source frequency. Both magnitude and phase of each component are measured so that the frequency response of input/output systems can be characterized. After each measurement, the source frequency is therefore adjusted to the next frequency in the sweep sequence, and a new measurement is taken at this new frequency. We observe that, comparing the swept-sine measurement technique to the FFT measurement, the swept-sine technique measures only one line at a time and is therefore much slower than the FFT which measures a group of frequencies simultaneously.

A clarification is necessary now. Since we have realized impedance-matching at the electrical input of the scrambler and at the output of the photo-detector, the frequency function we are measuring is a *forward transmission coefficient*, i.e. the scattering parameter called $S_{2,1}$ (if port "1" is the electrical input of the scrambler). Therefore, the frequency response of the device is measured in the sense that the transmission coefficient is characterized in frequency ($S_{2,1}(f)$).

The swept-sine analysis is performed by LabView software which controls the generation and the acquisition of the electrical signals through the DAQ board connected to the computer. We choose these parameters for the swept analysis:

- start frequency: 100 Hz;
- stop frequency: 25 kHz;
- number of step-points: 1000 or 5000.

The amplitude and the DC offset of the tone at the input of the scrambler are varied in a range such that the voltage value of the generated signal always belongs to the interval $[0, 4]$ V. The high level is chosen lower than 5 V as a precaution, because it is known that an analog input voltage greater than 5 V could damage the device. The parameters used in the test and the corresponding measured frequency responses are reported in Tab. 5.1. In the table also the corresponding -3dB bandwidths are present. In Fig. 5.3 there are the plots of the frequency response or, more precisely, of the forward transmission coefficient as a function of the frequency, only in some cases, for reasons of brevity. Both magnitude and phase are shown.

It can be observed that the magnitudes of the frequency responses are sufficiently regular in their bandwidths. The -3dB bandwidths are always greater than 8.5 kHz and lower than 10.5

Input signal at Channel1 of scrambler		Sweep modality	Frequency response	
Amplitude (peak-peak) [mV]	DC offset [mV]	Number of steps	-3dB bandwidth [kHz]	Figure
500	350	1000	10	-
400	350	1000	10	-
300	350	1000	10.1	-
200	350	1000	10.1	Fig. 5.3(d)
700	500	1000	8.5	Fig. 5.3(a)
300	500	1000	10	-
300	500	5000	10.5	-
800	1000	1000	8.5	-
400	1000	1000	10.5	-
300	1000	1000	10.5	-
800	2000	1000	9	Fig. 5.3(b)
400	2000	1000	11	-
300	2000	1000	10.4	-
200	2000	1000	10.2	-
800	3000	1000	9.5	Fig. 5.3(c)
400	3000	1000	10.3	-
300	3000	1000	10.5	-
200	3000	1000	10.2	-

Table 5.1: Characteristics of the input signals, number of steps of the sweep and measured bandwidth of the frequency responses in the swept-sine test. In correspondence to the plotted frequency responses there are the numbers of the respective figure.

kHz. Moreover, from this test, we can not observe any dependence of the 3-dB bandwidths on the amplitude of the input signal, although the constructor declares a certain dependence. However, it can be stated that the -3dB bandwidth of this device is substantially equal to 9 kHz. We must observe that the constructor declares a -3dB bandwidth equal to 16 kHz.

5.3 Measurement of the settling time of the scrambler

This scrambler will be used in the polarization attraction experiment, explained in Chapter 1. To scramble the SOP of the input optical signal, a square-wave with random amplitudes will drive the piezoelectric actuators. This should guarantee a good coverage of the Poincaré sphere by the SOP and a scrambling rate tunable in a sufficiently wide range to adapt to the acquisition rates of the available detection instruments. It is therefore necessary to collect information about the response of the scrambler to a square-wave at the electrical input. In particular, the *settling time* is a fundamental parameter to measure. In fact, it is defined as the time elapsed from the application of an ideal instantaneous step input to the time at which the device output has entered and remained within a specified error band (usually symmetrical about the final value). Consequently, it gives a precise indication of the response velocity of the device. In the following, this parameter is analytically defined and measured.

The experimental setup used for this test is very similar to the setup of Fig. 5.2 employed for the measurement of the frequency response of the scrambler. The main differences between this new configuration, represented in Fig. 5.4, and the old one, are a waveforms generator *Agilent 33250A* to generate the electrical signals at the input of the scrambler, and a digital oscilloscope (DSO) to visualize and digitally acquire the signals at the output of the photo-diode. The waveforms generator is more efficient than the DAQ board in the generation of waveforms, hence it is included in this setup. Impedance matching is realized in all the connections.

5.3.1 Preliminary test of the configuration

As a preliminary test, we generate three square-waves with the same period and duty-cycle but with different amplitudes to acquire the signals at the output of the photo-diode. Only the Channel1 of the scrambler has a non-zero input. In detail, the square waves have a 50% duty-cicle and a frequency of 100 Hz, and hence a period of 10 ms. Three different amplitudes are tested: $0.75V_{\pi,1}$, $0.75V_{\pi,1} + 2V_{\pi,1}$ and $0.75V_{\pi,1} + 4V_{\pi,1}$, where $V_{\pi,1} = 0.893$ V is the half-wave voltage for the Channel1. A voltage value of $0.75V_{\pi,1}$ V is chosen because it corresponds to less than a rotation of $180°$ on the Poincaré sphere by the SOP of the scrambled signal, and therefore the detected signal is not distorted. In fact, due to the linear polarizer after the scrambler, if a voltage greater than $V_{\pi,1}$ V is applied to the electrical channel of the scrambler, the SOP of the signal rotates of an angle greater than $180°$; hence, the linearly-polarized component of the signal oscil-

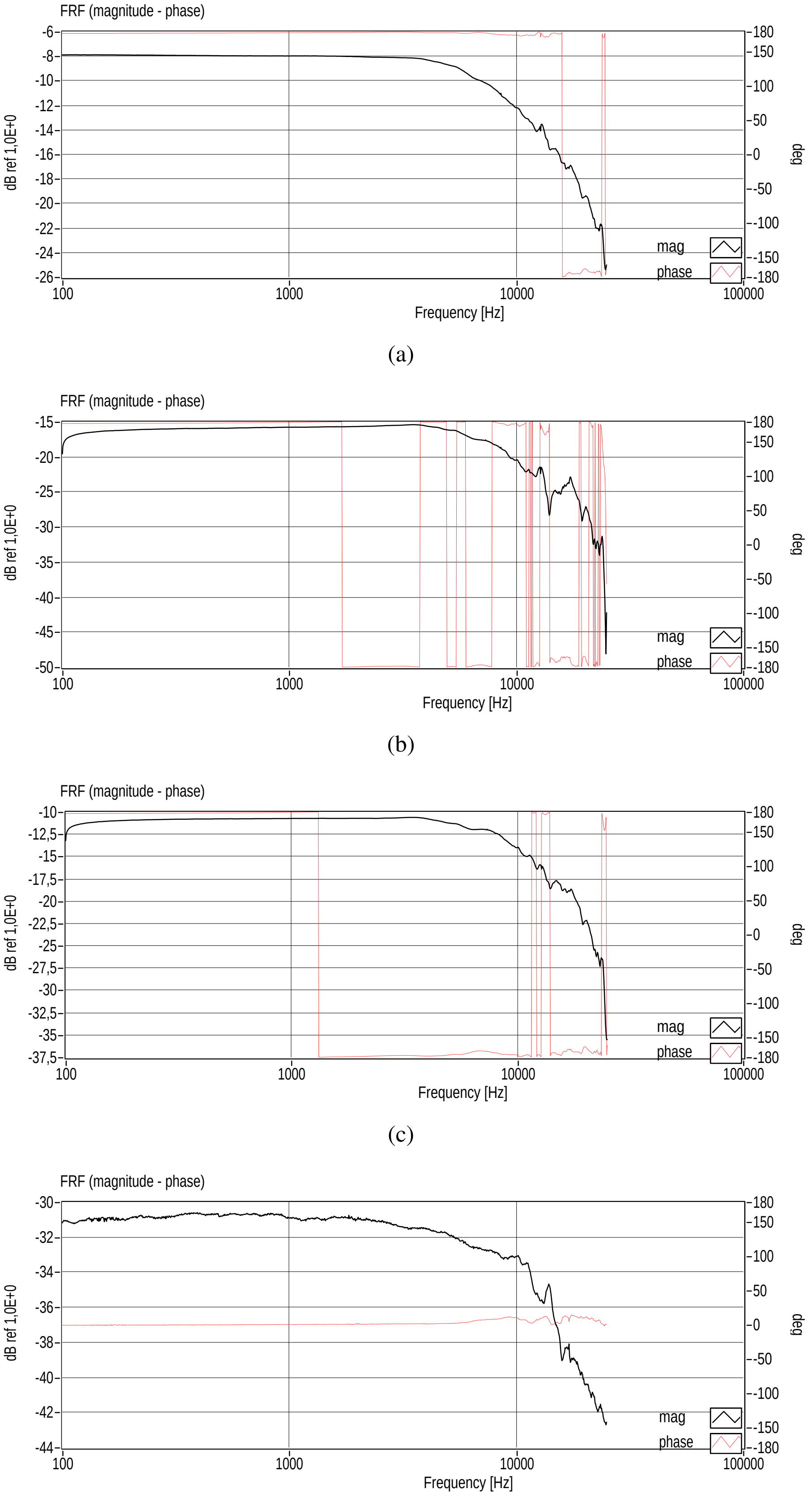

(a)

(b)

(c)

(d)

Figure 5.3: Some relevant measured frequency responses (transmission coefficient). Both magnitude and phase are represented. The experimental parameters in correspondence to which they are measured are listed in Tab. 5.1.

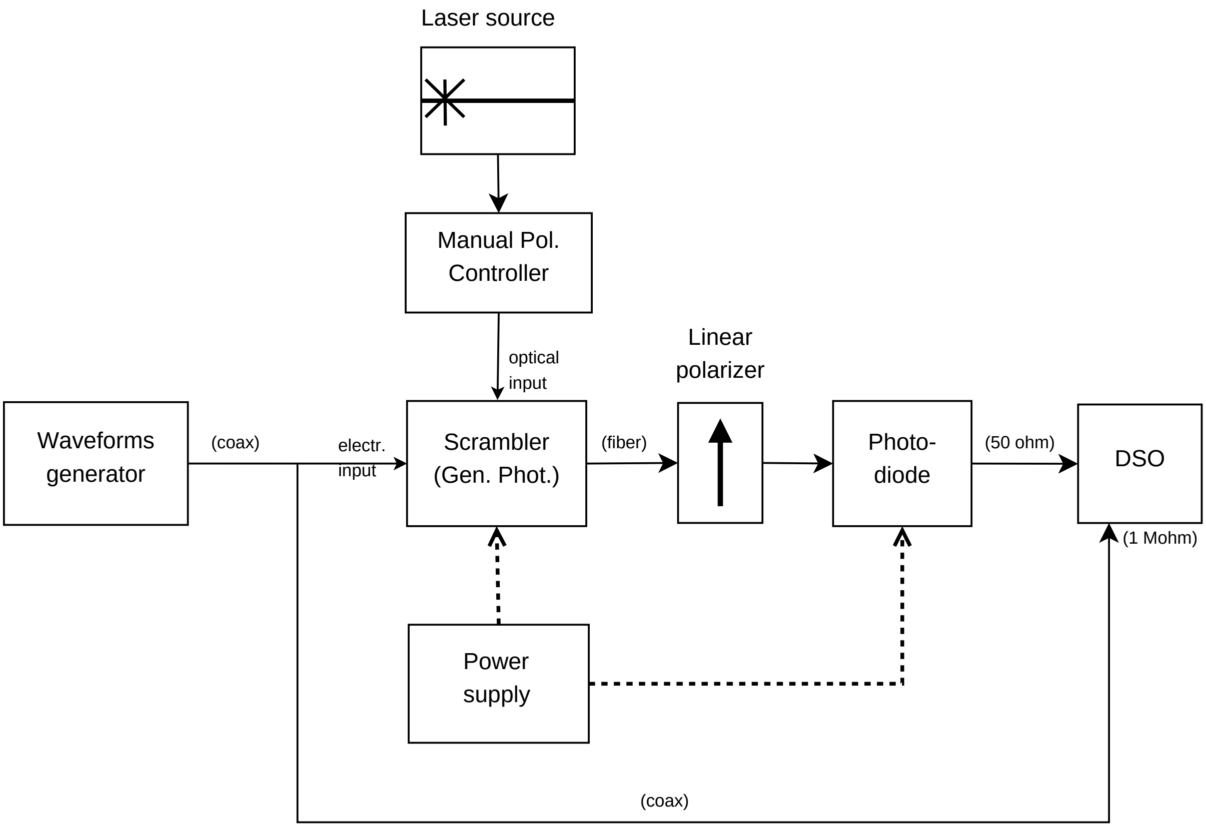

Figure 5.4: Experimental setup for the measurement of the settling-time of the General Photonics scrambler.

lates around its mean value. However, the voltage values for this test are arbitrary, but properly chosen.

Both the input and output signals are detected and digitally acquired by the DSO. The digital acquisitions are set in “High-Resolution” modality, for both the time axis and the amplitude axis. The signals acquired in correspondence to the three different increasing analog step amplitudes are plotted in Fig. 5.5. It is evident that an increase in the amplitude of the square wave induces oscillations on the detected output signal (in correspondence to the transition of the square-wave) for the reasons explained above.

5.3.2 Systematic measurements of the settling time

According to the above explanations, different definitions can be given to the settling time of a device. Settling time includes a very brief propag. delay, plus the time required for the output to slew to the vicinity of the final value, recover from the overload condition associated with slew, and finally settle to within the specified error. Hence, settling time can be defined as the time required for the response curve to reach and stay within a range of certain percentage (usually 5% or 2%) of the final value. In Fig. 5.6 a representation of the concept of settling time is shown.

Because of the non uniqueness of the settling time definition, we decide to measure it using some definitions which can be considered as different objectifications of the above concepts. We firstly introduce these quantities:

- low_level_out: the low level of the response voltage signal (V_1 in Fig. 5.6);
- high_level_out: the high level of the response voltage signal (V_2 in Fig. 5.6);
- ref_value: the quantity which defines the error band, that is the range of amplitude inside which the response signal oscillates after (or before) the settling time, as in Fig. 5.6;
- ref_value_low: the same definition applied to the low level of the signal (the error band of the high level is in general different from the error band of the low level);
- ref_value_high: the same definition applied to the high level of the signal;
- sigma_low_level_out: the standard deviation of the amplitude of the signal in a proper time interval in which the are no oscillations, at low level;
- sigma_high_level_out: the same definition as above for the high level;
- sigma_noise: the level (calculated as standard deviation) of the additive thermal noise, measured with no inputs to the system;
- Delta_absolute: the maximum (measured) range of amplitude of the response signal, to be used as a reference value.

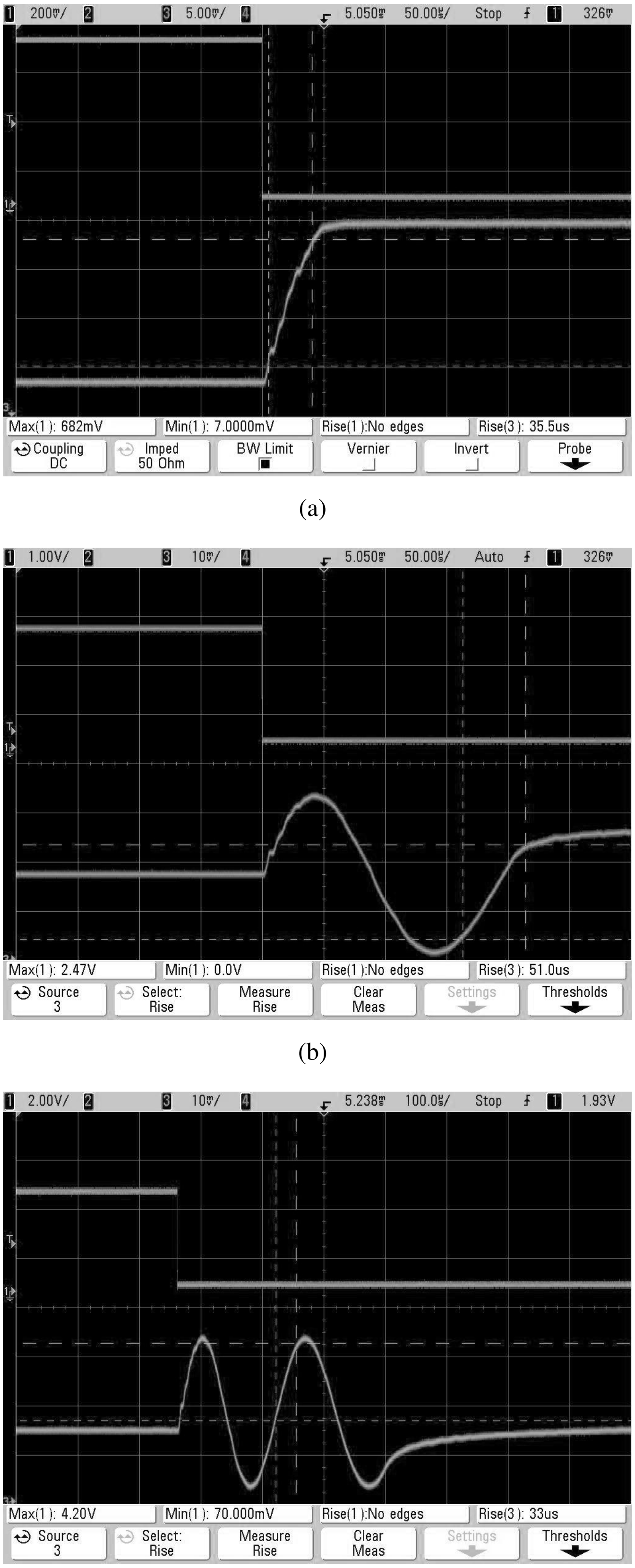

1 200mV/ 2 3 5.00mV/ 4 5.050ms 50.00µs/ Stop 1 326mV

Max(1): 682mV | Min(1): 7.0000mV | Rise(1):No edges | Rise(3): 35.5us

(a)

1 1.00V/ 2 3 10mV/ 4 5.050ms 50.00µs/ Auto 1 326mV

Max(1): 2.47V | Min(1): 0.0V | Rise(1):No edges | Rise(3): 51.0us

(b)

1 2.00V/ 2 3 10mV/ 4 5.238ms 100.0µs/ Stop 1 1.93V

Max(1): 4.20V | Min(1): 70.000mV | Rise(1):No edges | Rise(3): 33us

(c)

Figure 5.5: Preliminary test with square-waves at the input, with different amplitudes of the square-wave: $0.75V_{\pi,1}$ (a), $0.75V_{\pi,1} + 2V_{\pi,1}$ (b) and $0.75V_{\pi,1} + 4V_{\pi,1}$ (c). In each plot are present the input step signal (up) and the corresponding response of the scrambler (down).

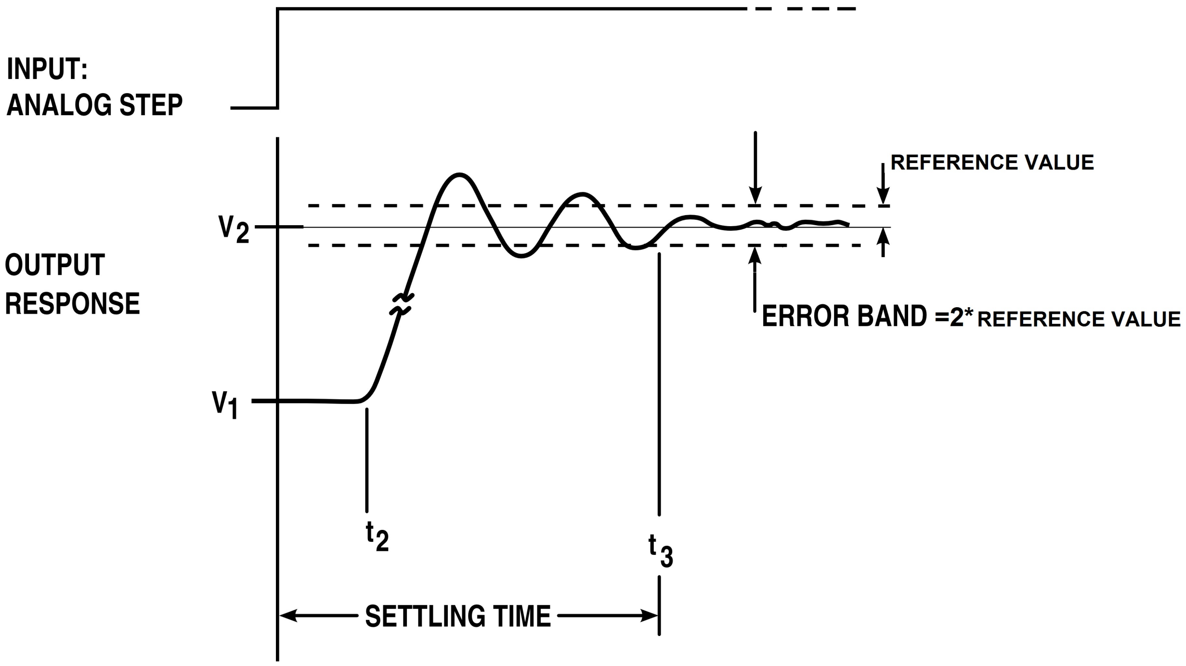

Figure 5.6: Settling time representation. (Adapted from [22].)

The chosen definitions for the settling-time are therefore contained in the following Paragraph.

Settling time definitions

```
-Definition_1:
    ref_value = max([3*sigma_noise (high_level_out-low_level_out)/20]);
    ref_value_low = ref_value;
    ref_value_high = ref_value;

-Definition_2:
    ref_value_low = max([3*sigma_low_level_out (high_level_out-low_level_out)/20]);
    ref_value_high = max([3*sigma_high_level_out (high_level_out-low_level_out)/20]);

-Definition_3:
    ref_value = max([10*sigma_noise (high_level_out-low_level_out)/20]);
    ref_value_low = ref_value;
    ref_value_high = ref_value;

-Definition_4:
    ref_value_low = max([10*sigma_low_level_out (high_level_out-low_level_out)/20]);
```

```
    ref_value_high = max([10*sigma_high_level_out (high_level_out-low_level_out)/20]);

-Definition_5:
    ref_value = max([3*sigma_noise (high_level_out-low_level_out)/10]);
    ref_value_low = ref_value;
    ref_value_high = ref_value;

-Definition_6:
    ref_value_low = max([3*sigma_low_level_out (high_level_out-low_level_out)/10]);
    ref_value_high = max([3*sigma_high_level_out (high_level_out-low_level_out)/10]);

-Definition_7:
    ref_value = max([10*sigma_noise (high_level_out-low_level_out)/10]);
    ref_value_low = ref_value;
    ref_value_high = ref_value;

-Definition_8:
    ref_value_low = max([10*sigma_low_level_out (high_level_out-low_level_out)/10]);
    ref_value_high = max([10*sigma_high_level_out (high_level_out-low_level_out)/10]);

-Definition_9:
    ref_value = Delta_absolute/10;
    ref_value_low = ref_value;
    ref_value_high = ref_value;

-Definition_10:
    ref_value_low = max([3*sigma_low_level_out Delta_absolute/10]);
    ref_value_high = max([3*sigma_high_level_out Delta_absolute/10]);

-Definition_11:
    ref_value = Delta_absolute/20;
    ref_value_low = ref_value;
    ref_value_high = ref_value;

-Definition_12:
    ref_value = Delta_absolute/40;
    ref_value_low = ref_value;
    ref_value_high = ref_value;
```

-Definition_13:
ref_value = Delta_absolute/50;
ref_value_low = ref_value;
ref_value_high = ref_value;

The test consists in driving the Channel1 of the scrambler with analog step signals with these amplitudes: $k * 0.25V_{\pi,1}$, with $0 \leq k \leq 23$ integer; in fact, with $k = 23$ the applied voltage is lower than 5 V, but with $k = 24$ it is not. The amplitudes values are arbitrary chosen to cover many cases. By means of the manual polarization controller, the optical power at the output of the linear polarizer is minimized, i.e. the SOP of the not-scrambled laser source and the linear polarization characterizing the polarizer are orthogonal. We use this alignment as a reference for all the measurements.

The settling time values of the acquired digital signals are evaluated by Matlab software according to the above definitions. In Fig. 5.7(a) the settling times are plotted as functions of the input voltage at Channel1, which is the only channel with a non-zero input. We repeat the same test driving all the four electrical channels of the scrambler with the same analog-step signals. The results, according to the same definitions, are presented in Fig. 5.7(b).

From the observation of these plots, it is evident that using certain definitions we obtain very high settling times. This is due to the fact that the error bands imposed by those definitions are too much low. In fact, if the error band is very low, the oscillations of the signal can easily be greater than it producing a very large settling time interval. These very high values evidently must be ignored. We observe that the other values of settling time increase with the input voltage, as must be. Moreover, most of them are lower than 1 ms. The same considerations can be made for the case of all the four channels with non-zero inputs.

Consequently, to complete the analysis, we consider only the definitions giving reasonable results for the settling time, plotting them in Fig. 5.8. We observe that the definitions giving reasonable results are those which contemplate different error bands for high and low level. It can be deduced from the plot that an input voltage in the range $[0, 1.5]$ V guarantees a settling time of the response sufficiently lower than 1 ms. Hence, the scrambler should be driven with voltages in that range to obtain higher scrambling rates.

As a final consideration, we remember that the declared maximum scrambling frequency is 1 kHz. This value of the maximum frequency means that the minimum time between the generations of two different SOPs by the polarization scrambler is 1 ms. Such a value is therefore consistent with the measured settling time lower than 1 ms, in the sense that the scrambling rate is strongly dependent on the settling time of the device.

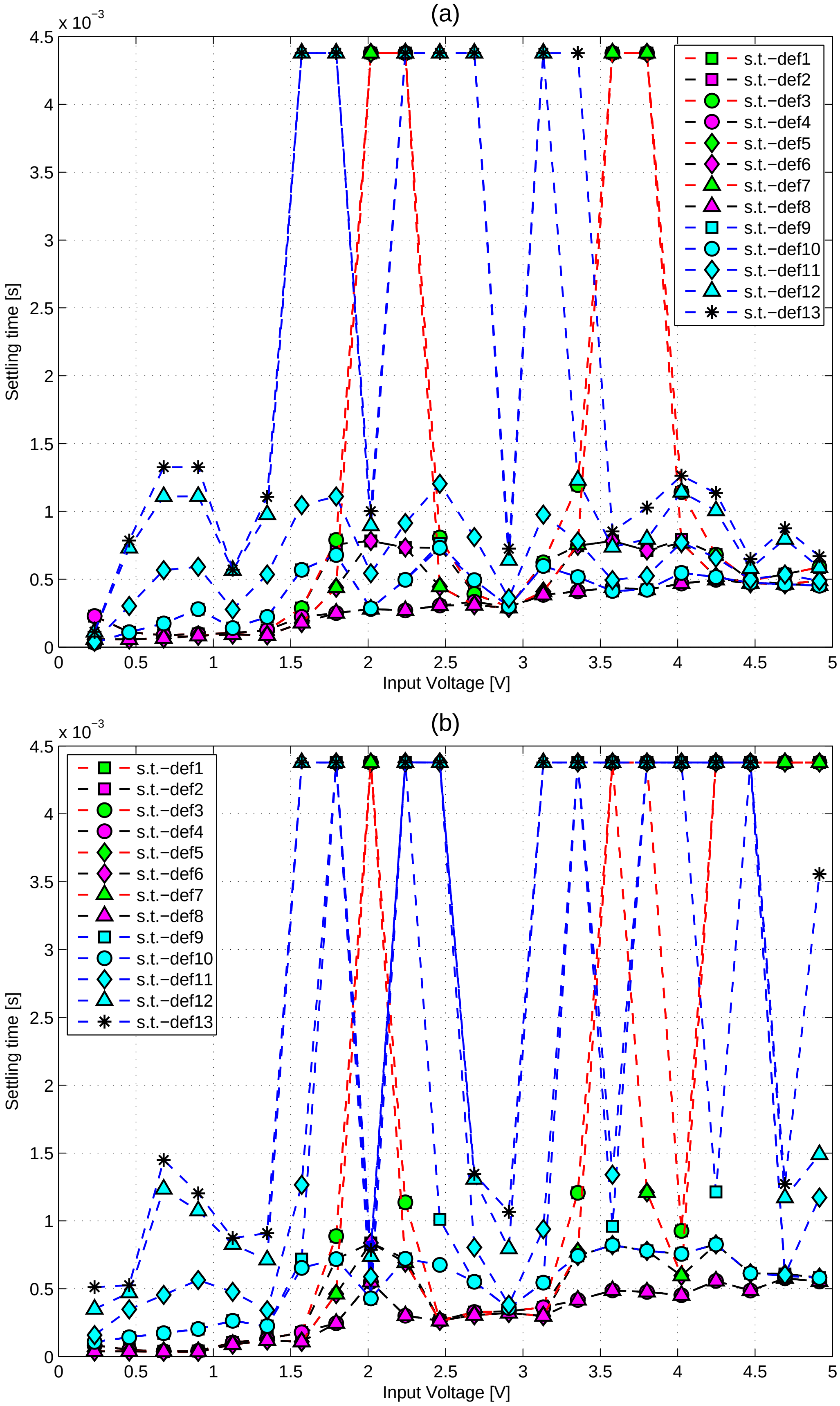

Figure 5.7: Settling times as functions of the input voltage when only Channel1 of the scrambler has non-zero input (a), when all the four channels are driven by the same analog step signal (b).

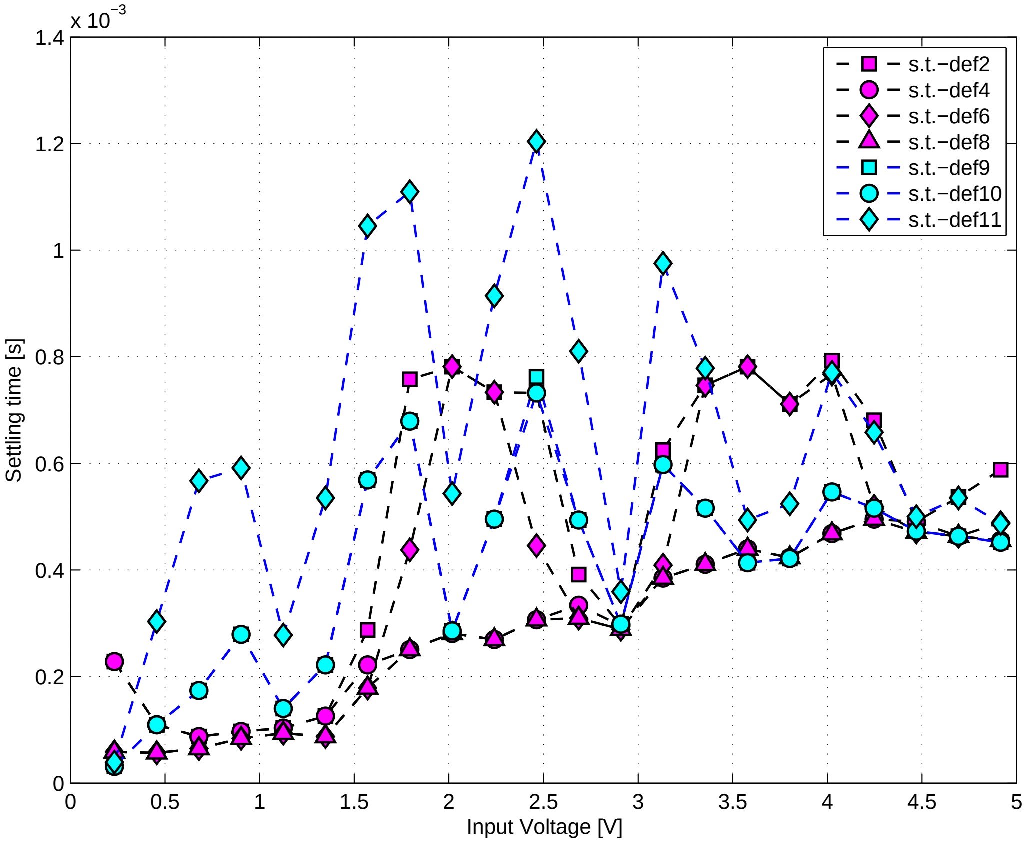

Figure 5.8: Settling times as functions of the input voltage when only Channel1 of the scrambler has non-zero input. Only some definitions are considered.

Conclusions

The first aim of this Thesis has been to study, test and characterize a polarimetric system to measure the state of polarization in counterpropagating FRAs polarization pulling experiments. These type of experiments, which should verify the repolarization capability of the SRS, needs in fact a suitable polarimeter.

We have firstly introduced the theoretical concepts necessary for the comprehension of polarization, polarization pulling, polarimeters and polarization scrambling.

We have therefore developed a polarimetric system employing a classical scheme formed by a birefringent rotative quarter-wave plate followed by a linear polarizer. From statistical analysis of a large number of SOP measurements in different situations, we have evaluated the appropriate number of rotation angles for the wave plate to obtain accurate and sufficiently fast SOP measurements. An interesting but troublesome temperature drift phenomenon has been observed. This phenomenon produces a slow but constant drift on SOP measurements, which should not variate when the source is totally polarized. To compensate the effect of this drift an analysis based on time windows has been used with positive results. In our experimental configurations we have employed both an optical power meter and an optical spectrum analyzer to make power measurements. We have tested various modalities of acquisitions of these instruments producing measurements with different durations. The accuracy of SOP and DOP measurements has been evaluated; in particular, the errors on DOP measurements provided by the OSA have been calculated considering the main experimental uncertainty's factors. These errors values characterize our polarimetric configuration.

The second aim of this experimental Thesis has been to generate polarization scrambled signals. Depolarized, or partially polarized, signals are necessary to experimentally verify the repolarization capability of NLPP schemes. Two different polarization scramblers, both based on piezoelectric squeezers, have been employed. The characterization of the first device has been obtained by means of the already used polarimetric system. We have tested different scrambling modalities and configurations of the detection instruments. We have also proved that with long acquisitions, as those of a power meter, the measured DOP of a scrambled source could be very low; instead, when the acquisitions at a certain wavelength are faster, as those provided by an OSA, which has structural limitations, the measured DOP is typically not sufficiently low. We have hence experimentally verified the dependence of DOP on scrambling frequency and on the detection bandwidth of instrumentation.

The second polarization scrambler, an OEM device, has shown good performance. The frequency response of this device has been measured by means of a swept-sine analysis. The measured -3dB bandwidth of the frequency response is approximately equal to 9 kHz, and it remains substantially constant when the driving voltages change. The measured settling time of the response to analog step input signals is lower than 1 ms, when the input voltages are not very high. We have measured these quantities applying many different input voltages and observing in each case the electrical behaviour of the scrambler. From these measured values it has been deduced that this device could produce a sufficiently high scrambling rate. In fact, after being tested in this Thesis, this scrambler has been successfully employed in a NLPP experiment. In particular, it has enabled to obtain a sufficiently low DOP, measured by the same polarimetric system, making the source depolarized.

Consequently, the polarimeter and the polarization scrambled signals generator tested in this Thesis can be employed in NLPP experiments obtaining correct results.

Ringraziamenti

Per lo svolgimento di questa Tesi sperimentale si ringraziano i prof. Luca Palmieri e Marco Santagiustina, e il dott. Fabrizio Chiarello del gruppo di Fotonica del Dipartimento di Ingegneria dell'Informazione dell'Università di Padova per la competenza, professionalità e disponibilità dimostrate.

Bibliography

[1] *IEEE Photonics Society Nesw* journal, vol. 25, no. 3, pp. 22-24, June 2011.

[2] *La Polarizzazione del Campo Electromagnetico*, didactic material of courses on Electromagnetic Fields, M. Santagiustina, L. Palmieri, a.a. 2007/08, DEI Unipd.

[3] E. Collett, *Polarized Light - Fundamentals and Applications*, New York, Marcel Dekker, 1993.

[4] G. P. Agrawal, *Fiber Optic Communication Systems*, Third Edition, Wiley, 2002.

[5] G. P. Agrawal, *Nonlinear Fiber Optics*, Third Edition, Academic Press, San Diego, CA, 2001.

[6] *Photonic Devices* course didactic material, prof. M. Santagiustina, a.a. 2010/11, DEI Unipd.

[7] M. Ikeda, *Optical Communications* **39**, 148 (1981).

[8] J. Hegarty, N. A. Olsson, and L. Goldner, *Electron. Lett.* **21**, 290 (1985).

[9] T. Sato, T. Horiguchi, Y. Koyamada, and I. Sankawa, *IEEE Photon. Technol. Lett.* **4**, 923 (1992).

[10] S. V. Chernikov, Y. Zhu, R. Kashyap, and J. R. Taylor, *Electron. Lett.* **31**, 472 (1995).

[11] P. B. Hansen, A. J. Stentz, L. Eskilden, and J. R. Pedrazzani *Electron. Lett.* **27**, 2164 (1996).

[12] M. Nissov, K. Rottwitt, H. D. Kidorf, and M. X. Ma, *Electron. Lett.* **35**, 997 (1999).

[13] J. Toulouse, ”Optical Nonlinearities in Fibers: Review, Recent Examples, and Systems Application”, *J. Lightw. Technol.*, vol. 23, no. 11, pp. 3625-3641, Nov. 2005.

[14] F. Chiarello, L. Ursini, L. Palmieri, and M. Santagiustina, ”Polarization Attraction in Counterpropagating Fiber Raman Amplifiers”, *IEEE Photon. Technol. Lett.*, vol. 23, no. 20, pp. 1457-1459, Oct. 2011.

[15] M. Ferrario, V. Gilardone, P. Martelli, L. Marazzi, M. Martinelli, ”Effective All-Optical Polarization Control Induced by Raman Nonlinear Amplification”, *ECOC 2010*, 19-23 September, 2010, Torino, Italy.

[16] L. Ursini, M. Santagiustina, and L. Palmieri, ”Raman nonlinear polarization pulling in the pump depleted regime in randomly birefringent fibers”, *IEEE Photon. Technol. Lett.*, vol. 23, no. 4, pp. 254-256, Feb. 2011.

[17] MS9710B Optical Spectrum Analyzer Operation Manual, 15th Edition, Anritsu Corporation, December 2008.

[18] ”Scrambling to Reduce Polarization Related Impairments”, General Photonics Application Note, April 2003.

[19] Deterministic Polarization Controller - TXP5004-DPC5500, SOP Scrambler Features available at Thorlabs website, `http://www.thorlabs.de/NewGroupPage9.cfm?ObjectGroup_ID=930`.

[20] C. Flueraru, S. Latoui, J. Besse, and P. Legendre, ”Error Analysis of a Rotating Quarter-Wave Plate Stokes’ Polarimeter”, *IEEE Transactions on Instrumentation and Measurement*, vol. 57, no. 4, pp. 731-735, Apr. 2008.

[21] Integrated PolaRITE™ II/III with Miniature Piezo Driver Card - PCD-M02, SOP Scrambler Features available at General Photonics website, `http://www.generalphotonics.com/Old_Website/PCD-M02.htm`.

[22] *IEEE Transactions on Instrumentation and Measurement*, Vol. IM-32, No. 1, March 1983.